Doped La0.5Sr0.5MnO3 as Oxide Anode for Solid Oxide Fuel Cells using Dry C3H8 for Fuel

アウディ，マジダン，ビン，カマルル，バハライン

https://doi.org/10.15017/1806995

出版情報：九州大学，2016，博士（工学），課程博士
バージョン：

Doped $La_{0.5}Sr_{0.5}MnO_3$ as Oxide Anode for Solid Oxide Fuel Cells using Dry C_3H_8 for Fuel

Audi Majdan Kamarul Bahrain

Kyushu University

Table of Contents

Chapter 1

Introduction

1.1 Fuel Cell Technology

By 2013, the worldwide energy use reached a staggering 13541 million tonnes of oil equivalent (Mtoe) and is projected to grow by one-third by 2040 according to International Energy Agency.[1, 2] This huge energy demand leads to excessive consumption of fossil fuels which actively contribute to formation of the greenhouse gas (GHG) emission and unavoidable increase of energy price. Reduction of GHG emissions from the energy supply requires the power sector to be deeply decarbonised.[2] Whilst many look to renewable energy like solar, tidal and wind power technology, most produce limited energy supply due to power fluctuation. In this regard, one practical and promising method for the near future is energy conservation; namely, to increase the current energy conversion efficiency rather than outright use of intermittent alternative energy source. From this point of view, the fuel cells (FCs) technology is highly anticipated.[3]

A fuel cell is an energy conversion device that converts the chemical energy of a fuel directly to electrical energy and heat, without the need for combustion as an intermediate step. A combination of a gaseous fuel (like hydrogen or hydrocarbon fuels) and an oxidant gas (like oxygen or air) go through electrodes and half-cell reaction occurs on anode and cathode respectively, with the active charge carrier species going through an ion conducting electrolyte. In this way, electrons are released into external circuit to produce electricity. Hence, quite similar to batteries, the operating principles of fuel cells are electrochemical combination of reactants to generate electricity. However, unlike a battery, a fuel cell does not require recharging because theoretically, the cell operates as long as both fuel and oxidant are supplied to the electrodes which proves to be a huge advantage. Needless to say, it represents environmental-friendly technology with negligible influence exerted on the natural environment. Additionally, fuel cells offer higher thermodynamic energy efficiencies than conventional combustion engines (30%) because chemical energy is converted directly into electrical

energy without the limitation of Carnot cycle.[3] In fact, current fuel cells when operated alone have efficiencies of about 40%-55%, and with combined heat and power (CHP) system the efficiencies reaches 80%.[4]

There are several types of fuel cells that have been developed. Generally, fuel cells are classified by the electrolyte used as the ionic conductor in the cell as shown in Table 1.1.

Table 1.1 Fuel Cell Types and Operating Features[5]

	PEMFC	**PAFC**	**AFC**	**MCFC**	**DMFC**	**MFC**	**SOFC**
Electrolyte	$CF(CF_2)_n$ $CF_2\ SO_3^-$	H_3PO_4	KOH	Li_2CO_3-K_2CO_3, Li_2CO_3-Na_2CO_3	$CF(CF_2)_n$ $CF_2\ SO_3^-$	Nafion, salt bridge, soil, ceramic	$Zr(Y)O_2$, $La(Sr)Ga(Mg)O_3$, $Ce(Gd)O_2$
Charge carrier	H^+	H^+	OH^-	CO_3^{2-}	H^+	H^+	O^{2-}
Temperature (K)	353	473	333-493	923	333-393	293-328	873-1273
Catalyst	Platinum	Platinum	Platinum	Nickel	Platinum, Ruthenium	Bacteria	Ceramic
Cell Components	Carbon based	Carbon based	Carbon based	Stainless based	Carbon based	Carbon based	Ceramic based
Fuel	H_2, methanol	H_2	H_2	H_2, CH_4	Methanol	Organic, Inorganic matter	H_2, CH_4, CO

All types of fuel cells are based on the same principle of electrochemical reaction but differ in their operating temperature, fuel, material and performance. Each have their own merits and demerits, however the SOFCs have been considered as the most promising system to generate electrical energy generator for commercial usage due to its high fuel-to-energy conversion ratio in the absence of expensive catalysts[6] which is the main motivation for this study.

SOFC is an all ceramic electrochemical power generation device that relies on the transport of oxide ions or protons across a ceramic membrane operating at temperatures in the range of 773 – 1273 K. A typical SOFC is composed of an electrolyte sandwiched between two porous electrodes, the anode and cathode. Unlike low-temperature PEM fuel cells, SOFCs have the ability to operate on a variety of fuel sources, including hydrocarbon or carbonaceous fuels due to their high operating temperatures ($\geq$ 973 K), which is a huge advantage compared to other type of fuel cell. While gases such as carbon monoxide, methane, and other hydrocarbons that are poisonous to low-temperature PEM fuel cell anodes, it can be a part of the fuel stream in an SOFC. The ability of SOFCs to facilitate internal fuel reforming for carbonaceous fuels allows for the possible removal of the reformer used to convert the hydrocarbon fuel into syngas.

Nevertheless, SOFCs still face many challenges in the development of materials and reduction of costs to make them eligible for wide-scale commercialization. For example, the sealing of fuel side feeds at high operating temperatures (> 973 K) requires expensive and relatively inert materials with good matching of thermal expansion coefficients with fuel cell materials. The electrode and electrolyte materials with rapid-heating capabilities and minimal cracking would improve SOFC applicability for applications with numerous stop-start cycles. Another major issue is long term stability in performance of SOFC systems when operating on hydrocarbon fuels or with fuels having impurities.[7-10]

Hydrocarbon fuels may produce carbon deposition in the anode pores which deactivates the electrocatalyst when it blocks the anode pores, resulting in loss of performance. The current study aims to explore fundamental issues in identifying preferred material combinations for durable SOFC anode operation in hydrocarbon fuel and hence in the following section theoretical and basic understanding on SOFC anode are presented.

1.2 Operation of SOFC with Hydrocarbon Fuel

As described in previous sections, SOFCs have the potential to be fuel flexible due to their high operating temperatures. Three common ways hydrocarbon fuels can be utilised with SOFC includes external reforming, internal reforming and direct oxidation. Each has specific advantages however suitability very much depends on the feasibility of the intended application. Normally, hydrocarbon reforming is necessary because electrochemical oxidation of heavy hydrocarbon fuels are particularly difficult not to mention the electrode can be poisoned from sulfur content in the fuel. Especially important, coking or carbon formation build-up on the electrode may block the reaction site at TPB. This occurs when solid carbon deposited on the anode surface, clogging the pores which deactivate the reforming and electrochemically active surface oxidation sites.

Popular workaround for this issue is via external reforming, where a syngas feed is created as a product outside of the fuel cell. Syngas is a mixture of CO and H_2 produced from heavy hydrocarbon gas. Instead of directly exposing SOFC anodes to hydrocarbons and letting the cell reforms the fuel internally, hydrocarbons can be reformed externally and the syngas is fed to the cell. This way, the syngas products are easier to electrochemically oxidized in the cell than the parent hydrocarbons. Performance is better and coking is less of an issue, since the pyrolysis route can be avoided. However,

huge penalty is imposed on the overall system complexity due to addition of extra components like reformer which incur higher costs and affects portability.

With internal reforming, the reforming reactions are carried out within the SOFC anode itself, made possible due to high operating temperature. The products stem from the anode electrochemical reaction can be used for hydrocarbons reforming. In large scale systems, this is very beneficial since the endothermic effect of steam reforming helps mitigate some of the issues of offsetting the heat of the electrochemical reaction thereby reducing sealing issues to some extent. For syngas and direct hydrocarbon fuel feeds, the following water gas shift reaction is important in order to understand the effect on cell performance in which CO is transformed into H_2 upon reaction with steam.[11]

$$CO_{(g)} + H_2O_{(g)} \leftrightarrow CO_{2(g)} + H_{2(g)} \left[\Delta H = -\frac{41\ kJ}{mol}\right] \quad (1\text{-}1)$$

At higher temperature, the thermodynamics of the water gas shift reaction shifts to the left, thereby producing more carbon monoxide. It is required to cool the product gas from the steam reformer and pass it through a reactor containing catalyst, which promotes the shift reaction. For instance, a steam reformer running on natural gas and operating at atmospheric pressure with an outlet temperature of 1073 K produces a gas comprises of ca. 60% hydrogen, 22% steam, 13% carbon monoxide, 5% carbon dioxide and traces of methane.[9] To minimize the risk of carbon formation, steam is added to the fuel stream, and if the steam concentration is high enough, thermodynamic equilibrium will lean more heavily towards the formation of CO_2 and H_2 via Reaction 1-1 than towards the formation of solid carbon. In general, a steam/carbon ratio (*S/C*) of 2.0 to 3.0 is normally employed in steam reforming so that carbon deposition may be avoided.[12] However, because steam is made through the electrochemical oxidation of H_2 in the SOFC anode, lower inlet *S/C* can be used in SOFC

anodes. Steam also aids the reduction in coking by carbon gasification reaction, given here in Reaction 1-2.

$$C_{(s)} + H_2O_{(g)} \leftrightarrow CO_{(g)} + H_{2(g)} \quad (1\text{-}2)$$

Yet, there are many disadvantages of internal reforming compared to using an ideal anode which tolerate dry hydrocarbons:[13]

a) Steam reforming requires considerable amounts of water in the fuel (usually a steam to carbon ratio (S:C) of about two), which results in a diluted fuel.[14, 15] This has a negative effect on the electromotive force (EMF) of the cell and thereby the electrochemical efficiency is reduced.[16]
b) Steam reforming is an extremely endothermic process. In the case of external reforming, this requires a considerable transport of entropy, which involves an energy loss. Internal steam reforming directly on the anode may cause large thermal gradients that can damage the cell.
c) Extra costs are involved in heat exchangers and additional equipment for steam raising or recycling of the anode exhaust gas.
d) While conventional SOFC anodes made up of Ni/YSZ are preferred due to low cost and high catalytic activity of nickel,[12, 17] they are not suitable for hydrocarbon reforming because Ni/YSZ anodes are prone to failure from sulfur poisoning [18-20] and carbon deposition[21] as shown in Figure 1.1.

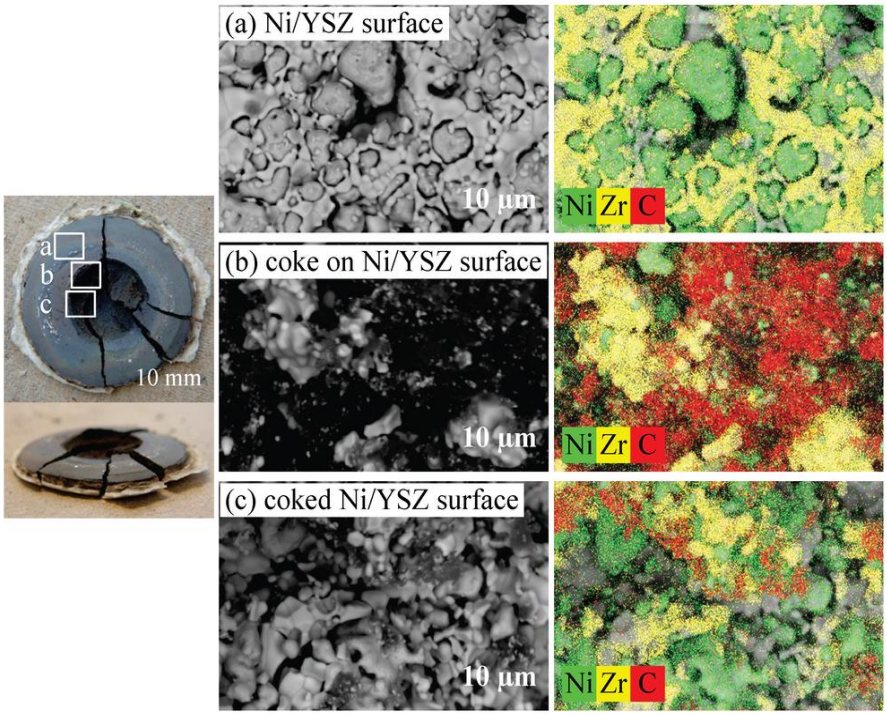

Figure 1.1 Coking on the surface of Ni-YSZ upon exposure to hydrocarbon fuel [(22)]

Alternatively, direct oxidation hydrocarbon feed to the SOFC lack most of the disadvantages of external or internal reforming. Principally, elimination of reformer is hugely beneficial to the industrial balance of plant (BOP), reducing the overall cost as well as the complexity of the system. Portability will also no longer an issue, paving the way for scaled down SOFC for transportation. Additionally, energy efficiency is improved due to the lack of fuel conversion required in the first place. In fact, the reforming reaction take place internally and can provide internal cooling to the fuel cell.[(16)] Yet, the main problem with direct hydrocarbon oxidation is coke formation for without steam, carbon formation is thermodynamically much easier to proceed. This is made worse when the anode is based on Ni as has been mentioned previously.

1.3 Carbon Formation and Mitigation in SOFC

In addition to reforming and water gas shift, the carbon formation from the Boudouard reaction in Reaction 1-3 can occurs particularly on Ni surfaces that encourage surface carbon build-up:

$$2CO_{(g)} \leftrightarrow C_{(s)} + CO_{2(g)} \quad (1\text{-}3)$$

This reaction explains the formation of solid carbon, which is highly undesirable for an SOFC not just from performance point of view, but also from long term durability point of view.[16, 23] To understand when carbon will form, it is important to understand the reactions that deposit and remove carbon. At least two mechanisms are known to exist at high temperatures for carbon deposition.[24, 25] First, carbon can form as a result of reactions over a catalyst. This process has been very well studied over Ni, Fe, and Co, both for catalytic applications[26-33] and for "dusting", also known as "dry corrosion", the problem of pitting when steels are exposed to hydrocarbons at high temperatures.[34, 35] The mechanism on each of these metals involves deposition of a carbon source onto the metal surface, dissolution of the carbon into the bulk of the metal, and finally precipitation of carbon. Many types of coke can be formed, depending on the material (surface) used for the (catalytic) cracking of the hydrocarbon. At least three major families of coke exist: filamentous, amorphous, and graphitic.

Graphitic coke is formed mainly at high temperatures (> 1173 K) and has a higher density than that of other types of coke. It is important to recognize that the metal is not merely covered by carbon in this reaction, but becomes part of the carbon fibre, explaining the pitting that is observed in dry corrosion. Filamentous coke can be divided into different subtypes depending on the structure of

the coke; for example, filaments with a rope-like appearance have been found. Normally, filamentous coke contains metal particles. In contrast to this, amorphous coke contains few or no metal particles.

The results of the different carbon formation pathways may be illustrated by the difference in carbon growth on Ni and Pt-Fe catalysts. This is especially true for nickel which is a good catalyst for cracking of both methane and higher hydrocarbons. The Ni catalyses the formation of carbon nanotubes that grows with the nickel particle at its tip. A nickel catalyst is therefore normally not stable in methane. Another mechanism for growing coke is observed for an alloy of the Pt-Fe where the tube of coke is extruded from the catalyst particle, which stays in contact with the support during the growth of the coke.

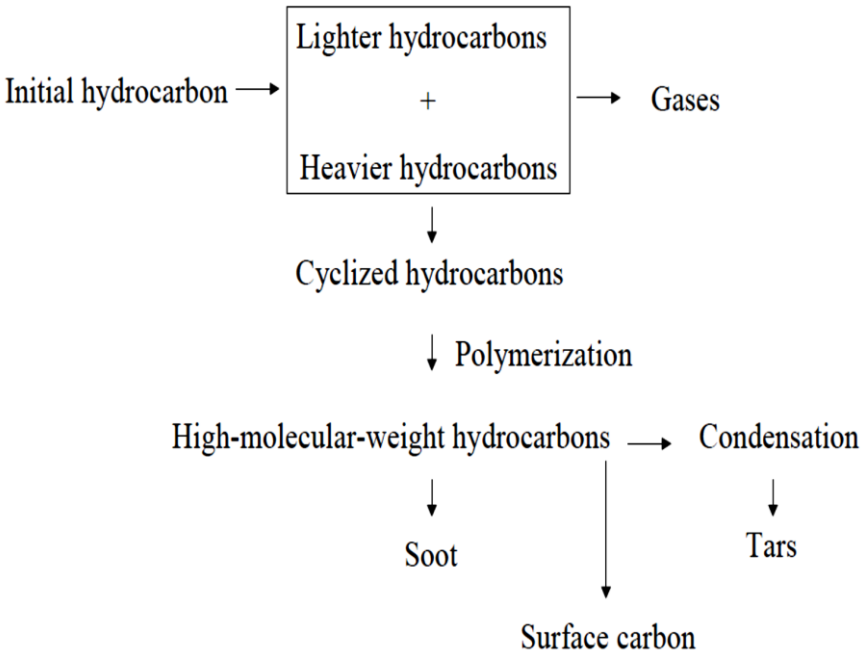

Figure 1.2 Diagram of the formation of carbon by pyrolysis of hydrocarbons through free-radical reactions[36]

Additionally, carbonaceous compounds can also form in the absence of a catalyst via free-radical, gas-phase condensation reactions or pyrolysis.[37] Especially, higher hydrocarbons like n-butane can undergo pyrolysis readily in SOFC conditions (Figure 1.2).[36] Even natural gas, for example, will decompose when heated in the absence of air or steam at temperatures above 932 K. These reactions are most important for hydrocarbons larger than methane and are usually initiated by $C - C$ bond scission at high temperatures. While the primary products of pyrolysis are molecules that are smaller than the parent hydrocarbons, the olefins that are formed by pyrolysis can react with radicals to form larger molecules. The carbonaceous products that are ultimately formed by pyrolysis are high-molecular weight, polyaromatic compounds, [38, 39] perhaps best referred to as tars and quite different in form from the graphitic fibers on Ni, Co, and Fe catalysts. Because C-H bonds are much stronger than C-C bonds, considerably higher temperatures are required to pyrolyze CH_4 compared to larger alkanes. It is also noteworthy that calculations suggest H_2O does not appear to enter gas-phase reactions,[40] so that the addition of steam provides no obvious gas-phase reaction for preventing carbon formation and establishing equilibrium between carbon deposits and the hydrocarbon.

Obviously, coking mitigation and prevention is essential if hydrocarbon fuel to be utilized. External reformer has already been described to prevent the coking problem but not suitable for BOP because it greatly add up to the cost, system complexity and penalty to portability. Carbon formation can also be mitigated by altering testing conditions. Lin et al.,[41] for example, found that maintaining a high current density allowed for stable operation under methane. Under current loading, the flux of oxide ions from cathode may facilitate the carbon gasification reaction. However, it is still not proven to assist in operation using heavier hydrocarbon fuel. Low operating temperatures (< 973 K) has also been cited to avoid carbon deposition as reported by Murray et. al.,[42] however, these conditions put severe constraints on the operation of an actual fuel cell application.

Even internal reforming still comes with many limitation especially if Ni-based cermet is still used as the anode. For example, it has been proposed to operate the cell in the thermodynamic regime where carbon is predicted to be unstable.[43-46] Unfortunately, thermodynamic analysis assumes that the rates of the forward reaction (carbon deposition) and the reverse reaction (carbon removal) are rapid enough to establish equilibrium, an assumption that cannot be justified.[47] There are many examples where carbon does form under conditions where it is predicted to be thermodynamically unstable. For example, based on the calculations of Sasaki and Teraoka, carbon is thermodynamically unstable towards reaction to CO and CO_2 for essentially all hydrocarbon fuels at 773 K when there is a H_2O:C ratio of 1.8 or greater.[46] In truth, it has been shown that carbon formation will occur at this temperature on Ni catalysts at H_2O:C ratios greater than 3.0 following the addition of even a few percent of olefins to methane.[48] Other studies have also shown that conditions under which carbon deposits form on Ni and Co catalysts depend strongly on the metal particle size, a result that cannot be explained by thermodynamics.[49] Clearly, the penalty associated with internal reforming outweighs its benefit. This issue necessitates an alternative material with coke-suppression ability, robust and durable enough to withstand the harsh environment of hydrocarbon fuel but with comparable electrocatalytic activity to Ni.

1.4 Anode

The role of an anode in SOFC is electro-oxidation of fuel by catalyzing the reaction, facilitating fuel access and removal of product. Therefore, the anode materials should meet several requirements:[50-53]

1) Stability in reducing environment;

2) Sufficient electronic and ionic conductivity; Mixed ionic and electronic conductor (MIEC)

3) Porous structure;

4) Thermal expansion coefficient (TEC) matching with electrolyte materials;

5) High catalytic activity.

These requirements together with elevated operating temperature limit the choice of the anode materials to nickel and the noble metals. The vast majority of SOFCs have a nickel anode because of its low cost compared to precious metals. The most commonly used anode materials are cermet composed of nickel and solid electrolyte, such as Ni-YSZ, Ni-SDC, aiming at maintaining porosity of anode by preventing sintering of the Ni particles and giving the anode a TEC comparable to that of the solid electrolyte. The threshold for electrical conductivity is about 30 vol% nickel.[9] The conductivity of the anode depends on its microstructure, in particular the size and particle size distribution of the solid electrolyte and nickel particles, and the connectivity of the nickel particles in the cermet.

However, while Ni is an excellent catalyst for the dissociation of hydrogen and an excellent electronic conductor, there is a mismatch of TEC with the YSZ electrolyte and is known to have considerable reaction with LSGM producing a separate phase of $LaNiO_3$. In addition, during longer operation, the Ni metal aggregates by grain growth leading to reduced porosity and the blocking of TPB. Another problem that occurs with carbonaceous fuels is heavy coking as has been discussed in previous section, and sulfur poisoning of the Ni/YSZ anode.[54] Natural gas and petroleum liquids contain organic sulfur compounds that normally have to be removed before any further fuel processing can be carried out. Sulfur level even as low as 2 ppm is detrimental to SOFC performance even at high operating temperatures.[55]

Therefore, there is a growing interest in developing novel anodes as alternatives to Ni cermets. The development of anodes that will be operated with hydrocarbon fuels is hence driven by a number of factors namely (a) high electronic conductivity (b) poor reformer catalyst (c) high melting temperature (d) low surface energy and (b) single component electrode rather than composite. Since anode is the focus of this thesis, alternative anode for SOFC using hydrocarbon fuel will be discussed in the next section.

1.5 Relevant Anode for Hydrocarbon Fueled SOFCs

Fluorite ceria is extensively studied for direct hydrocarbon conversion especially when doped with Gd_2O_3 or Sm_2O_3, The efficacy of CeO_2 based ceramics lies in the fact that they exhibit MIEC characteristic in a reducing atmosphere owing to reduction of Ce^{4+} to Ce^{3+}. Ceria's electronic conductivity, however, is insufficient as the sole current conductor (~0.2 S/cm) while for Gd-doped ceria (GDC) it is only 0.08 S/cm at 1073 K. Additionally, it was first thought that CeO_2 possess good catalytic activity stemming from the oxygen-vacancy formation and migration associated with reversible CeO_2–Ce_2O_3 transition. However, later detailed investigations proved that reduced ceria is almost inactive to C–H bond breaking.

Unlike Ni, even though copper is a metal, it is known to have a low susceptibility for carbon formation on the metal surface. Hence, copper cermet anodes have been actively investigated in SOFC for instance, Cu/SDC (samaria doped ceria) and Au/SDC were tested using H_2 and n-butane fuels at 923 K. Their results show similar *I-V* performance proving that Au and Cu are simply electronic conductors without any catalytic characteristics. Being a poor catalyst for C–H and C–C bond breaking and low melting point of 1356 K compared to Ni (1726 K) limits the operating temperatures that can be used with Cu anodes.[56-58] On the other hand, the volume change of the Cu-CeO_2 anode during

redox cycling will cause degradation of the stack. Therefore, this cermet is not quite suitable and redox stable anodes are still in high demand.

To supplement each other weaknesses, later development combined both Cu and CeO_2 as composite anodes material that provides a lower resistance path for electrons and better catalytic features. Gorte and co-workers focuses primarily on porous YSZ anode structures impregnated with Cu-CeO_2 mixtures or Cu/CeO_2/YSZ, for use in the oxidation various carbonaceous fuels.[54, 58] Cu-YSZ is reported to be inert to methane, while ceria addition improves the power densities and stable operation over a period of at least 3 days without deactivation due to carbon deposition. Interestingly, they reported increased power density when exposed to butane after reduction in H_2 (Figure 1.3 (a)) and proposed that the improvement is due to carbonaceous structure which extends the TPB. They have also demonstrated the robustness of the composite by using n-decane as direct fuel with quite similar performance (Figure 1.3 (b)). Nevertheless, the remarkable power density using this composite is mostly contributed by the thin electrolyte that they used (60 μm) and the impregnation technique. And since Cu is used, their operating temperature is similarly limited.

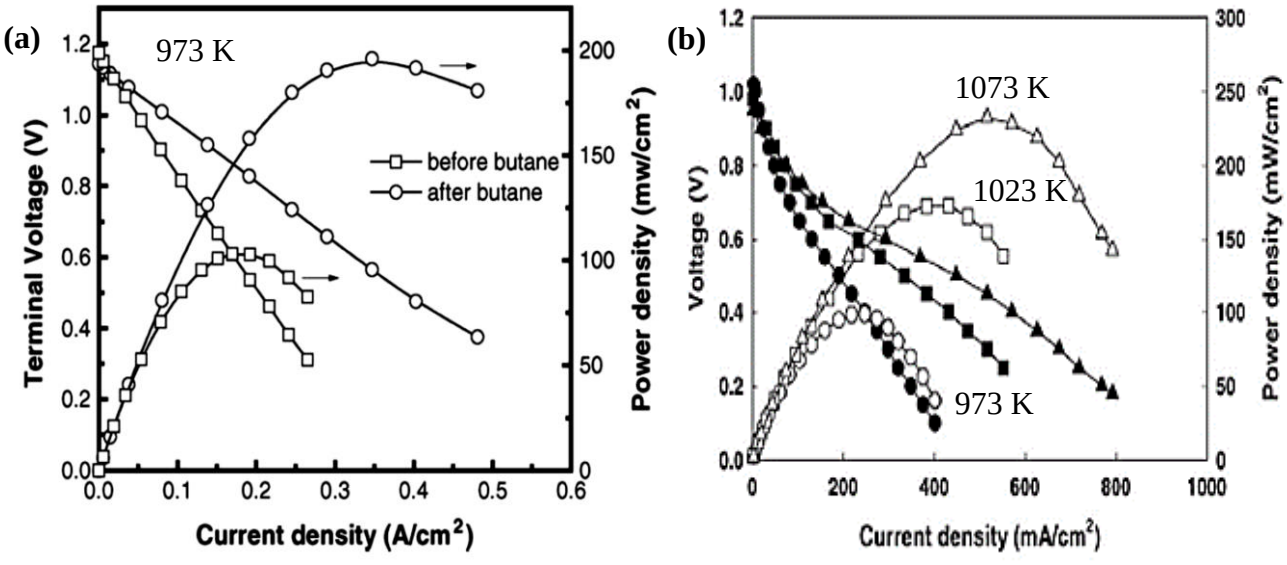

Figure 1.3 *I-V* curve for Cu/CeO_2/YSZ using (a) butane and (b) n-decane[54]

1.5.1 Perovskite oxide

Perovskites are rapidly emerging as an alternative material for SOFC materials due to its unique structure.[59-63] It is named from the mineral perovskite $CaTiO_3$ and is a naturally occurring mineral that is abundant in chlorite, talc, and serpentine rocks. The general formula is ABO_3, where A and B are cations with a total charge of +6, with the unit cell shown in Figure 1.4. The lower valence A cations are typically larger and reside on the 6-fold coordinated corners of a simple cubic lattice, with the B cations occupying the 12-fold coordinated center site. The oxygen atoms are found in a face-centered structure around the central B cation. Therefore, an ideal perovskite exhibits a cubic space group *Pm3m.*

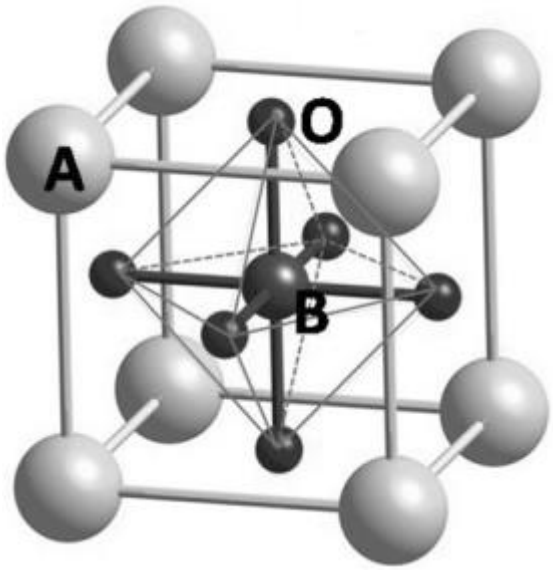

Figure 1.4 The structure of perovskite with the origin centered at the B-site ion

The properties that makes perovskite attracting interest as material of choice for SOFC lies in its structure. Generally, perovskite exhibits excellent thermal and mechanical stability even above the

operating temperature of SOFC at 1273 K, which is a huge advantage over Ni that may aggregated. Some perovskites can accommodate a large content of oxygen vacancies, making themselves potential oxygen ion conductors. This is due to perovskites having large tolerances for departure from its ideal stoichiometry.[64] Generally speaking, perovskite allows first-row transition metal cations to be introduced into B-site and rare-earth and/or lanthanoid cations into A-site. First-row transition metal cations usually exhibit multi-valence in function of pO_2 allowing the creation of MIEC capable perovskite. For example, manganite, ferrite, and cobaltite perovskites have modest ionic conductivity but high electronic conductivity. In addition, the presence of oxygen vacancies is another factor that makes perovskite suitable as anode for hydrocarbon fuel since it may provide a potential carbon cleaning mechanism.[65] Perovskite oxides containing transition metals at B sites have been proven to be effective catalysts for the combustion of light hydrocarbons like CH_4 and C_2H_6.[66] Hydrocarbon oxidation over perovskite oxides is thought to proceed by both suprafacial and intrafacial reactions.[67] The suprafacial reactions take place between the adsorbed species on the surface at relatively low temperatures, and the reaction rates appear to be correlated primarily with the electronic configurations of the surface transition-metal ions. The intrafacial reactions typically occur at high temperatures, with rates that are greatly dependent on the thermodynamic stability of oxygen vacancies adjacent to the transition-metal ion.

In this regard, many perovskite has been investigated as a potential anode for example improved performance has been reported on perovskites based upon Cr and Mn at the B-site of $(La,Sr)Cr_{1-x}Mn_xO_{3-\delta}$. Tao and Irvine studied the lanthanum chromite doped with Sr and Mn up to 20% dopant on the B-site, usually 5 or 10%. The $(La_{0.75}Sr_{0.25})Cr_{0.5}Mn_{0.5}O_3$ (LSCM) exhibits comparable electrochemical performance to Ni/Y_2O_3 stabilized ZrO_2 (YSZ) cermets.[68] Good performance is

achieved for methane oxidation without using excess steam (Figure 1.5). This anode is stable in both fuel and air conditions and shows stable electrode performance in methane.

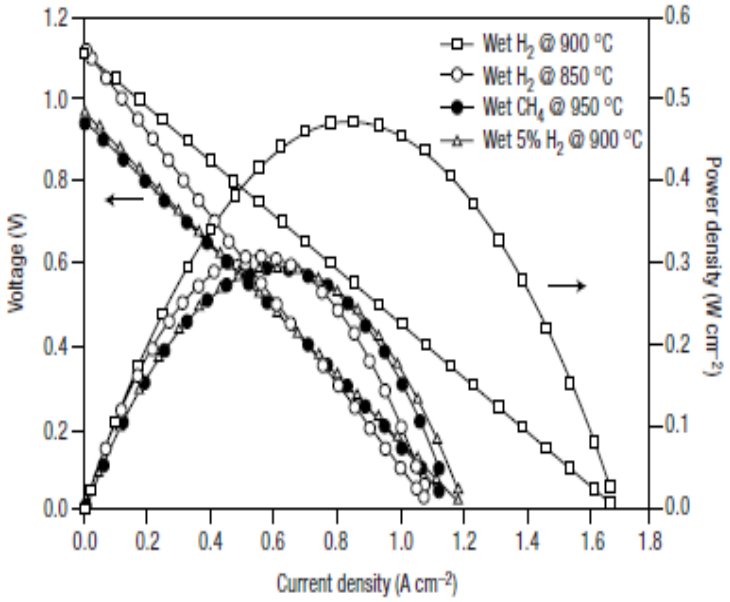

Figure 1.5 *I-V* curve for $La_{0.75}Sr_{0.25}Cr_{0.5}Mn_{0.5}O_3$ using methane fuel[68]

Titanate is another group of anode materials for hydrocarbon fed SOFC. The Ti^{4+}/Ti^{3+} redox couple could accept electrons from the H_2 dissociation. In this case $SrTiO_3$ is the most popular parent structure, which is of negligible conductivity across a wide range of pO_2 but greatly improved by doping. For example La^{3+} is an appropriate donor dopant because of similar ionic radius with Sr^{2+}. The electrical conductivity of $La_xSr_{1-x}TiO_3$ (LST) depends on the thermal history and pO_2 during sample preparation. A YSZ-supported single cell with $La_{0.4}Sr_{0.6}TiO_3$ (LST46) showed modest cell performance, with maximum power density of 25 $mWcm^{-2}$ at 1273 K in wet H_2.[69] A power density of 0.17 $mWcm^{-2}$ was obtained at 1273 K for LST46–YSZ composite anode fed with 5000 ppm H_2S–H_2.

Another variation of perovskite that is used for anode includes double perovskite like $Sr_2MgMoO_{6-\delta}$ (SMMO).[70] The Mo^{6+}/Mo^{5+} redox couple provided the electronic conductivity. Power densities is recorded to be 0.84 W/cm^2 in H_2 and 0.44 W/cm^2 in CH_4 at 1073 K, and good sulfur tolerance up to 50 ppm H_2S is exhibited. However, under prolonged reduction above 1173 K, SMMO began to decompose into MgO, metallic Mo, and some Ruddlesden–Popper phases.

Meanwhile, Shin et al. prepared a composite of $La_{0.6}Sr_{0.4}Fe_{0.9}Mn_{0.1}O_3$ (LSFM) and $Ce_{0.6}Mn_{0.3}Fe_{0.1}O_2$ (CMF),[62] combining high electrical conductivity of LSFM with the catalytic properties of CMF, similar concept to Gorte and his co-workers with Cu-Ce composite. The composite shows high anodic activity with high power density of up to 1 W/cm^2 in C_3H_8 at 1073 K when utilizing $LaGaO_3$-based electrolyte[55, 71-74] which provides exceptional ionic conductivity at low temperature (Figure 1.6). Even when using heavy hydrocarbon, no coke formation was detected when dry C_3H_8 or C_4H_{10} was directly used for fuel.

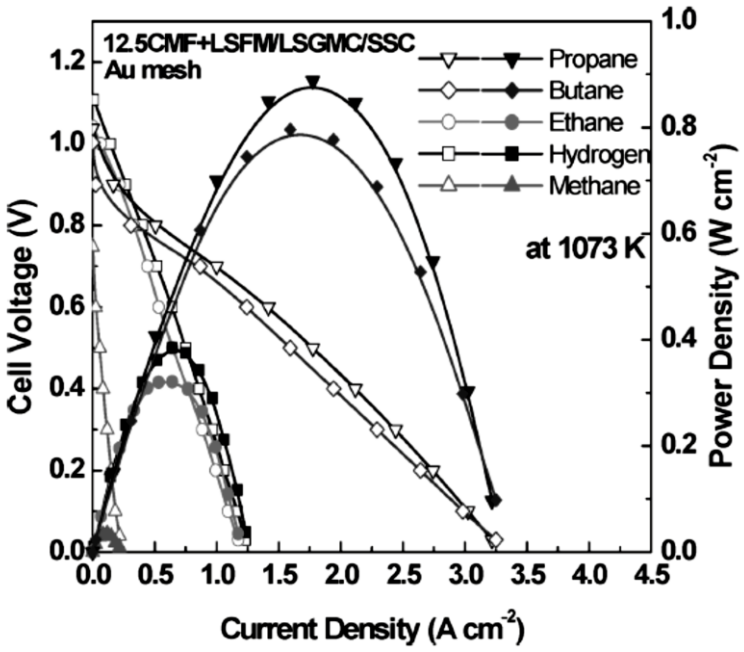

Figure 1.6 *I-V* curve for CMF-LSFM using various hydrocarbon fuels[62]

1.6 Doped $LaMnO_3$ as an Anode of SOFCs

Lanthanum manganites ($LaMnO_3$) is a material that belong to ABO_3 perovskite oxide family with the larger La ions occupy the 12 coordinated A-sites and the transition metal ions Mn occupy the octahedral B-sites. It is widely used as material component for high temperature SOFCs due to their great compatibility with ZrO_2/Y_2O_3 electrolytes. Its crystalline structure is deeply influenced by temperature and oxygen partial pressure but it is rhombohedral at room temperature while the undoped lanthanum manganites is orthorhombic but there is a crystallographic transition of orthorhombic/rhombohedral at 873 K. This transformation has been attributed to the oxidation of some Mn^{3+} to Mn^{4+} ions, which reduces the energy tending to produce long range Jahn–Teller ordering.[75] Thus, the orthorhombic/ rhombohedral transition temperature is dependent on the Mn^{4+} content and sensitive to the stoichiometry of the material. Hence, doping lower-valence cations such as Sr^{2+} and Ca^{2+} for the La sites increases the Mn^{4+} concentration in $LaMnO_3$, thus affecting the transformation temperature. This material can be formulated as $La_{1-x}A_xMnO_{3\pm\delta}$ (where A is divalent cation, "+" denotes an oxygen excess and "-"an oxygen deficiency). In the Sr-doped lanthanum manganite ($La_{1-x}A_xMnO_{3\pm\delta}$ with $x < 0.5$) a manganese ion oxidation is observed:[76]

$$2SrO + \frac{1}{2}O_{2(g)} \xrightarrow{LaMnO_3} 2Sr_{La} + Mn\cdot_{Mn} + 3O_O^x \qquad (1\text{-}4)$$

Depending on the doping level, $La_{1-x}A_xMnO_{3\pm\delta}$ can display three lattice types: rhombohedral ($0 \leq x \leq 0.5$), tetragonal ($x = 0.5$), and cubic ($x = 0.7$) (Figure 1.7).[75, 77] According to reaction 1-4, when La^{3+} is substituted with Sr^{2+} in $LaMnO_3$ lattice (LSM) , electro-neutrality is sustained by the formation of Mn^{4+} due to the charge compensation, increases the electron-hole concentration and contributes to increased electrical conductivity. Due to the formation of cation vacancies, LSM is an intrinsic p-type

electrical conductor. The electrical conductivity of LSM takes place via small polaron hopping throughout the ceramic matrix. A polaron is defined as an electron that travels through a solid state material that, as it passes by positive ions, attracts them and, as it passes by negative ions, repels them. This electronic transport deforms the overall structure slightly as electrons pass through the structure. It has sufficient electrical conductivity at high temperatures of about 102 $S \cdot cm^{-1}$ at 1273 K and the electrical conductivity increases with increasing temperature and increasing strontium concentration. The conductivity increases when the strontium concentration is increased from 10% to 50% and at equimolar concentration of La and Sr, ($La_{0.5}Sr_{0.5}MnO_3$ or LSM55) it shows the maximum electrical conductivity in air (200 – 485 S/cm at $x = 0.5$ at 1273 K).[78] Under normal operating conditions, LSM exhibits a negligible amount of ionic conductivity. While the ionic conductivity of LSM is lower than that of the YSZ electrolyte, it increases with the Mn substitution by Co.[79]

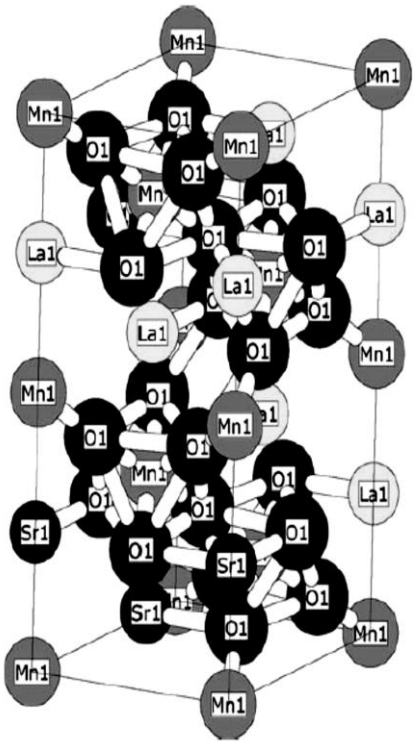

Figure 1.7 The schematic crystal structure of $La_{0.7}Sr_{0.3}MnO_3$).[75]

The LSM system is the typical choice for the cathode of SOFC because of its stability under oxidising conditions (decomposition at 1273 K for $pO_2 < 10-14$), with its thermal expansion that matches to the YSZ electrolyte (TEC ~11.1 × 10^{-6} cm/cm K^{-1}). However, using LSM as an anode is not studied thoroughly due to its chemical instability under reducing atmosphere. In addition, the stability of the perovskite oxide, in general, increases with the size of A-site cations. [80] Hence, while both electrical conductivity and catalytic activity of LSM are enhanced considerably when lanthanum is substituted partially with strontium, concurrently the stability is reduced. In particular, oxide AMO_3-type oxides (A = Ln (lanthanides), Ca, Sr, Ba; M = Cr, Mn, Fe, Co, Ni, Ga, In) becomes unstable at higher temperatures and lower oxygen partial pressures with a phase conversion to A_2MO_4.[81] When exposed to reducing atmosphere of about 10^{-14} to 10^{-15} atm at temperatures above 1373 K, for example $La_{1-x}Sr_xMnO_3$ with $x \geq 0.2$ suffers partial decomposition to $La_{2-x}Mn_xO_4$ and MnO. [82] This is significant since decomposition of LSM perovskite phase leads to abrupt decrease in electrical conductivity.[83]

Nevertheless, Ishihara et al. has demonstrated that LSM is active not only as a cathode but also anode.[84] They investigated the effect of Sr content of LSM to the power density when using H_2 fuel. It is reported that $La_{0.5}Sr_{0.5}MnO_3$ (LSM55) exhibits maximum power density of 0.64 W/cm^2 at 1273 K when $La_{0.8}Sr_{0.2}Ga_{0.8}Mg_{0.15}Co_{0.05}O_3$ (LSGMC, 0.3 mm thickness) is used for electrolyte (Figure 1.8 (a)).[84] In particular, both anodic overpotential and especially anodic IR loss drastically reduced when Sr dopant reached 50 mol% (Figure 1.8 (b)). At 50 mol% Sr, LSM achieved the highest electrical conductivity as has been discussed previously and this result agree well that the reduced IR loss is due to the increase in electrical conductivity. While, LSM is naturally a p-type conductor, $Mn^{3+/4+}$ redox couple helps in providing the electrical conductivity.[85]

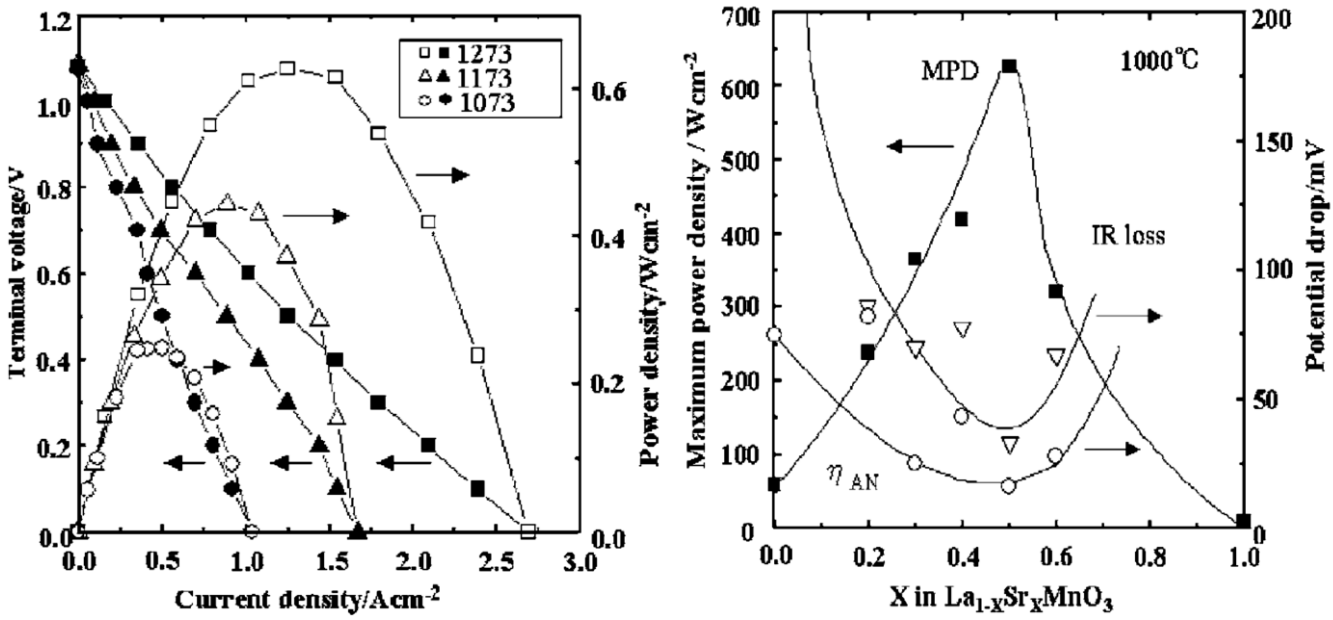

Figure 1.8 (a) *I-V/P* of $La_{0.5}Sr_{0.5}MnO_3$ anode by using H_2 as fuel

(b) Sr dopant content effect of LSM to the power density of cell operated in H_2 [(83)]

Although LSM55 decomposes into La_2MnO_4, $SrMnO_3$ and SrO, the parent $LaMnO_3$ perovskite still exists after the reduction with strong diffraction peaks in Figure 1.9 which explain the stable power density recorded at lower temperature. The study also confirms that the parent $LaMnO_3$ is the active phase in LSM55 while other phases produces negligible power density, suggesting low catalytic activity and electrical conductivity. Additionally, the LSM55 also exhibits very good tolerance towards reoxidation, an important requirement as anode.

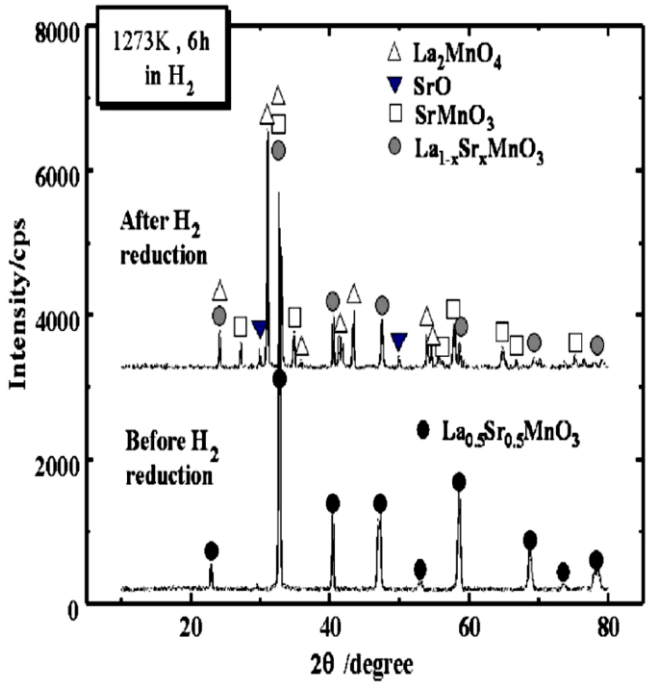

Figure 1.9 XRD decomposition of $La_{0.5}Sr_{0.5}MnO_3$ under H_2 reduction [84]

1.7 Objective of This Study

Based on the current status of anode development, it is obvious that alternative anode to Ni for direct hydrocarbon SOFC is required. The advantages of oxide anodes are obviously their tolerance to reoxidation and small carbon deposition in hydrocarbon fuels. Despite many positive development of oxide anode, the problem with most alternative anode materials is their lower performance compared to Ni based cermet. In addition, most studies focus on new materials with uncharted properties and characteristics. A relatively easier and low-risk route is by improving the current and widely studied material to be used as anode. Hence, the objective of this study is to understand the possibility of using LSM55 as a potential oxide anode with high activity and electrical conductivity and utilizing hydrocarbon fuel. The challenge at the moment is to improve the phase stability of LSM55 under reducing environment as well as the possibility to use it with heavy hydrocarbon fuel. This study consists of the following chapters.

In Chapter 2, the effect of various dopants onto Mn site of LSM55 to its phase stability is investigated. It was demonstrated that the cell using doped Al greatly improved the phase stability of LSM55 under reducing environment owing to stable Al^{3+} state. In addition, it will be discussed why the power density is increased simultaneously. Furthermore, in order to enhance the power density, the effect of Al dopant content was carried out. It was found that 40 mol% Al produces the highest cell performance compared to other dopant content.

In Chapter 3, further improvement to the Al-doped LSM55 was investigated. Among the various dopant, Co as a catalyst is used to enhance the surface activity of the material. The effect of Co dopant content is studied and high maximum power density of approximately 1 W/m^2 at 1273 K in hydrogen and 0.25 W/m^2 at 1173 K in propane fuel was achieved when 20 mol% Co is doped to Al-doped LSM55. In addition, it was confirmed that no coke deposition is observed by using Raman spectroscopy.

In Chapter 4, mixing Al- and Co-doped LSM55 with various oxides for anodic performance was studied and it was found that positive effects were observed when using direct C_3H_8 fuel. In case of oxides mixed with LSMAC72, it was found that STN and CMF shows the most positive effects for C_3H_8 fuel especially at 1173 K. However, at lower temperature at 1073 K, mixing with GDC shows highest power density, hence effect of GDC content was examined. It is shown that adding 20 wt% GDC is effective in increasing power density for C_3H_8 fuel.

In Chapter 5, conclusion of this study was summarized and future view of SOFC was discussed.

Reference

(1) https://www.iea.org/publications/freepublications/publication/KeyWorld_Statistics_2015.pdf. Accessed on 2016 June 22nd.

(2) https://www.iea.org/Textbase/npsum/WEO2015SUM.pdf. Accessed on 2016 June 22nd.

(3) M.G. Bellino, J.G. Sacanell, D.G. Lamas, A.G. Leyva, de Reca New. J. Am. Chem. Soc. **129**, 3066 (2007).

(4) EG&G Services (2000), Fuel Cell Handbook. Parsons, Inc., Morgantown, West Virginiak.

(5) R. O'Hayre, S-W.Cha, W. Colella, F.B. Printz, 2006. Fuel Cell Fundamentals. Edition 1, Hoboken, New Jersey: John Wiley & Sons, Inc.

(6) A.B. Stambouli, E.S. Traversa, Renewable and Sustainable Energy Reviews **6**, 433 (2002).

(7) K. Sasaki, S. Adachi, K. Haga, M. Uchikawa, J. Yamamoto, A. Iyoshi, J.-T. Chou, Y. Shiratori, K. Itoh, ECS Trans. **7**(1) 1675 (2007).

(8) M. B. Pomfret, J. Marda, G. S. Jackson, B. W. Eichhorn, A.M. Dean, R.A. Walker, J. Phys. Chem. C, **112** (2008).

(9) R.J. Kee, H. Zhu, A.M. Sukeshini, G.S. Jackson, Combustion Science and Technology, **180**(6) (2008).

(10) R. J. Gorte, J. M. Vohs, Journal of Catalysis, **216**(1-2) (2003).

(11) T. Horita, H. Kishimoto, K. Yamaji, Y. Xiong, N. Sakai, M.E. Brito, H. Yokokawa, Solid State Ions., **177**, 1941 (2006).

(12) R. Ormerod, Fuels and Fuel Processing, in High Temperature Solid Oxide Fuel Cells: Fundamentals, Design, and Applications; S.C. Singhal and K. Kendell, Editors, (2003), Elsevier Ltd.: Bodmin.

(13) M. Mogensen, K. Kammer, Annu. Rev. Mater. Res. **33**, 321 (2003).

(14) K. Kendall, C.M. Finnerty, G. Saunders, J.T. Chung, J. Power Sources, **106**, 323 (2002).

(15) V.M. Janardhanan, V. Heuveline, O. Deutschmann, J. Power Sources, **172**, 296 (2007).

(16) S. Patel (2009). Performance of Ni/CeO_2/YSZ SOFC Anodes with Carbonaceous Fuels. Master of Science. University of Maryland, US.

(17) S. F. Corbin, R. M. Clemmer, Q. Yang, Ceramic Engineering and Science Proceedings, **26**(4) (2008).

(18) Z. Cheng, M.L. Liu, Solid State Ionics, **178**, 13 (2007).

(19) M. Yoshio, I. Yasuda, Solid State Ionics, **132**(3), 261 (2000).

(20) D.K. Niakolas, Applied Catalysis A: General, **486**, 123 (2014).

(21) A. Atkinson, S. Barnett, R.J. Gorte, J.T.S. Irvine, A.J. McEvoy, M. Mogensen, S. Singhal, J. Vohs, Nat. Mater., **3**, 17 (2004).

(22) J. Mirzababaei, S.S.C. Chuang, Catal., **4**(2), 146 (2014).

(23) S. Park, J.M. Vohs, R.J. Gorte, Nature, **404**, 265 (2000).

(24) S. McIntosh, R.J. Gorte, Chem. Rev. **104**, 4845 (2004).

(25) S. McIntosh, H. He, S.-I. Lee, O. Costa-Nunes, V.V. Krishnan, J.M. Vohs, R.J. Gorte, J., Electrochem. Soc. **151**, A604 (2004).

(26) R.T.K. Baker, M.A. Barber, P.S. Harris, F.D. Feates, R.J. Waite, J.Catal. **26**, 51 (1972).

(27) R.T.K. Baker, P.S. Harris, J. Henderson, R.B. Thomas, Carbon **13**, 17 (1975).

(28) R.T.K. Baker, P.S. Harris, S. Terry, Nature **253**, 37 (1975)

(29) C.W. Keep, R.T.K. Baker, J.A. France, J. Catal. **47**, 232 (1977).

(30) C.H. Bartholomew, Catal. Rev. Sci. Eng. **24**, 67 (1982).

(31) R.T.K. Baker, Carbon **27**, 315 (1989).

(32) T. Zhang, M.D. Amiridis, Appl. Catal. A **167**, 161 (1998).

(33) B. Monnerat, L. Kiwi-Minsker, A. Renken, Chem. Eng. Sci. **56**, 633 (2001).

(34) C.M. Chun, J.D. Mumford, T.A. Ramanarayanan, SOFC VI, in: S.C. Singhal, M. Dokiya (Eds.), Proceedings of the Electrochemical Society Series PV 1999-19, The Electrochemical Society, Pennington, NJ, (1999), p. 621.

(35) C.H. Toh, P.R. Munroe, D.J. Young, K. Foger, Mater. High Temp. **20**, 129 (2003).

(36) N.Q. Minh, T. Takahashi (1995), *Science and Technology of Ceramic Fuel Cells*. Amsterdam: Elsevier.

(37) L.F. Albright, B.L. Crynes, W.H. Corcoran (1983), *Pyrolysis: Theory and Industrial Practice*, pp. 47–87. New York: Academic.

(38) J.R. Rostrup-Nielsen (1984), *Catalytic Steam Reforming*. Berlin: Springer-Verlag.

(39) J.R. Rostrup-Nielsen, J. Sehested, J.K. Nørskov, Adv. Catal. **47**, 65 (2002).

(40) C.Y. Sheng, A.M. Dean, J. Phys. Chem. A **108**, 3772 (2004).

(41) Y. Lin, Z. Zhan, J. Liu, S.A. Barnett, Solid State Ionics, **176**(23), 1827 (2005).

(42) E. Perry Murray, T. Tsai, S.A. Barnett, Nature, **400**, 649 (1999).

(43) T. Takeguchi, Y. Kani, T. Yano, R. Kikuchi, K. Eguchi, K. Tsujimoto, Y. Uchida, A. Ueno, K. Omoshiki, M. Aizawa, J. Power Sources **112**, 588 (2002).

(44) K. Eguchi, H. Kojo, T. Takeguchi, R. Kikuchi, K. Sasaki, Solid State Ionics **152-153**, 411 (2002).
(45) K. Sasaki, Y. Teraoka, J. Electrochem. Soc. **150**, A878 (2003).
(46) K. Sasaki, Y. Teraoka, J. Electrochem. Soc. **150**, A885 (2003).
(47) T. Kim, G. Liu, M. Boaro, S.-I. Lee, J.M. Vohs, R.J. Gorte, O.H. Al-Madhi, B.O. Dabbousi, J. Power Sources, **155**, 231 (2006).
(48) T. Sperle, D. Chen, R. Lødeng, A. Holmen, Appl. Catal. A **282**, 195 (2005).
(49) Y. Zhang, K.J. Smith, Catal. Lett. **95**, 7 (2004).
(50) R. J. Gorte, S. Park, J. M. Vohs, C. Wang, Adv. Mater., **12**, 1465 (2000).
(51) S. Park, R. J. Gorte, J. M. Vohs, J. Electrochem. Soc., **148**, A443 (2001).
(52) Y. Huang, K. Ahn, J. M. Vohs, R. J. Gorte, J. J. Electrochem. Soc., **151**, A1592 (2004).
(53) Y. Ma, (2009). Ceria-based Nanocomposite Electrolyte for Low-Temperature Solid Oxide Fuel Cells. Licentiate Thesis. Royal Institute of Technology, Sweden.
(54) R. J. Gorte, H. Kim, J. M. Vohs, J. Power Sources, **106**(1-2), 10 (2002).
(55) T. Ishihara, H. Matsuda, Y. Takita, J. Am. Chem. Soc. **116**, 3801 (1994).
(56) A. Lasthabeg, S.J. Skinner, J. Materials Chem., **16**, 3161 (2006).
(57) M.D. Gross, J.M. Vohs, R.J. Gorte, J. Materials Chemistry, **17**, 3071 (2007).
(58) R. J. Gorte, J. M. Vohs, S. Mcintosh, Solid State Ion., **175**, 1 (2004).
(59) P. R. Slater, J. T. S. Irvine, T. Ishihara, Y. Takita, Solid State Ionics, **107**, 319 (1998).
(60) T. Ishihara, H. Minami, N. Matsuda, H. Nishiguchi, Y. Takita, Denki Kagaku, **64**, 642 (1996).
(61) T. Ishihara, T. Shibayama, M. Honda, H. Nishiguchi, Y. Takita, J. Electrochem. Soc., **147**, 1332 (2000).
(62) T.H. Shin, S. Ida, T. Ishihara, J. Am. Chem. Soc. **133**(48), 19399 (2011).
(63) S. An, C. Lu, W. L. Worrell, R. J. Gorte, J. M. Vohs, Solid State Ionics, **175**, 135 (2004).
(64) T. Ishihara, in Perovskite Oxide for Solid Oxide Fuel Cell: Fuel Cells and Hydrogen Energy, T. Ishihara, Editor, p. 3, Springer, New York (2009).
(65) S.M. Bukhari, J.B. Giorgi, J. Power Sources, **198**, 51 (2012).
(66) J. Hanna, W.Y. Lee, Y. Shi, A.F. Ghoniem, Progress in Energy and Combustion Science, **40**, 74 (2014).
(67) V.C. Belessi, A.K. Ladavos, P.J. Pomonis, Appl. Catal. B.: Environmental, **31**(3), 183 (2001).
(68) S. Tao, J.T.S. Irvine, Nature, **2**, 320 (2003).
(69) G. Kim, M.D. Gross, W. Wang, J.M. Vohs, R.J. Gorte, J. Electrochemical Soc., **155**(4), B360

(2008).
(70) Y. H. Huang, R. I. Dass, Z. L. Xing, J. Goodenough, Science, **312**, 254 (2006).
(71) T. Ishihara, M. Honda, T. Shibayama, H. Minami, H. Nishiguchi, Y. Takita J. Electrochem. Soc. **145**, 3177 (1998).
(72) T. Ishihara, H. Matsuda, Y. Takita, Solid State Ion., **79**, 147 (1995).
(73) T. Ishihara, T. Yamada, H. Arikawa, H. Nishiguchi, Y. Takita, Solid State Ion., **135**, 631 (2000).
(74) T. Ishihara, Y. Tsuruta, T. Todaka, H. Nishiguchi, Y. Takita, Solid State Ion., **152-153**, 709 (2002).
(75) S.P. Jiang, J. Mater. Sci., **43**, 6799 (2008).
(76) C. Lu, W. L. Worrell, J. M. Vohs R. J. Gorte, J. Electrochem. Soc., **150**, A1357 (2003).
(77) N. Kallel, N. Ihzaz, S. Kallel, A. Hagaza, M. Oumezzine, J. Magn. Magn. Mater. **321**, 2285 (2009).
(78) A. Hammouche, E.J.L. Schouler, M. Henault, Solid State Ions. **28**, 1205 (1988).
(79) H.A. Taroco, J.A.F. Santos, R.Z. Domingues, T. Matencio, in Advances in Ceramics - Synthesis and Characterization, Processing and Specific Applications, C. Sikalidis, Editor, p. 428, InTech (2011).
(80) K. Kamata, T. Nakajima, T. Hayashi, T. Nakamura, Mat. Res. Bull. **13**, 49 (1978).
(81) M. Al Daroukh, V.V. Vashook, H. Ullmann, F. Tietz, I. Arual Raj, Solid State Ions. **158**, 141 (2003).
(82) J. Mizusaki, N. Mori, H. Takai, Y. Yonemura, H. Minamiue, H. Tagawa, M. Dokiya, H. Inaba, K. Naraya, T. Sasamoto, T. Hashimoto, Solid State Ions. **129**, 163 (2000).
(83) J.H. Kuo, H.U. Anderson, J. Solid State Chem., **87**, 55 (1990).
(84) T. Ishihara, S. Fukui, M. Enoki, H. Matsumoto, J. Electrochem. Soc. **153**(11), A2085 (2006).
(85) X.M. Ge, S.H. Chan, Q.L. Liu, Q. Sun, Advanced Energy Mater., **2**, 1156 (2012).

Chapter 2

Al doped $La_{0.5}Sr_{0.5}MnO_3$ as a New Oxide Anode for Direct Hydrocarbon Type SOFC

2.1 Introduction

As has been discussed in Chapter 1, Ni-YSZ cermet anode has been widely used up to now and exhibits excellent electrocatalytic activity towards oxidation of H_2, however, it is also active towards carbon formation or coking when operates in hydrocarbon fuel.[1-5] Hence, the Ni-based cermet easily forms coke resulting in the deactivation of the cell or in more serious case separation of Ni whiskers from the cermet which damage the anode.[6-8] When, hydrocarbon higher than ethane is used the coke deposition is more severely occurred.[9] Despite the proposed utilization of internal reforming or strict operation in a specific thermodynamic regime, both solutions are still not completely practical which produce other array of problems.[10, 11] Therefore, to realize a direct hydrocarbon type SOFC, alternative anode with highly tolerant to coke deposition is required. It has been reported that a direct oxidation is possible when the anode is inert for coking or carbon deposition.[12]

Despite commonly known as cathode material for SOFC, $La_{0.5}Sr_{0.5}MnO_3$ (LSM55) has been widely used for cathode but also demonstrated to be highly active as anode for H_2 oxidation.[13] Being a perovskite oxide, it is a suitable candidate as anode for hydrocarbon fuels because their lattice oxygen provides a potential carbon cleaning mechanism depending on the chemical composition of the perovskite.[14] Additionally, LSM55 is specifically chosen because its characteristics are well documented and possess the highest electrical conductivity amongst Sr-doped $LaMnO_3$.[15-16] However, while LSM55 is stable under oxidising condition, it decomposes under reducing environment (decomposition at 1273 K for $P_{O2} < 10{-}14$) mainly into Sr_2MnO_4 and La_2MnO_4 which both have negligible power density.[17-18] Hence, in order for LSM55 to succeed as an anode especially in highly challenging hydrocarbon environment, the phase stability of $LaMnO_3$ needs to be increased.

In this chapter, the effects of various dopants in the Mn site of $La_{0.5}Sr_{0.5}MnO_3$ (LSM55) on their stability in reducing atmosphere by using dry C_3H_8 are investigated. The phase stability are determined by semi-quantitative calculation of the $LaMnO_3/(La,Sr)_2MnO_4$ phase peak ratio. In addition, dopant effects on the anodic performance when using hydrocarbon fuel is characterized to gauge their feasibility as a direct hydrocarbon anode for SOFC. Among the dopant, it was found that substitution of Al is effective in increasing the stability of $LaMnO_3$ phase in LSM55 and reasonable power density was exhibited when dry C_3H_8 was used for fuel. Further study is conducted to improve the power density of the anode by varying the Al content of the doped LSM55.

2.2 Experimental

2.2.1 Sample preparation

$La_{0.5}Sr_{0.5}MnO_3$ (LSM55) and B-site doped $La_{0.5}Sr_{0.5}Mn_{0.9}A_{0.1}O_3$ (A: Ni, Co, Fe, Ce, Cu, Sc, In, Sb, Al, Ga) were synthesized by using sol-gel combustion method of $La(NO_3)_3.6H_2O$ (99.9% Wako Pure Chemical Co. Ltd., Japan), $SrNO_3$ (98% Chameleon Reagent, Japan), $Mn(NO_3)_2.6H_2O$ (99.9% Wako Pure Chemical Co. Ltd., Japan) and the corresponding metal nitrates. Citric acid, $C_6H_8O_7.H_2O$ (99.5% Wako Pure Chemical Co. Ltd., Japan) was added as the chelating agent. The addition of citric acid has been reported to be beneficial in obtaining finely powdered perovskite oxides by decreasing the crystallization temperature of the perovskite.[19] The precursor was calcined at 673 K followed by calcination at 1523 K to achieve pure phase.

$LaGaO_3$-based oxide, $La_{0.9}Sr_{0.1}Ga_{0.8}Mg_{0.2}O_3$ (LSGM) and $Sr_{0.5}Sm_{0.5}CoO_3$ (SSC) were used for electrolyte and cathode, respectively and the oxides were prepared by conventional solid-state reaction method. The commercial oxides of La_2O_3 (99.9% Kishida Chemical Co., Japan), Ga_2O_3

(99.9% Mitsubishi Materials Corporation, Japan), MgO (99.9% Wako Pure Chemical Co. Ltd., Japan), and $SrCO_3$ (99.9% Kishida Chemical Co., Japan) were mixed in alumina mortar for the preparation of $LaGaO_3$-based oxide. The obtained powder mixture was pre-calcined at 1273 K for 6 h, pelletized before fired at 1773 K for 6 h. Similarly, $Sr_{0.5}Sm_{0.5}CoO_3$ for cathode was prepared by solid state reaction method using commercial $Sr(CH_3COO)_2.0.5H_2O$ (99% Wako Pure Chemical Co. Ltd., Japan), Sm_2O_3 (99.9% Nacalai Tesque Inc., Japan) and $Co(NO_3)_2.6H_2O$ (98% Wako Pure Chemical Co. Ltd., Japan). After pre-calcination at 673 K, the powder was fired at 1273 K in air.

All samples prepared were analyzed with commercial diffractometer XRD (Rigaku, RINT2500) with Cu K_α line for phase identification. The particle size of the powder samples were estimated using Scherrer's equation. In order to measure the porosity and the surface area of LSM55 and doped LSM55, Brunauer-Emmet-Teller (BET) measurement was carried out through N_2 adsorption/desorption by using Belsorp mini (Microtrac Bell Co. Ltd). Electrical conductivity test specimen with rectangular shape was prepared by sintering at 1523 K for 6 h and the electrical conductivity was measured in air and 1% H_2/Ar gas flow (100 mL/min) with dc four-probe method.

2.2.2 Measurement of anodic performance

The oxide anodes and cathode were made into paste for screen printing by mixing with ethyl cellulose (N7 grade) as a binder and isobutyrate as the solvent prior to preparation of single cell. The ingredient was then homogenized by using a mixer. The electrolyte-supporting single cell using LSGM (ca. 0.3 mm thickness) electrolyte was prepared by screen printing of the prepared doped LSM55 and SSC for anode and cathode, respectively (ø 5 mm in diameter). After painting and dry, the cell was calcined at 1373 K for 30 min to remove organic solvent. Platinum mesh (5×5 mm) was pressed on

top of the anode as current collector, and it is to be noted that almost no power density was obtained by using Pt mesh for anode. Reference electrode was set close to the cathode by using the commercial Pt paste (Tanaka TR7902). Platinum lead wire was connected to the Pt reference electrode.

Power generating property of the cell was measured with the four-probe method with humidified hydrogen (3%H_2O/H_2) followed by feeding dry C_3H_8 (100 mL/min) as the fuel. N_2 gas is purged for 40 min before dry C_3H_8 is introduced. Commercial O_2 without purification was fed to the air side (100 mL/min). Constant dc current was applied with galvanostat (Hokuto Denko HA-151A) and the terminal voltage was measured with digital multimeter (Advantest, type R 6451A). Internal resistance was estimated with current interruption method and dc current pulse was generated with current pulse generator (Nikko Keisoku, NCPG 10-1) and potential response was measured with digital memory recorder (Hioki 8835). The electrode resistance was also evaluated by the impedance measurement using the impedance/gain-phase analyzer (Solartron type 1255B, Solartron) with the electrochemical interface (Solartron type 1287, Solartron).

Analysis of the phase stability of the anode after power generation measurement was performed by using XRD after the measurement has ended. In order to ensure reducing state is maintained, N_2 gas is continuously purged during the cooling of the cell. The microstructure of the anode before and after the reduction was investigated by using scanning electron microscope (SEM) (VE-7800, Keyence Co.) with Energy Dispersive Spectrometry (EDS) instrument (EDAX Co., Ltd.) for elemental analysis.

2.3 Results and Discussion

2.3.1 Effects of various dopant on the B-site of $La_{0.5}Sr_{0.5}MnO_3$ to the power generating property of the cell

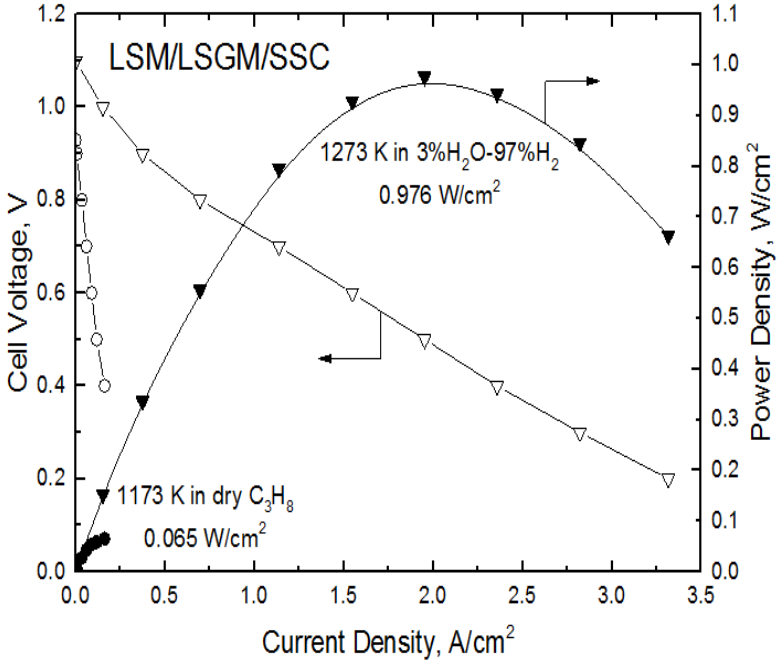

Figure 2.1 *I-V*/*I-P* curve of the LSM55 as anode in humidified H_2 and dry C_3H_8

Figure 2.1 shows the power generation curve of the cell using $La_{0.5}Sr_{0.5}MnO_3$ (LSM55) for anode at 1273 K when $3\%H_2O/H_2$ was used for fuel. As already reported on the cell using $La_{0.9}Sr_{0.1}Ga_{0.8}Mg_{0.15}Co_{0.05}O_3$ (LSGMC), almost theoretical open circuit potential was exhibited and the maximum power density close to 1 W/cm^2 was achieved on LSM55. Therefore, as already reported, LSM55 has reasonable activity to electrochemical oxidation of H_2. On the other hand, *I-V*, *I-P* curves of the same cell is shown in Fig.1 when dry C_3H_8 was used instead of humidified H_2 at 1173 K. Open circuit potential was decreased to be 0.92 V which is much smaller than that of theoretical one (1.12 V) for assuming reaction $C_3H_8+5O_2 \rightarrow 3CO_2 + 4H_2O$. Therefore, although LSM55 shows reasonable activity to H_2 oxidation, that for dry C_3H_8 is much smaller. This may be explained by the insufficient

surface catalytic activity to oxidation of hydrocarbon. In addition, XRD measurement after power generation measurement shows that diffraction peaks from La_2MnO_4 phase and $SrMnO_3$ phase was observed, although intensity is not strong. Therefore, LSM55 is active to electrochemical oxidation of H_2, however, stability is also required to be increased. In order to increase the surface activity and chemical stability against reduction, partial substitution of Mn in LSM55 was studied in the following part.

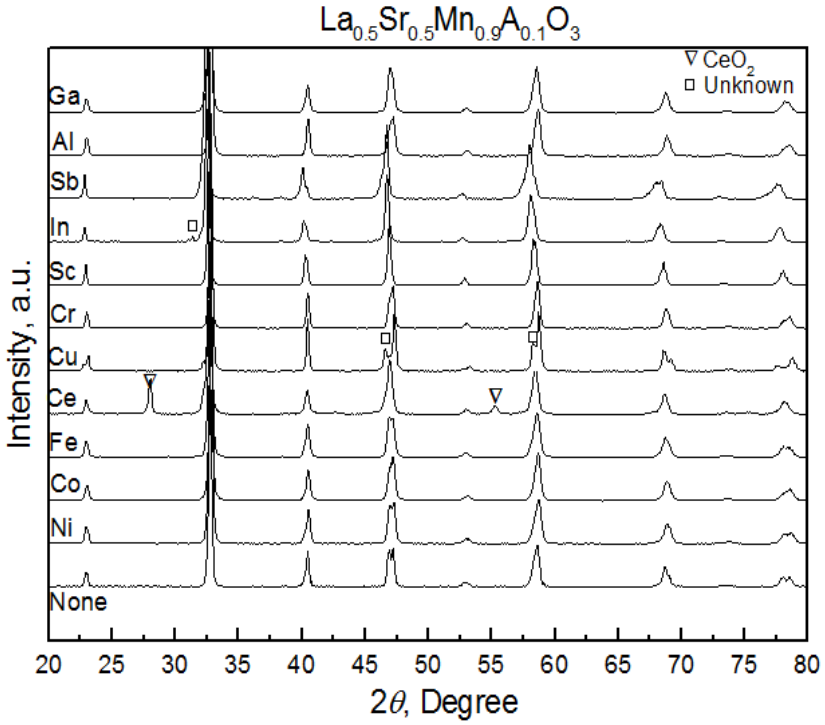

Figure 2.2 XRD pattern of $La_{0.5}Sr_{0.5}Mn_{0.9}A_{0.1}O_3$ (A = Ni, Co, Fe, Ce, Cu, Sc, In, Sb, Al, Ga)

Figure 2.2 shows the XRD patterns of $La_{0.5}Sr_{0.5}Mn_{0.9}A_{0.1}O_3$ (A = dopant). With exception of Ce-doped LSM55, all observed diffraction peaks were assigned to those of LSM55 even though shift in diffraction peaks was also observed by dopant suggesting changes in lattice parameter. However, doping of Ce on the B-site formed CeO_2 phase due to significantly larger ionic radius of Ce^{4+} (0.87

nm) compared to Mn^{3+} (0.58 nm).[20] However, other doped cations seems to be successfully substituted the Mn site of LSM55.

Table 2.1 Effect of metal dopant on power density of the cell using C_3H_8 as the fuel

$La_{0.5}Sr_{0.5}Mn_{1-x}A_xO_3$ A	OCV (mV)	MPD (mW/cm^2)	$La_{0.5}Sr_{0.5}Mn_{1-x}A_xO_3$ A	OCV (mV)	MPD (mW/cm^2)
None	929	64.8	Cr	956	115.8
Ni	1017	221.0	Sc	900	113.7
Co	971	208.4	In	913	111.6
Fe	1011	139.0	Sb	904	107.4
Ce	1105	139.0	Al	972	100.0
Cu	983	127.4	Ga	930	79.0

cathode: SSC electrolyte: LSGM

Power generation property of the cell using dry C_3H_8 was measured by using doped LSM55 for anode. Table 2.1 summarized the performance of the cell using doped LSM55 anodes when dry C_3H_8 was fed at 1173 K. Obviously, open circuit potential increased by using doped LSM55 and this suggests that the activity to electrochemical oxidation of C_3H_8 was increased by dopant. On the other hand, maximum power density (MPD) is also increased by dopant and the largest MPD of 221 mW/cm^2 which is ca. 5 times larger than that of the non-doped LSM55 anode was exhibited on the cell using Ni doped LSM55. Since it is well known that Ni is active towards hydrocarbon oxidation, the large power density of the cell using Ni doped LSM55 anode is reasonable. However, considering the stability of LSM55, metallic Ni may be deposited under operating condition and contribute to the increased power density. Disadvantage of Ni is formation of coke and in fact, power density of the cell

was gradually decreased with time which may be assigned to the deactivation of anode by coke deposition.[21] This is also the same trend for Co doped LSM55. Therefore, although much higher initial MPD was exhibited on the cell using LSM55 doped with Ni, Co, and Fe, these oxides seem not to be suitable as anode of the cell using dry C_3H_8 fuel. In contrast, MPD of the cell using LSM55 doped with Al, and Ga which is the same valence number of Mn, was also increased by two times comparing with that of non-doped one. Since Al or Ga is not catalytically active for hydrocarbon oxidation, increase in power density may not be the same with that of doping with transition metal like Ni or Co. Therefore, mechanism for increased power density of LSM55 with doping Al is interesting and further detail study was performed.

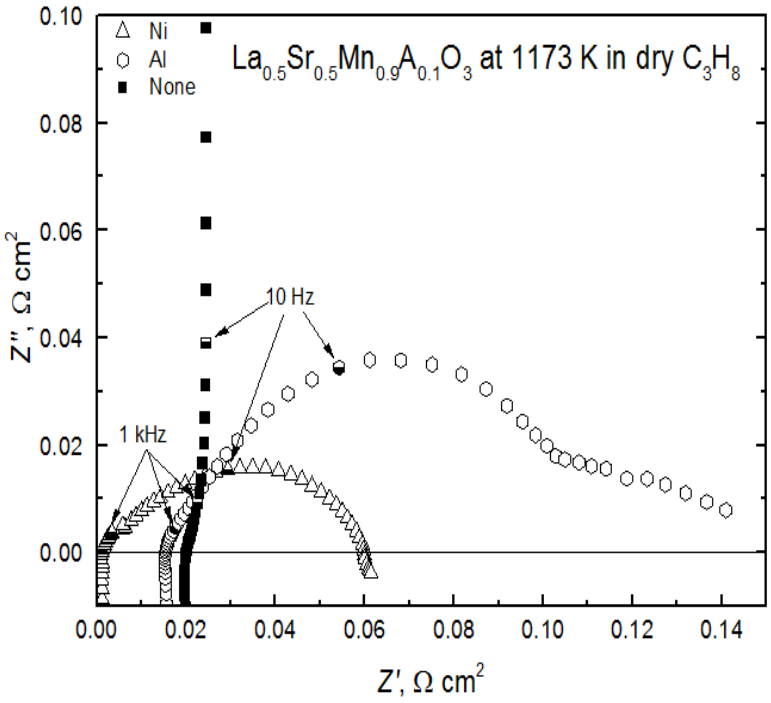

Figure 2.3 Impedance plots of LSM55, LSM55 doped with Al or Ni anode of the cell using C_3H_8 at 1173 K

Figure 2.3 shows comparison of anodic impedance of LSM55 and that doped with Al and Ni when dry C_3H_8 was fed as fuel under open circuit condition. Obviously, by doping Ni, resistance loss (IR) which is estimated from real axis intercept at higher frequency was shifted to lower value and the impedance arc was decreased by doping Ni, suggesting that electrical conductivity and surface activity was increased by doping Ni and this is also suggested that metallic Ni was deposited from lattice of LSM55 under working condition. On the other hand, IR loss is also decreased by addition of Al, and so it is considered that electrical conductivity may not be increased by doping Al considering the same valence number of Al^{3+} and Mn^{3+}. Therefore, decreased IR loss could be assigned to the improved contact between anode and electrode. On the other hand, large diffusion overpotential was observed for Al doped LSM55 and so surface activity is still not high when doped with Al.

2.3.2 Effect of Al-doped $La_{0.5}Sr_{0.5}MnO_3$ on phase stability and power generating property

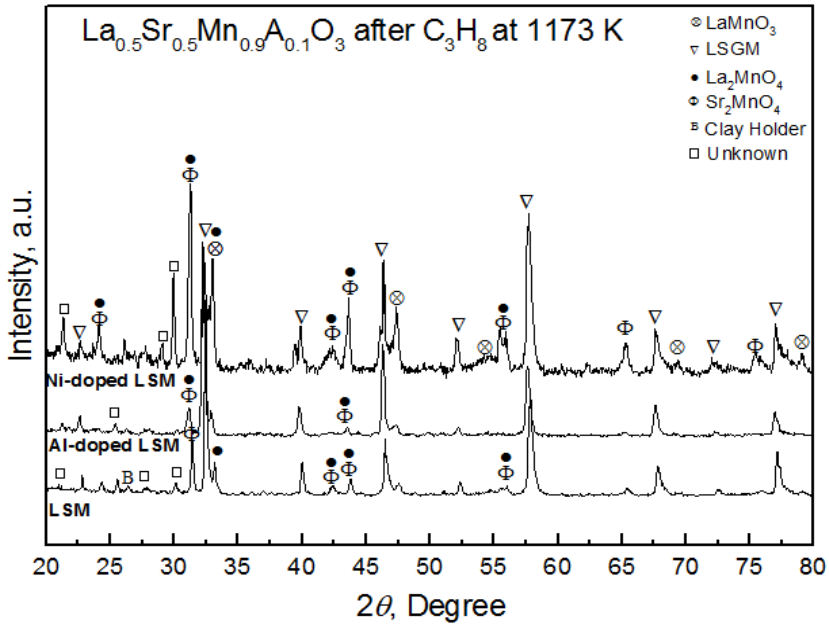

Figure 2.4 XRD spectrum of LSM55, $La_{0.5}Sr_{0.5}Mn_{0.9}Al_{0.1}O_3$ (LSMAl-5591) and $La_{0.5}Sr_{0.5}Mn_{0.9}Ni_{0.1}O_3$ (LSMNi-5591) after power generation measurement

Figure 2.4 represents the XRD patterns of LSM55, Ni and Al doped LSM55 after reduction at 1173 K in C_3H_8. As already reported, although main peak in XRD of LSM55 after reduction was $LaMnO_3$ perovskite, strong peaks assigned to La_2MnO_4 were observed suggesting that phase separation of $LaMnO_3$ to MnO and La_2MnO_4. On the other hand, as shown in Fig. 2.4, doping Al for Mn site is effective for increasing the stability of perovskite phase because intensity ratio of $LaMnO_3/La_2MnO_4$ main peak was 0.62 which is 1.7 times higher than that of non-doped LSM55 (peak ratio was 0.36). Therefore, it seems that doping Al for Mn site is effective for increasing the stability of perovskite phase against reduction. Optimization of Al substitute to Mn site of $LaMnO_3$ was further studied.

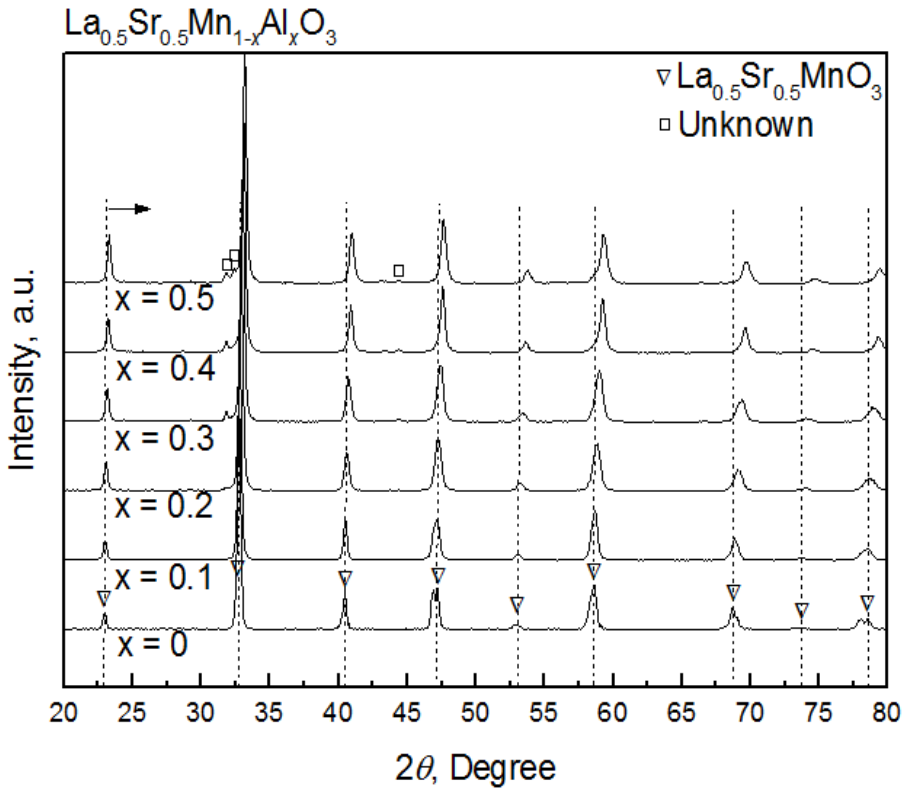

Figure 2.5 XRD patterns of as-prepared $La_{0.5}Sr_{0.5}Mn_{1-x}Al_xO_3$ (x = 0.1-0.5)

The XRD patterns of $La_{0.5}Sr_{0.5}Mn_{1-x}Al_xO_3$ (x = 0.1-0.5) (denoted as LSMA) is shown in Fig. 2.5. Crystal structure of $La_{0.5}Sr_{0.5}MnO_3$ is determined to be tetragonal and the partial substitution by aluminum of the B-site cation for manganese has caused lattice parameter shrinkage owing to smaller ionic radius of Al^{3+} (0.535 nm) compared to Mn^{3+} (0.58 nm (low spin) and 0.645 nm (high spin)) at coordination number of 6. [20, 22] Consequently, the diffraction peaks were shifted to higher angle with increasing Al content. When Al is increased, some diffraction peaks which were split into two, were changed to a single one suggesting the crystal structure changes from hexagonal to tetragonal. Single phase is obtained with no secondary phase up to x = 0.2. However, trace of secondary phase appeared from x = 0.2 at 2θ = 33° and more obviously observed with increasing Al dopant. However, even at x = 0.4, diffraction peaks from secondary phase are not significant and so amount of secondary phase seems not to be large up to x = 0.4.

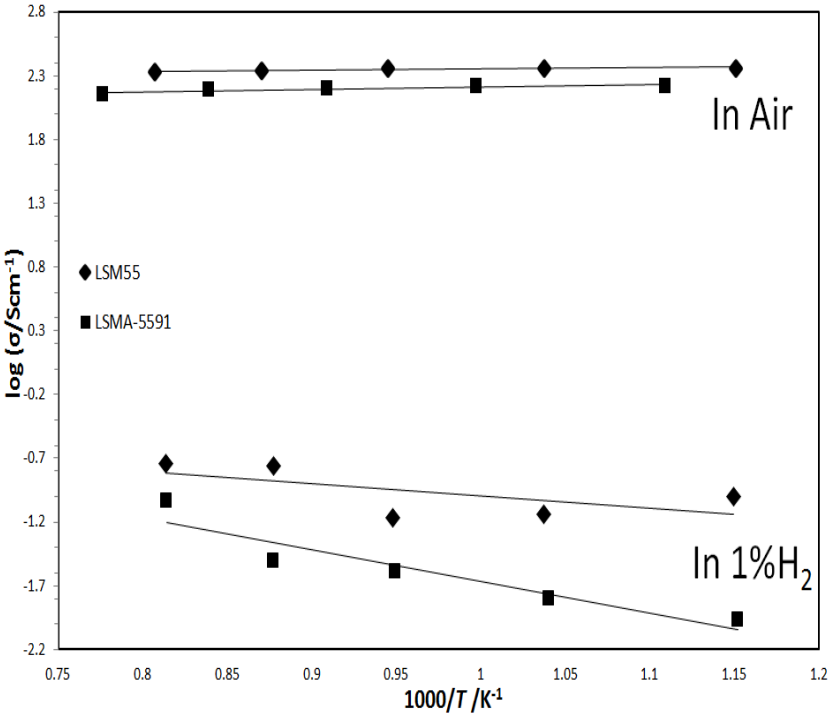

Figure 2.6 Electrical conductivity of LSM55 and LSMA-5591 in air and 1%H_2-99%Ar

Figure 2.6 shows the temperature dependence of electrical conductivity of LSM55 and LSM55 doped with 10 mol% Al in air and 1% H_2-Ar atmosphere. LSM55 is a well-known hole conductor in air and the measured value matched well with the literature[15]. Electronic hole is formed in LSM55 according to the following equation,

$$\frac{1}{2}O_2 \leftrightarrow O_i'' + 2h^{\cdot} \qquad (2\text{-}1)$$

Expectedly, the conductivity decreased in the reducing 1%H_2-Ar atmosphere. In a similar manner with LSM55, electrical conductivity of Al doped sample decreased with decreasing P_{O2}. Hence, it can be confirmed that electronic hole is still dominant in LSM55 doped with Al. Evidently, total conductivity was decreased by doping Al in both air and 1%H_2-Ar atmosphere. Considering the stable valence number of Al^{3+}, decrease in conductivity could be explained by the shift in chemical equilibrium shown in eq. (1) to left side.

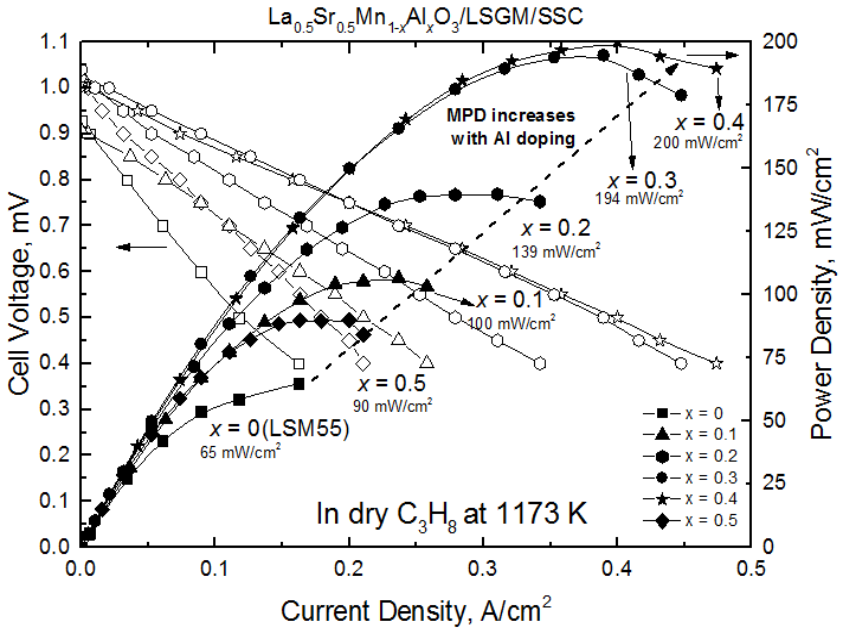

Figure 2.7 *I-V, I-P* curve of the cell using $La_{0.5}Sr_{0.5}Mn_{1-x}Al_xO_3$ (x = 0-0.5) anode using dry C_3H_8 for fuel

On the other hand, Figure 2.7 shows *I-V* and *I-P* curves of the cell using LSM55 doped with different amount of Al for anode. It is apparent that the power density of the cell increased with increasing Al amount when operating in dry C_3H_8 gas. The power density of the cell increases with increasing Al amount doped for LSM55 from x = 0.1 to x = 0.4, and achieved the highest maximum power density of 0.2 W/cm^2 at x = 0.4 and then decreased. In addition, OCV is also increased with increasing Al amount. At x = 0, OCV of the cell is around 972 mV and it increased to a value of 1008 mV at x = 0.4. Therefore, it is considered that the surface activity of LSM55 to electrochemical oxidation reaction is also increased with increasing Al content.

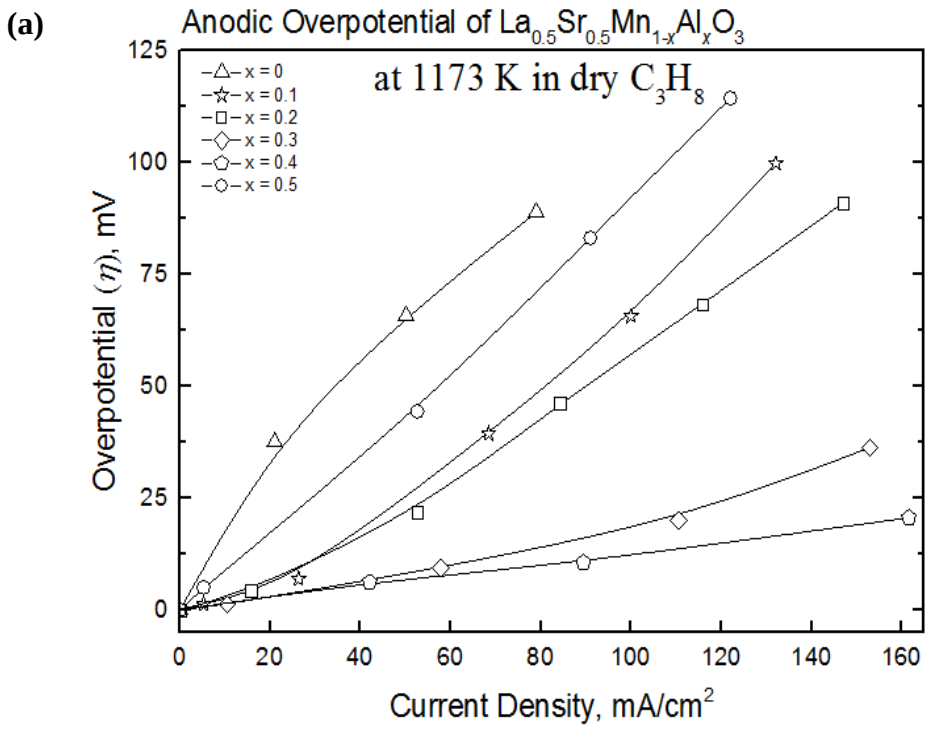

Figure 2.8 (a) Anodic overpotential of $La_{0.5}Sr_{0.5}Mn_{1-x}Al_xO_3$ (x = 0-0.5) anode as a function of current density in C_3H_8 at 1173 K

(b)

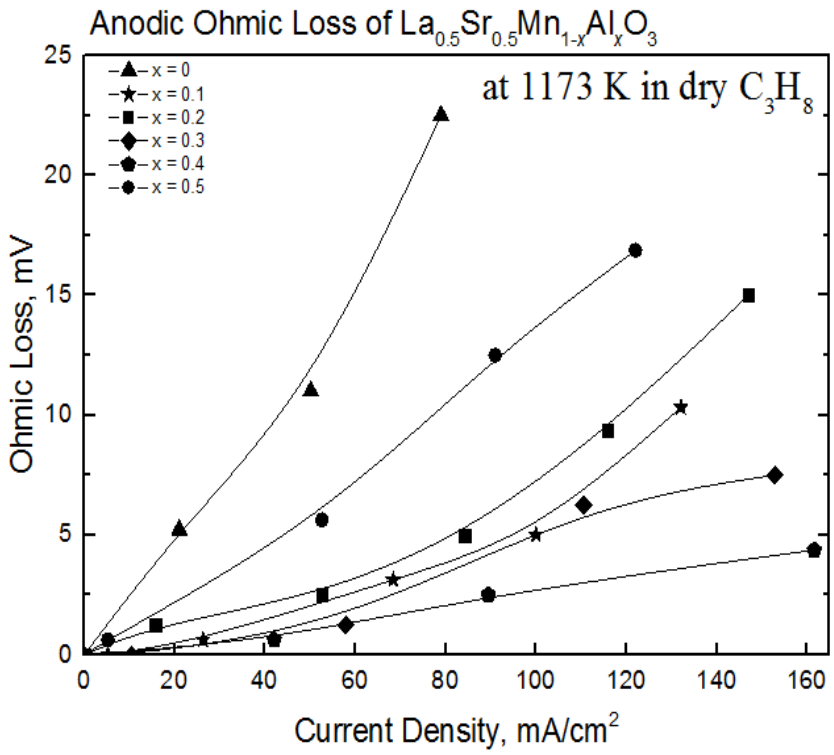

Figure 2.8 (b) Potential drop by IR loss

Figure 2.8 (a) and (b) shows the comparison of internal resistance of the cell as a function of current density. Obviously, the largest internal resistance was anodic overpotential which suggests that the low activity of LSM55 to C_3H_8 electrochemical oxidation (Fig. 2.8 (a)). It is found that the anodic overpotential was much decreased by addition of Al and it became minimum at x = 0.4, and so the surface activity of LSM55 against C_3H_8 oxidation was increased by doping Al which is low catalytic activity. Therefore, increased power density of the cell by using Al doped LSM55 was explained by decreased anodic overpotential. On the other hand, comparing with anodic overpotential, IR loss was much smaller (Fig. 2.8 (b)). Here, it is considered that IR loss was mainly assigned to resistance of LSGM electrolyte because the thickness of the electrolyte used was as thick as 0.3 mm. However, due to the low electrical conductivity of LSM55 in C_3H_8, the observed IR loss is much larger than that of

IR loss estimated from electrical conductivity of LSGM. Obviously, IR loss of the cell is also decreased by using LSM55 doped with 40 mol% Al for anode and this suggests that the interface resistance between LSM55 and LSGM was decreased by doping Al because the increased stability against the reduction is also an effective against preventing LSM55 electrode delamination. Therefore, increase in power density of the cell was mainly assigned to the decreased anodic overpotential and IR loss at anode side. Since Al_2O_3 is inactive to hydrocarbon oxidation, mechanism for decreased anodic overpotential by doping Al is interesting.

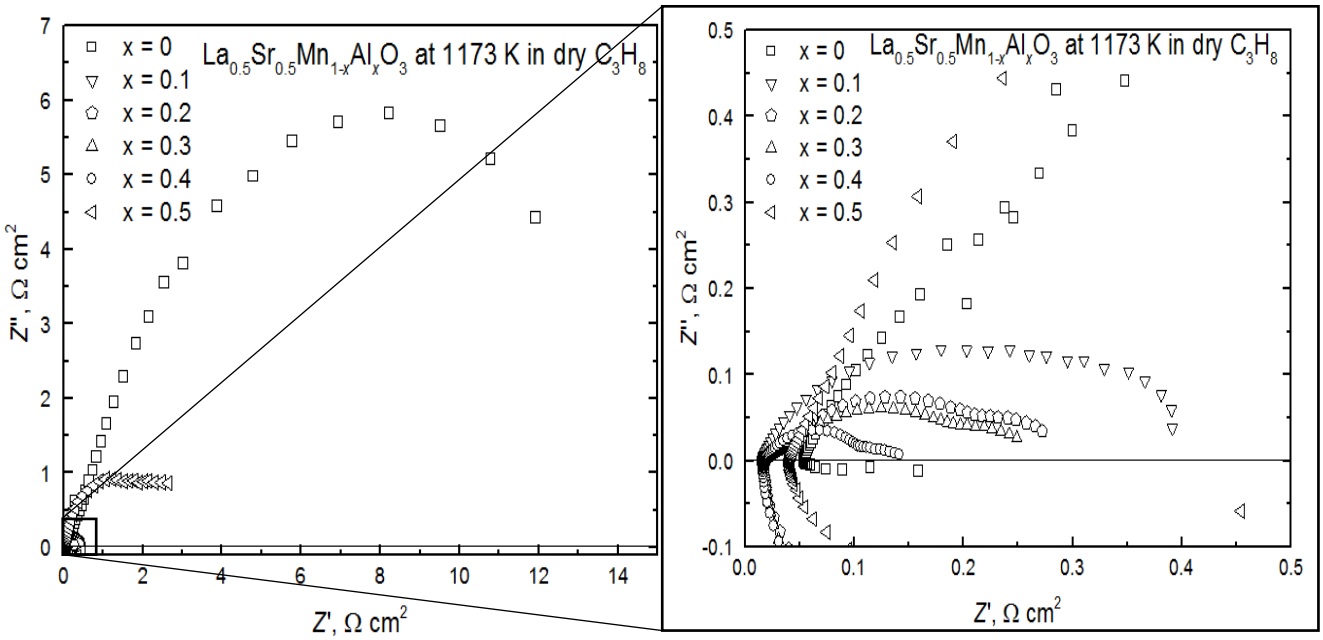

Figure 2.9 Impedance plots of $La_{0.5}Sr_{0.5}Mn_{1-x}Al_xO_3$ anode under open circuit condition at 1173 K in dry C_3H_8

Figure 2.9 shows the anodic impedance plots of LSM55 doped with various Al content under open circuit condition. Apparently, the observed impedance arcs were decreased with increasing Al amount doped for Mn site of LSM55 and it became the smallest at x = 0.4 which shows the largest power density. The impedance arc of Al doped LSM55 is consisted of two semicircles, higher and

lower frequency region. As shown in Figure 2.9, the size of semicircle at higher frequency was not significantly changed, however, that at lower frequency was decreased significantly. In general, impedance semicircle at higher frequency region represents the surface activity and the lower is concentration overpotential or diffusion resistance. Therefore, doping Al is effective for decreasing diffusion resistance which may be assigned to the larger reaction area. BET surface area and average particle size of LSM55 doped with Al which is estimated with line broadening method were shown in Table 2.2. Apparently, not only BET surface area but also the average particle size were almost the same between Al doped and non-doped LSM55 and so doping Al may not change the geometrical reaction area before power generation measurement.

Table 2.2 BET surface area and average particle size of $La_{0.5}Sr_{0.5}MnO_3$ (LSM55) and $La_{0.5}Sr_{0.5}Mn_{0.6}Al_{0.4}O_3$ (LSMA64) synthesized by sol-gel combustion method

	BET surface area (m^2g^{-1})	Pore volume (cm^3g^{-1})	Average particle size* (nm)
LSM55	31.4	0.045	27.4
LSMA64	32.8	0.064	29.2

*estimated by using Scherrer equation.

Figure 2.10 (a) shows the XRD patterns of the LSM55 doped with Al after the power generation measurement. Although diffraction peaks from LSGM are close to those of LSM55, diffraction peaks assigned to $LaMnO_3$ of which main diffraction peak was observed around 33°, were more significantly observed with increasing Al content. This suggests that substitution of Mn site with Al increased the stability against reduction and $LaMnO_3$ perovskite phase became stable in reducing

atmosphere because of stable valence number of Al^{3+}. In order to confirm the phase retention of $LaMnO_3$, 40 mol% Al-doped LSM55 (LSMA64) is fired at 1173 K under flowing C_3H_8 gas and the XRD pattern of the oxide is shown in Figure 2.10 (b). It can be seen clearly that the perovskite phase of $LaMnO_3$ can still be observed and so it was seen that perovskite phase was stabilized by Al doping and this is main reason for increasing power density.

(a)

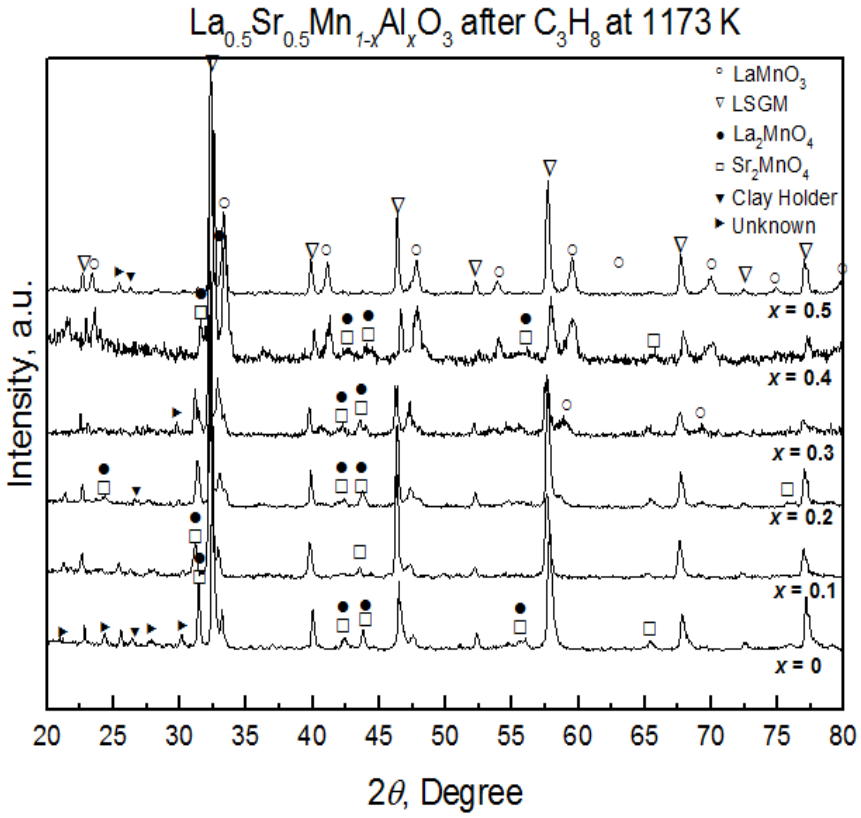

Figure 2.10 (a) XRD patterns of $L_{0.5}Sr_{0.5}Mn_{1-x}Al_xO_3$ after power generation measurement

(b)

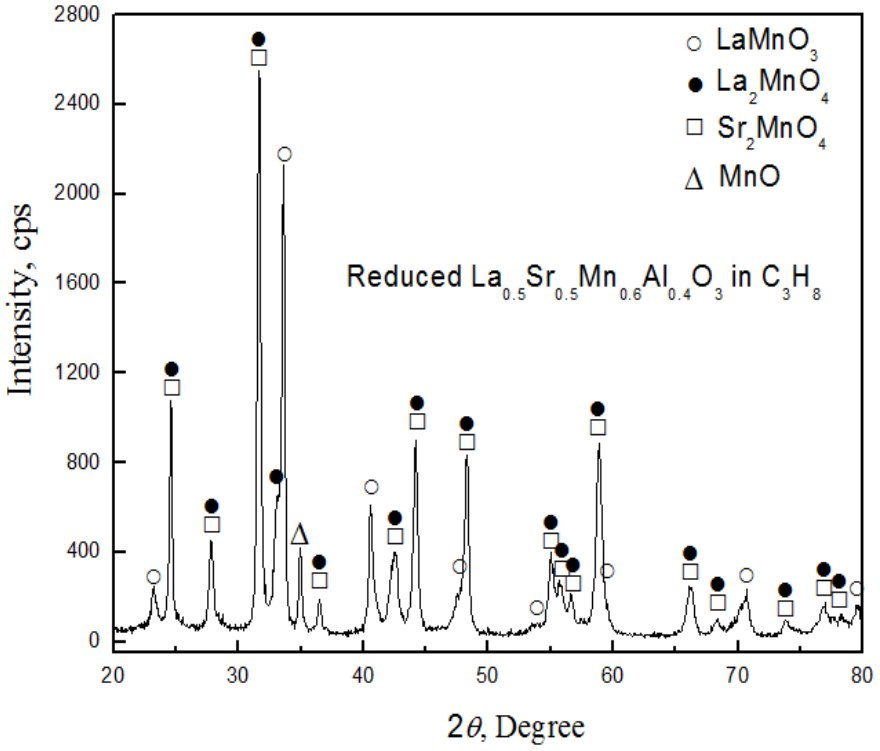

Figure 2.10 (b) XRD pattern of $La_{0.5}Sr_{0.5}Mn_{0.6}Al_{0.4}O_3$ after reduction in dry C_3H_8 at 1173 K

Figure 2.11 shows the SEM images of LSM55 and Al doped LSM55 before and after power generation measurement. Before measurement, in case of LSM55 in Fig. 2.11 (a), uniform electrode film with fine particle was observed. However, after measurement in Fig. 2.11 (c), aggregation and more dense structure occurred which explained the large diffusion resistance of LSM55. In contrast, similar fine particle and porous structure was still sustained after measurement in case of Al doped one (Fig. 2.11 (b) and (d)). Therefore, much smaller particle sizes were sustained by doping Al. Considering the low catalytic activity of Al but increased surface activity to C_3H_8 oxidation by doping, increased stability of $LaMnO_3$ perovskite structure in C_3H_8 atmosphere seems to be important role. Therefore, compared to La_2MnO_4, it is considered that $LaMnO_3$ might be active to C_3H_8 oxidation resulting in the much decreased anodic overpotential by partial substitution of Mn with Al which is stable against reduction.

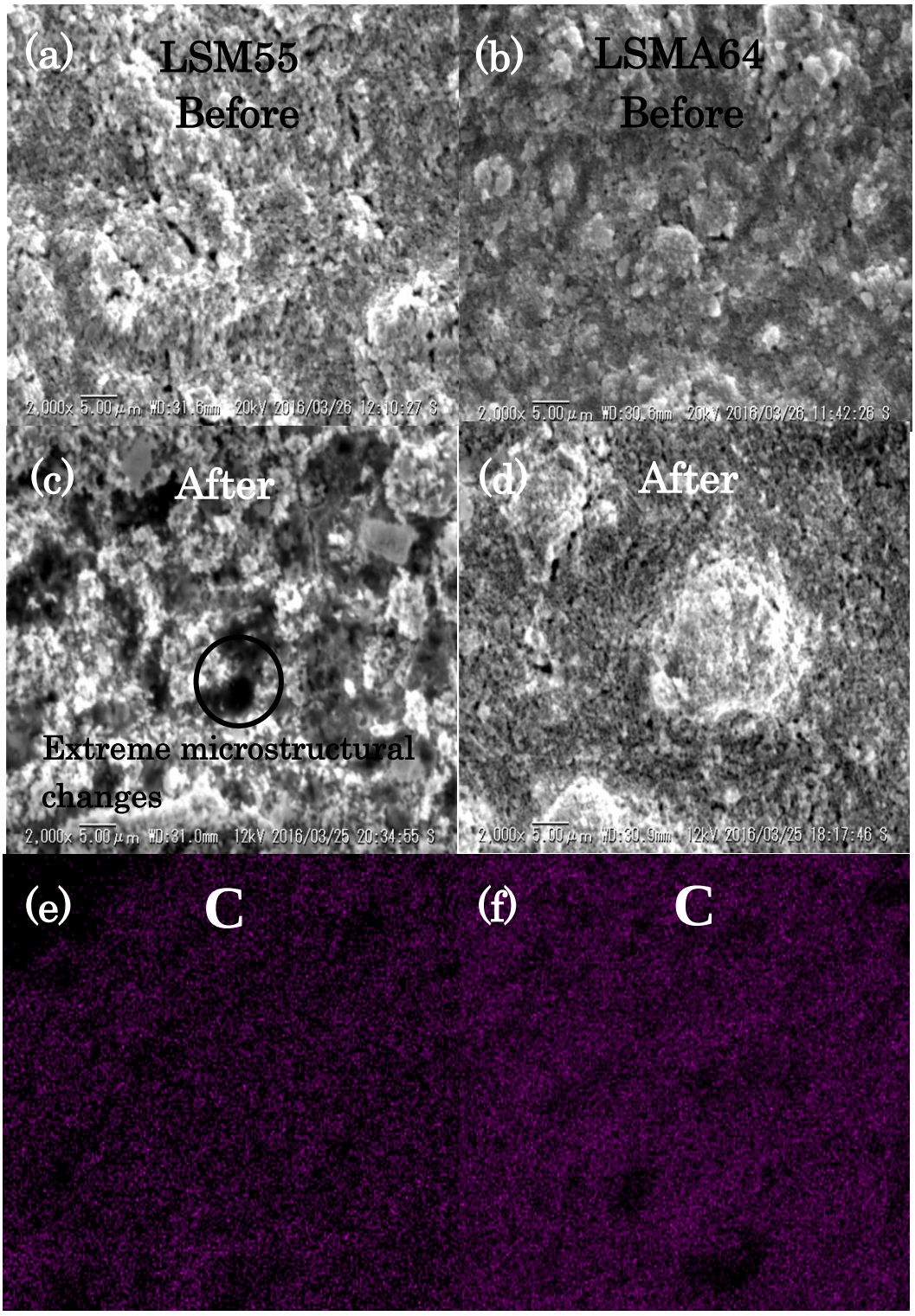

Figure 2.11 SEM and EDS surface images of (a), (c) & (e) $La_{0.5}Sr_{0.5}MnO_3$ and (b), (d) & (f) $L_{0.5}Sr_{0.5}Mn_{0.6}Al_{0.4}O_3$

It is also noted that no filament-like deposits were observed as shown in Figure 2.11 (c) and (d) and the color of LSM55 electrode was dark black and does not changed suggesting that no coke deposition was recognized. EDS scanning in both Figure 2.11 (e) & (f) also confirmed that no distinctive carbon structure characteristics appear on the anodes surface after power generation test using C_3H_8 fuel. Clearly from this result, the study revealed that Al doping improved the phase stability of LSM55 and consequently enhance its activity for direct C_3H_8. Since there is no coke deposition observed, Al-doped LSM55 is feasible to be used as anode for direct hydrocarbon SOFC. Further proof is shown by the cross section of both cells in Figure 2.12 that clearly reveal no delamination happen which usually occurs due to amongst other from the growth or expansion of carbon formation.

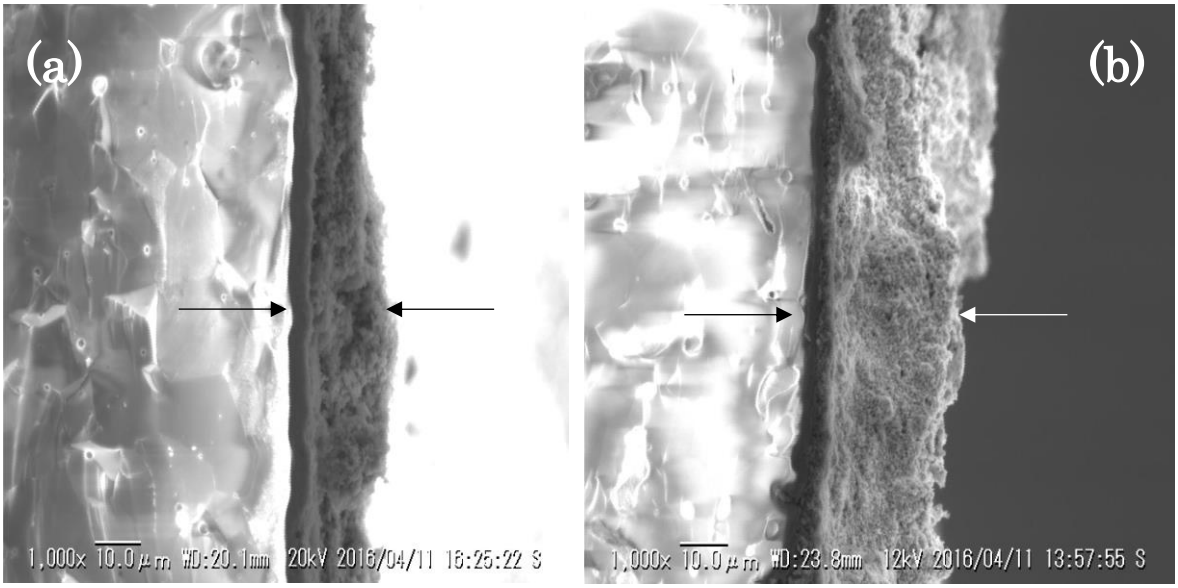

Figure 2.12 SEM images of cell cross section after measurement (a) $La_{0.5}Sr_{0.5}MnO_3$ and (b) $L_{0.5}Sr_{0.5}Mn_{0.6}Al_{0.4}O_3$

In order to estimate the contribution of LSGM electrolyte to the cell performance, the power generation property of the cell using both H_2 and C_3H_8 fuel was also measured by using the

conventional YSZ electrolyte. Similar cell configuration and electrolyte thickness was used for the cell using YSZ electrolyte. Figure 2.13 shows the comparison of anodic impedance plots of the 40 mol% Al-doped LSM55 for anode of LSGM or the conventional YSZ cell using H_2 fuel. While LSGM has superior ionic conductivity especially at lower temperature compared to YSZ,[23] LSGM can also be used as electrolyte for high temperature SOFC. As shown in Fig. 2.13, the anodic overpotential of LSMA64 on YSZ electrolyte is similar with that on LSGM cell at 1273 K. This suggests that similar anodic activity is achieved when using YSZ electrolyte. It is also noted that much larger IR loss was observed for YSZ cell comparing with that of LSGM cell resulting in 1.8 times larger power density on LSGM than that on YSZ. This is reasonable because anodic activity should not be strongly affected by electrolyte.

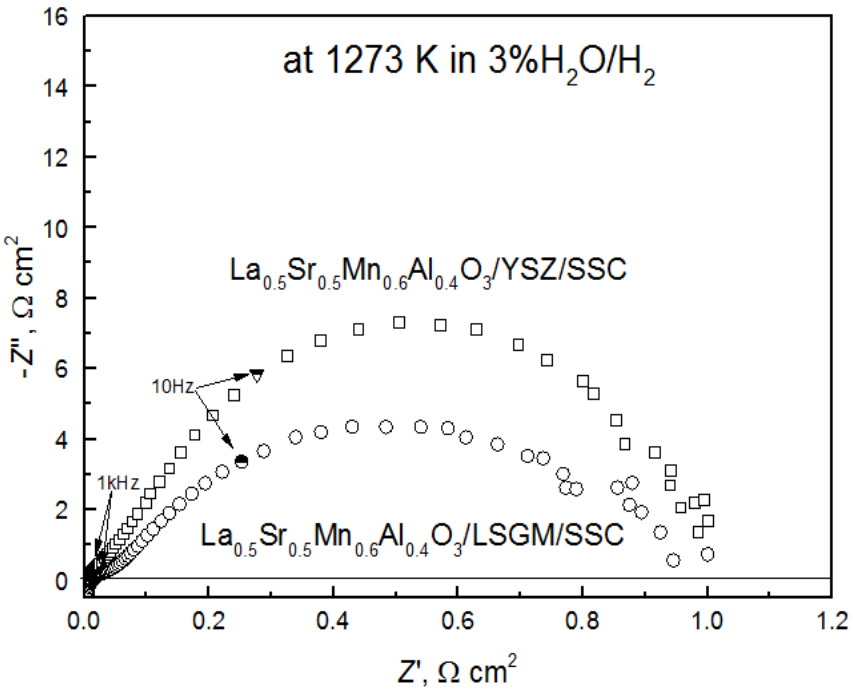

Figure 2.13 Impedance plots of $La_{0.5}Sr_{0.5}Mn_{0.6}Al_{0.4}O_3$ anode on YSZ and LSGM cell when H_2-3%H_2O was used as fuel.

In contrast, interestingly, when the fuel is switched to C_3H_8 at 1173 K (Figure 2.14 (a)), the maximum power density of the cell using YSZ electrolyte is significantly smaller compared to the cell using LSGM electrolyte. As shown in Figure 2.14 (b), small MPD of the cell using YSZ electrolyte in C_3H_8 is assigned to the large IR loss and anodic overpotential. Large activation overpotential is shown by the impedance spectra at 1 kHz suggesting lower activity of the anode. Additionally, anodic impedance at lower frequency suggests that large diffusion resistance was observed for LSMA64 on the cell using YSZ electrolyte. This may be explained by the coke formation on LSMA64 when YSZ is used for anode. This is because the oxygen pumping current is small on the YSZ cell resulting in more coke deposition on anode when C_3H_8 is used for fuel. It is considered that the deposited coke blocked the active sites on LSMA64 also blocked the gas diffusion route in anode. The observation suggests that the superior oxide conductivity of LSGM might have assisted for preventing carbon formation by larger oxygen pumping current. As has been shown by the SEM result in Fig. 2.11, the carbon was hardly formed on Al-doped LSM and therefore, this study revealed that Al doped LSM55 is highly active and suitable as anode for direct C_3H_8 used SOFC.

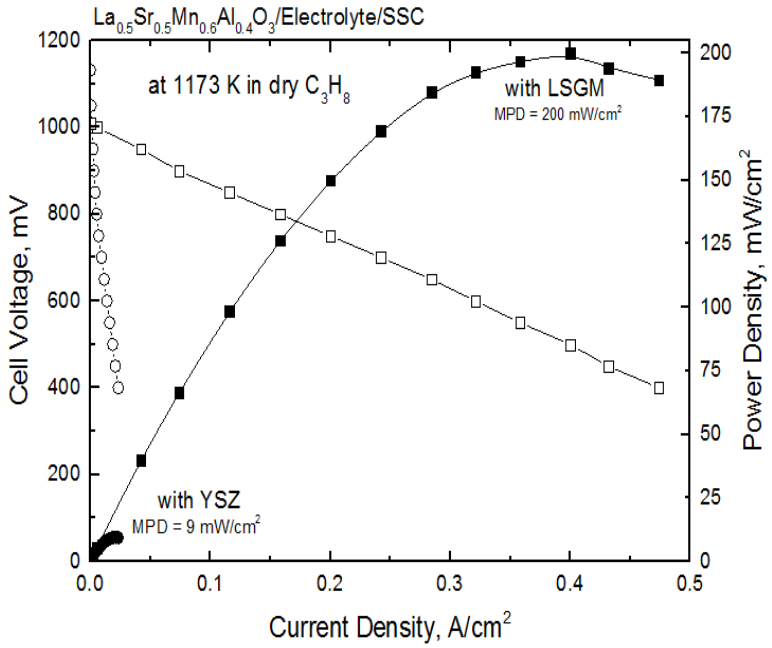

(a)

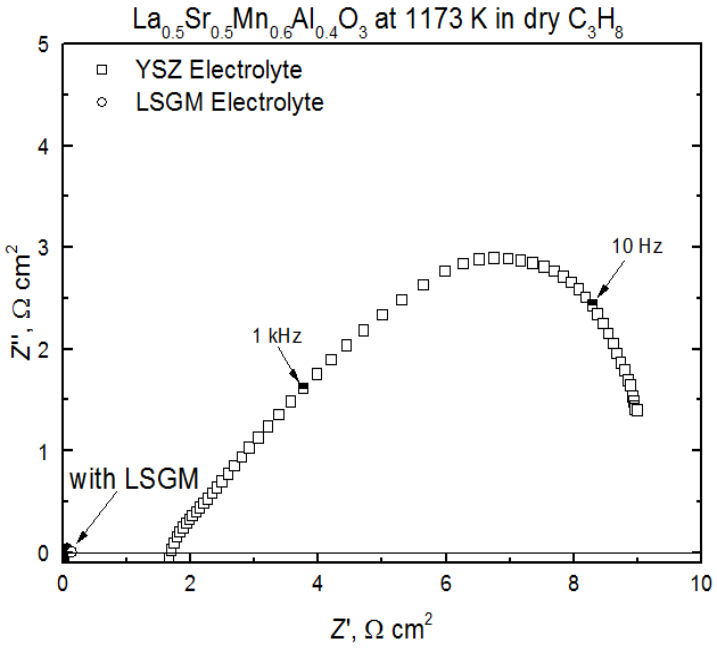

(b)

Figure 2.14 (a) *I-V*, *I-P* curve of the cell using YSZ and LSGM for electrolyte and $La_{0.5}Sr_{0.5}Mn_{0.6}Al_{0.4}O_3$ for anode when using dry C_3H_8 for fuel (b) Anodic impedance plots of $La_{0.5}Sr_{0.5}Mn_{0.6}Al_{0.4}O_3$ anode on YSZ and LSGM cell when dry C_3H_8 was used for fuel.

2.4 Conclusion

$La_{0.5}Sr_{0.5}MnO_3$ perovskite oxide was studied as oxide anode for direct hydrocarbon type SOFC. Reasonably high activity of LSM55 towards H_2 oxidation was observed and the power density of up to 1 W/cm^2 and open circuit voltage (1.1 V) at 1273 K can be achieved when using a cell with LSGM electrolyte that utilizes H_2 fuel. However, the power density using LSM55 significantly decreased when C_3H_8 is used for fuel and this could be explained by the low stability of LSM55 in reducing atmosphere that thermodynamically favor low catalytic activity phases like La_2MnO_4 and Sr_2MnO_4. It was found that stability of $LaMnO_3$ perovskite phase which is the active phase for fuel oxidation was increased by partial substitution of Mn with Al which is a stable trivalent ion. As a result, the substitution of Mn with Al the increased the maximum power density.

In particular, $La_{0.6}Sr_{0.4}Mn_{0.6}Al_{0.4}O_3$ shows high activity to electrochemical oxidation of C_3H_8 resulting in the increased power density of 200 mW/cm^2 which is almost 3 times of non-doped LSM55 anode. In spite of low activity of Al^{3+} to oxidation, this could be assigned to the increased stability of LSM55 due to increased surface activity to C_3H_8 oxidation and decreased IR loss in dry C_3H_8. This may suggests that the perovskite phase of $LaMnO_3$ is of higher catalytic activity to C_3H_8 oxidation than that of La_2MnO_4 and also of higher electrical conductivity. Small particle size of LSM55 was also sustained by doping with Al and so doping Al for Mn site of $La_{0.5}Sr_{0.5}MnO_3$ is positively worked for decreasing the anodic overpotential. In this study, it has also been demonstrated that while LSGM electrolyte is used which is now considered for low temperature SOFC, however, when $Zr_{0.84}Y_{0.16}O_2$ (YSZ) was used for electrolyte, anodic impedance arc of $La_{0.5}Sr_{0.5}Mn_{0.9}Al_{0.1}O_3$ anode was almost the same with that of LSGM electrolyte in case of H_2 fuel. It is also noted that power density of YSZ cell

is much smaller than that of the LSGM cell because of large IR loss. Therefore, $La_{0.5}Sr_{0.5}Mn_{0.6}Al_{0.4}O_3$ is promising as oxide anode for direct hydrocarbon type SOFC.

Reference

(1) Y. Zhao, C. Xia, L. Jia, Z. Wang, H. Li, J. Yu, Y. Li, Int. J. Hydrogen Energ. **38**(36), 16498 (2013).

(2) S.P. Shaikh, A. Muchtar, M.R. Somalu, Renew. Sust. Energ. Rev. **51**, 1 (2015).

(3) X. Ge, S. Chan, Q. Liu, Q. Sun, Advanced Energy Materials **2**(10), 1156 (2012).

(4) J.C. Ruiz-Morales, D. Marrero-López, M. Gálvez-Sánchez, J. Canales-Vázquez, C. Savaniu, S.N. Savvin, Energ. Environ. Sci. **3**(11), 1670 (2010).

(5) T.H. Shin, S. Ida, T. Ishihara, J. Am. Chem. Soc. **133**(48), 19399 (2011).

(6) J. Millichamp, T.J. Mason, N.P. Brandon, R.J. Brown, R.C. Maher, G. Manos, T. Neville, D.J. Brett, J. Power Sources **235**, 14 (2013).

(7) S. Tao, J.T. Irvine, Nat. Mater. **2**(5), 320 (2003).

(8) Y. Huang, R.I. Dass, J.C. Denyszyn, J.B. Goodenough. J. Electrochem. Soc. **153**(7), A1266 (2006).

(9) R. Gorte, H. Kim, J. Vohs, J. Power Sources **106**(1-2), 10 (2002).

(10) T. Kim, G. Liu, M. Boaro, S. Lee, J. Vohs, R. Gorte, O.H. Al-Madhi, B. Dabbousi, J. Power Sources **155**(2), 231 (2006).

(11) M. Mogensen, K. Kammer, Annu. Rev. Mater. Res. **33**, 321 (2003).

(12) R. Gorte, J. Catal. **216**(1-2), 477 (2003).

(13) T. Ishihara, S. Fukui, M. Enoki, H. Matsumoto, J. Electrochem. Soc. **153**(11), A2085 (2006).

(14) S.M. Bukhari, J.B. Giorgi, J. Power Sources **198**, 51 (2012).

(15) S.P. Jiang, J. Mater. Sci. **43**(21), 6799 (2008).

(16) A. Hammouche, Solid State Ionics **28-30**(2), 1205 (1988).

(17) M.A. Daroukh. Solid State Ionics **158**(1-2), 141 (2003).

(18) J. Mizusaki, Solid State Ionics **129**(1-4), 163 (2000).

(19) T. Ishihara, in Perovskite Oxide for Solid Oxide Fuel Cell: Fuel Cells and Hydrogen Energy, T. Ishihara, Editor, p. 14, Springer, New York (2009).

(20) R.D. Shannon, Acta Crystallogr. **A32**, 751 (1976).

(21) H. He, J.M. Vohs, R.J. Gorte, J. Power Sources **144**, 135 (2005).

(22) Q.X. Fu, F. Tietz, P. Lersch, D. Stover, Solid State Ionics **177**(11-12), 1059 (2006).

(23) T. Ishihara, H. Matsuda, Y. Takita, J. Am. Chem. Soc. **116**, 3801 (1994).

Chapter 3

Effects of Cobalt Dopant for $La_{0.5}Sr_{0.5}Mn_{0.9}Al_{0.1}O_3$ on Anodic Property of Direct Hydrocarbon SOFC

3.1 Introduction

In Chapter 2, we have demonstrated that the stability of $LaMnO_3$ perovskite phase can be increased by partial substitution of Mn with stable trivalent Al^{3+} ion (LSMA). Among the examined composition, it was found that $La_{0.5}Sr_{0.5}Mn_{0.6}Al_{0.4}O_3$ (LSMA64) shows the largest power density of 0.2 W/cm^2 and almost theoretical open circuit potential against dry C_3H_8 fuel oxidation at 1173 K. However, the activity to C_3H_8 seems to be still not high enough and this could be assigned to the low catalytic activity of Al. Therefore, in this chapter, effects of Co doping for Mn site with Al was further studied because CoO or Co_3O_4 are well-known as active catalyst to hydrocarbon oxidation.[(1)] In addition, $La_{0.5}Sr_{0.5}Mn_{0.9}Co_{0.1}O_3$ shows reasonable anodic performance in our previous study in both fuel gases condition, albeit stability of LSM55 was much decreased. Therefore, it is expected that double doping of Al and Co to Mn site is effective to increasing stability of perovskite phase in reducing atmosphere and increasing activity of C_3H_8 oxidation. In this chapter, co-doping Al and Co for Mn site was further investigated to achieve better performance in both H_2 and C_3H_8 fuel.

3.2. Experimental

3.2.1. Sample preparation and characterization

Perovskite oxides of $La_{0.5}Sr_{0.5}Mn_{0.9-x}Al_{0.1}Co_xO_3$ (x = 0 - 0.4) (LSMAC) were synthesized by using sol-gel combustion method of $La(NO_3)_3.6H_2O$ (99.9% Wako Pure Chemical Co. Ltd., Japan), $SrNO_3$ (98% Chameleon Reagent, Japan), $Mn(NO_3)_2.6H_2O$ (99.9% Wako Pure Chemical Co. Ltd., Japan), $Al(NO_3)_3.9H_2O$ (98% Wako Pure Chemical Co. Ltd., Japan) and $Co(NO_3)_2.6H_2O$ (98% Wako Pure Chemical Co. Ltd., Japan) similar to the method as in Chapter 2. Citric acid was employed as the complexing agent. All metal nitrates were mixed and dissolved in deionized water by continuous

stirring condition before quantitative amount of citric acid was added. The solution was then heated at 423 K and continuously stirred on a hotplate until the solution converted to viscous gel. The gel was then ignited to flame and resulted in an ash-like precursor. The ash collected from the reaction was calcined at 673 K to remove nitrates residue prior to final calcination at 1523 K. $LaGaO_3$-based oxide, $La_{0.9}Sr_{0.1}Ga_{0.8}Mg_{0.2}O_3$ (LSGM) electrolyte and $Sr_{0.5}Sm_{0.5}CoO_3$ (SSC) cathode were prepared by conventional solid-state reaction method. For the preparation of LSGM, commercial oxides of La_2O_3 (99.9% Kishida Chemical Co., Japan), Ga_2O_3 (99.9% Mitsubishi Materials Corporation, Japan), MgO (99.9% Wako Pure Chemical Co. Ltd., Japan), and $SrCO_3$ (99.9% Kishida Chemical Co., Japan) were mixed in alumina mortar and the obtained powder mixture was pre-calcined at 1273 K for 6 h, pelletized before fired at 1773 K for 6 h. Meanwhile, $Sr_{0.5}Sm_{0.5}CoO_3$ was prepared by continuous heating and stirring of $Sr(CH_3COO)_2.0.5H_2O$ (99% Wako Pure Chemical Co. Ltd., Japan), Sm_2O_3 (99.9% Nacalai Tesque Inc., Japan) and $Co(NO_3)_2.6H_2O$ (98% Wako Pure Chemical Co. Ltd., Japan) dissolved in deionized water. After pre-calcination at 673 K, the powder was fired at 1273 K in air.

Phase confirmation of all obtained powder samples were analyzed by using commercial X-ray diffractometer, XRD (Rigaku, RINT2500) with Cu K_α line. The lattice parameter of LSMAC was refined by employing Rietveld refinement technique using PDXL 2 program (Rigaku Corp). The morphology of the as-prepared powders were investigated by using scanning electron microscope (SEM) (VE-7800, Keyence Co.). Electrical conductivity measurement was conducted by the conventional dc four probe method. Rectangular-shape specimens for the test were prepared by dry pressing powder at 2 MPa before subjected to Cold Isostatic Press (CIP) at 300 MPa for 30 min. The specimens were then sintered at 1523 K for 6 h in air. The densities of the sintered bars were greater than 90% of theoretical value. The electrical conductivity was measured as a function of temperature in air and 1% H_2/Ar gas flow (100 mL/min). For phase stability study of LSMAC, reducing treatment

was conducted for LSMAC powder at x = 0.2 under two different atmosphere in 3%H_2O-H_2 at 1273 K or dry C_3H_8 at 1173 K with a flow rate of 100 mL/min for 1 h.

3.2.2 Single cell preparation and measurement of anodic performance

The electrolyte-supported single cell using LSGM (ca. 0.285 mm thickness) was prepared by screen printing method. The LSMAC anode and SSC cathode was painted on each side of LSGM disc with a diameter of 5 mm. To remove organic solvent, the cell was dried after painting. Platinum mesh (5×5 mm) was pressed on top of the anode as current collector while platinum electrode set close to cathode as a reference electrode by using the commercial Pt paste (Tanaka TR7902). A platinum lead wire was connected to the Pt reference electrode before the cell was fired at 1373 K for 1 h.

The power generating property of the cell was measured with the conventional four-probe method with humidified hydrogen (3%H_2O/H_2) followed by feeding dry C_3H_8 as the fuel. To ensure H_2 gas is completely removed, N_2 gas is purged for 40 min before dry C_3H_8 is introduced. Commercial O_2 was fed to the air side. All gases supplied at the flow rate of 100 mL/min. For measurement of terminal voltage, digital multimeter (Advantest, type R 6451A) was used with constant dc current applied by using galvanostat (Hokuto Denko HA-151A). Current interruption method was conducted to estimate the internal resistance with dc current pulse generated by using current pulse generator (Nikko Keisoku, NCPG 10-1). To record the potential response, digital memory recorder (Hioki 8835) was used. The electrode resistance was also evaluated by the impedance measurement using the impedance/gain-phase analyzer (Solartron type 1255B, Solartron) with the electrochemical interface (Solartron type 1287, Solartron). Phase stability of the cell after the power generation test was conducted *ex-situ* by XRD immediately after the measurement was finished. To analyse carbon deposition on the anode

material after the cell test, commercial spectrometer X-ray photoelectron spectroscopy (XPS) with Al-K_α radiation (Kratos, AXIS-165), SEM with EDS and Raman spectroscopy (Horiba HR800) were employed.

3.3. Results and Discussion

3.3.1 Effects of doping Co on electrical conductivity and phase stability of $La_{0.5}Sr_{0.5}Mn_{0.9-x}Al_{0.1}Co_xO_3$

Figure 3.1 shows the effect of Co doping on the XRD pattern of $La_{0.5}Sr_{0.5}Mn_{0.9-x}Al_{0.1}Co_xO_3$ (x = 0 – 0.4) (LSMAC). The XRD pattern of LSM55 is also shown in this figure as reference. From Fig. 3.1 (a), all diffraction peaks were assigned to Sr-doped $LaMnO_3$ indicating solid solution of the doped Co. Considering that there is no confirmed XRD peaks from secondary phase up to x = 0.4, it seems that Co partially substitutes the lattice in wide concentration. In Fig. 3.1 (b), main diffraction peaks were shown and it was seen that diffraction angle was increased with increasing Co amount up to x = 0.2. The X-ray diffraction peak shift suggests a reduction in lattice parameter up to x = 0.2 prior to slight increase with x = 0.3. LSM55 is known to have a mixed $Mn^{3+/4+}$ with a formal oxidation state of +3.5,[(2)] however the substitution of Al^{3+} and $Co^{3+/4+}$ for LSMAC may also change the oxidation state of Mn. The ionic radii of Co^{3+}/Co^{4+} are 0.0545 nm and 0.0530 nm respectively which is smaller or similar to Mn^{3+} (0.0645 nm) and Mn^{4+} (0.0530 nm).[(3)] Since there is no obvious secondary phase observed, it is safe to presume that Co successfully substituted at the B-site rather than at the A-site. It can be assumed that initially at lower Co doping ($x \leq 0.2$), a larger ratio of Mn^{3+} to Mn^{4+} is available, which explains reduced lattice parameter by the substitution of smaller $Co^{3+/4+}$ ionic radii compared to Mn^{3+}.

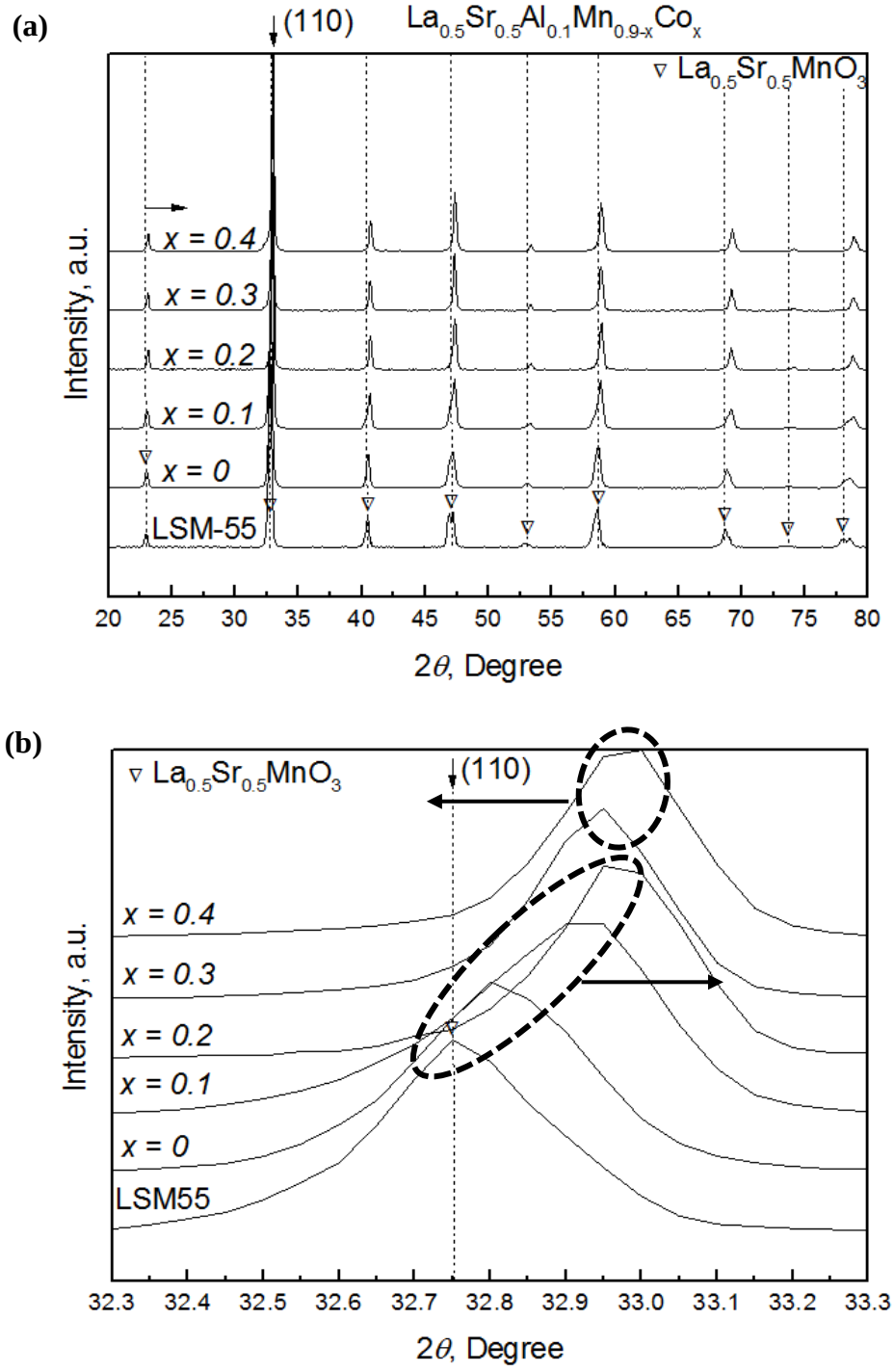

Figure 3.1 (a) XRD patterns of $La_{0.5}Sr_{0.5}Mn_{0.9-x}Al_{0.1}Co_xO_3$ (x = 0 - 0.4) (b) Magnified at main peak (110). XRD pattern of LSM55 is shown as reference

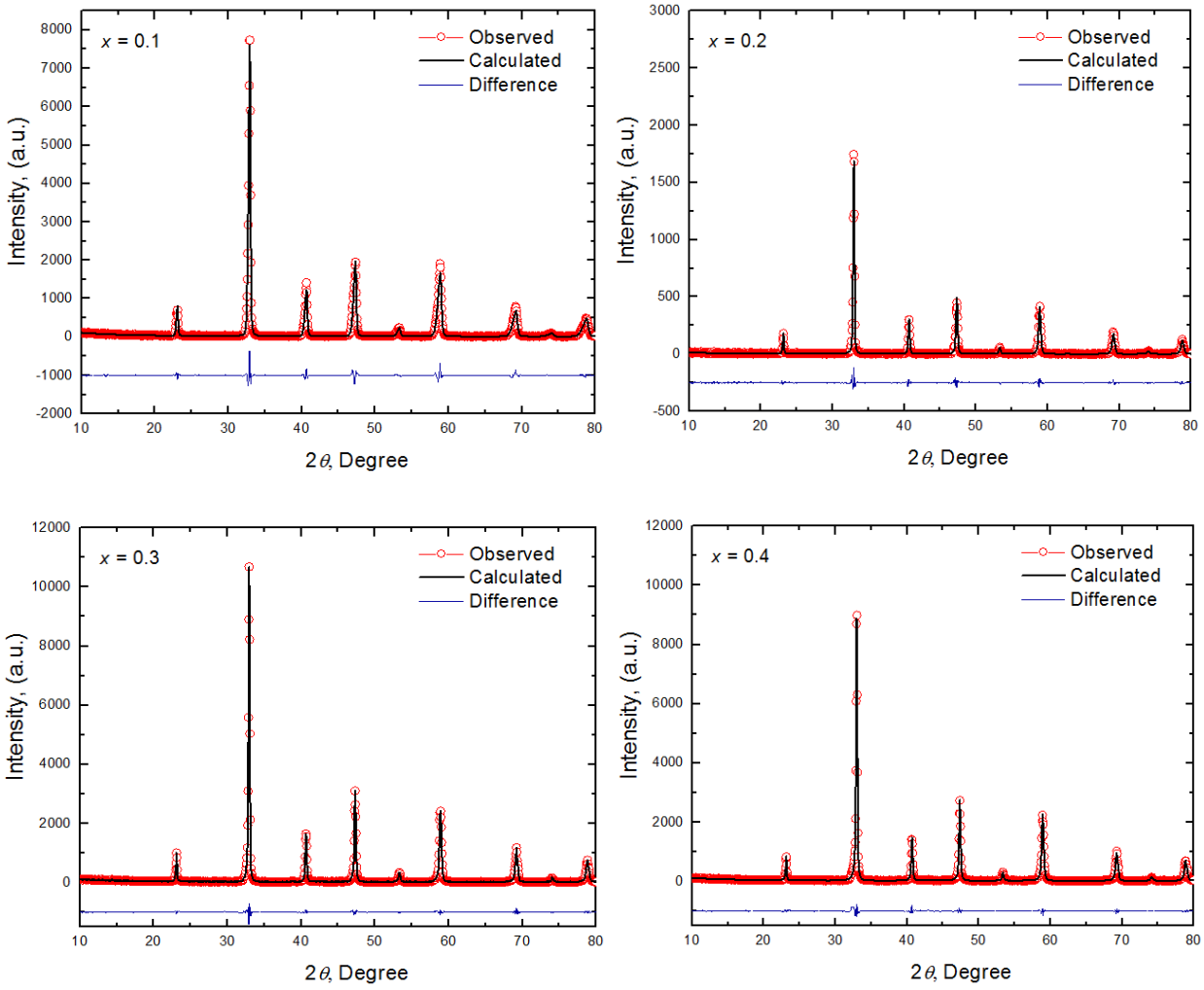

Fig. 3.2 Rietveld refinement of $La_{0.5}Sr_{0.5}Mn_{0.9-x}Al_{0.1}Co_xO_3$ (x = 0 - 0.4)

To analyze Co substitution effects, Rietveld refinement analysis is employed for all LSMAC compositions as shown in Figure 3.2. The dots indicate the experimental data while the continuous line overlapping them is the calculated data. The lowest blue curve shows the difference between experimental and calculated patterns. Figure 3.3 represents the variation of lattice parameter *a* and *c* as a function of Co content, *x* deduced from the Rietveld refinement analysis. The refinement for LSMAC at $x = 0$ reveals *I4/mcm* space group of tetragonal symmetry which is similar to that of LSM55 itself,[4, 5] suggesting little changes to the crystal structure at 10 mol% Al doping. However, the

LSMAC crystallographic transition from tetragonal to trigonal was the most reasonably fit from x = 0.1 resulting in significant increase in lattice parameter c. At x = 0.1 to 0.4, LSMAC can be indexed to $R\bar{3}c$:H space group (trigonal symmetry). The changes in lattice parameter a are in accordance to the shift by XRD peaks of (110) plane within the error bar limit, with lattice parameter a reduced from x = 0 until x = 0.2 before a slight increase at x = 0.3. The calculated structural parameter is also summarized in Table 3.1. The lattice parameter was slightly decreased with increasing Co amount suggesting that Co successfully substitutes the lattice position of Mn site of LSMA.

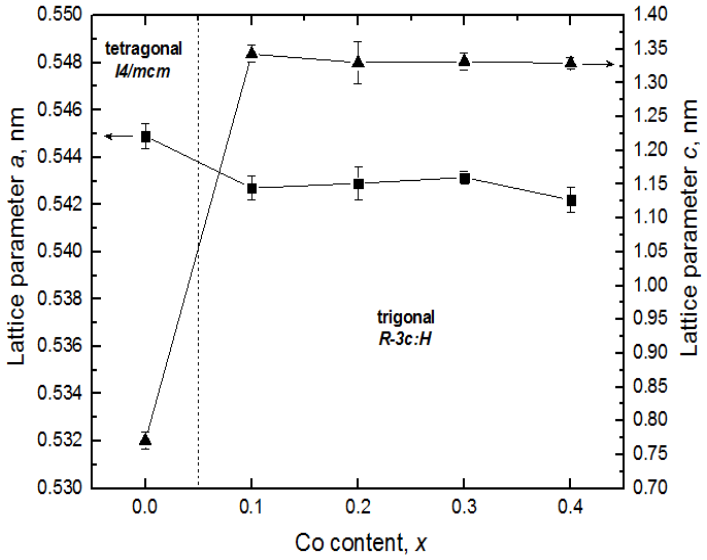

Figure 3.3 Lattice parameter *a* and *c* as a function of nominal Co content, *x*

Table 3.1 Room temperature structural parameters (Rietveld refinement) for $La_{0.5}Sr_{0.5}Mn_{0.9-x}Al_{0.1}Co_xO_3$ specimen: tetragonal phase *I4/mcm* for x = 0 and trigonal $R\bar{3}c$:H phase for x = 0.1-0.4.

	x				
Space group	0	0.1	0.2	0.3	0.4
	I4/mcm	$R\bar{3}c$:H			
Cell					
a (nm)	0.5449	0.5427	0.5429	0.54315	0.5422
c (nm)	0.771	1.343	1.33	1.332	1.3291

The morphology of the as-prepared LSMAC powders investigated by SEM are shown in Figure 3.4. The images reveal very fine powder particles possibly in nanometer scale as expected from sol-gel combustion route. While the LSMAC powders retained fine sizes even after final calcination yet the particles are heavily agglomerated into larger grains. It is known that carbon deposition rate on anode may be reduced by altering the micromorphological characteristics of anode and the use of sol-gel combustion method is hoped to assist in reduced coking.[6] Nevertheless, the agglomeration makes the determination of particle size particularly difficult but it is estimated from the micrograph that the clusters size are broadly distributed from less than 1 to 3 μm.

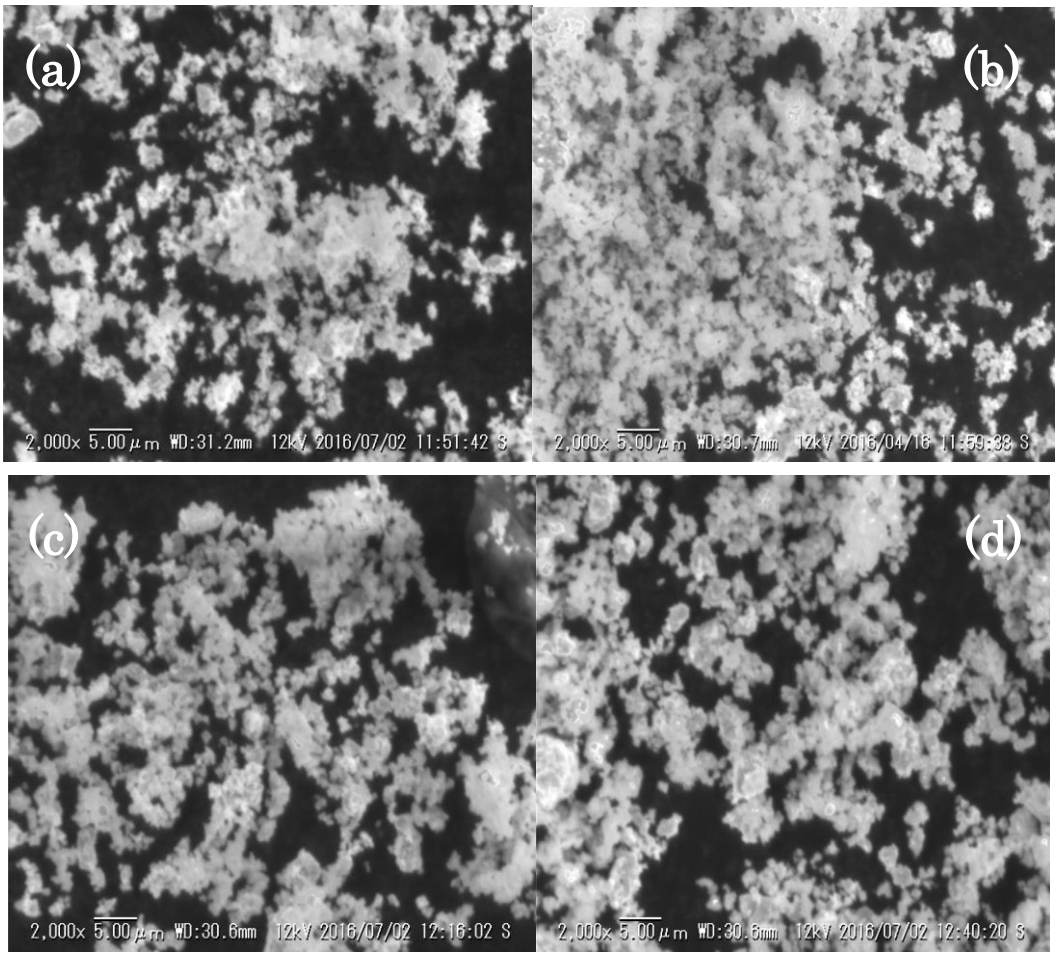

Figure 3.4 Powder morphology of as-prepared $La_{0.5}Sr_{0.5}Mn_{0.9-x}Al_{0.1}Co_xO_3$ (a) x = 0.1 (b) x = 0.2 (c) x = 0.3 and (d) x = 0.4

Figure 3.5 shows the electrical conductivity of LSM55 and LSMAC oxides in air as well as in 1% H_2-99% Ar mixture. As expected, LSM55 exhibits exceptionally high hole conductivity in air attributed to the oxidation of Mn^{3+} to Mn^{4+} ions as an electronic compensation to the lower valence of Sr^{2+}.[7] The formation of hole in LSM55 is expressed by the following equation,

$$\frac{1}{2}O_2 \leftrightarrow O_i'' + 2h^{\cdot} \quad (1)$$

The electrical conductivity of the doped $LaMnO_3$ displays three separate stages depending on the dopant type and composition as shown in Figure 3.5. In air atmosphere (Fig. 3.5 (a)), firstly when doped with Al, the electrical conductivity of LSM55 is decreased due to reduced polaron hopping sites. The substitution of Mn by Al has been reported to cut the Mn-O-Mn bond in LSM55, leading to decrease in mobility of hole.[7, 8] Further decreased is exhibited when LSMA is doped with Co due to further reduction of Mn-O-Mn chain. In addition, while temperature dependence of LSM55 conductivity shows metallic behaviour, it changes to semiconductor-like one by doping Co at $x > 0.1$. Finally, although the electrical conductivity of LSM55 and LSMA initially decreased with Co dopant, it slightly increased with increasing Co amount. This suggests that while hole concentration is decreased by doping Co, the electrical conductivity gradually increased by the increase in hole mobility owing to the existence of similar Co^{3+}/Co^{4+} mixed valence state like Mn^{3+}/Mn^{4+}. Since the electrical conductivity of LSM55 is predominantly p-type, as expected the electrical conductivity decreased in 1% H_2-Ar atmosphere (Figure 3.5 (b)). Additionally, in low P_{O2} condition, higher concentration of divalent manganese ions, Mn^{2+} will be formed. The increase in ionic radius of Mn^{2+} compared to Mn^{3+}/Mn^{4+} causes longer Mn-O-Mn bond distance, resulting in increased hopping energy.[8] In a similar manner in air, doping Al decreased the electrical conductivity and further co-doping with Co also decreased the conductivity, however, it gradually increased with increasing Co amount. By doping

stable trivalent Al^{3+}, chemical equilibrium shifts to the left side producing decreased amount of hole. It is widely known that Co^{2+} is stable over wide P_{O2} range and so doping Co^{2+} also shifts equilibrium to the left, further lowering the electrical conductivity.

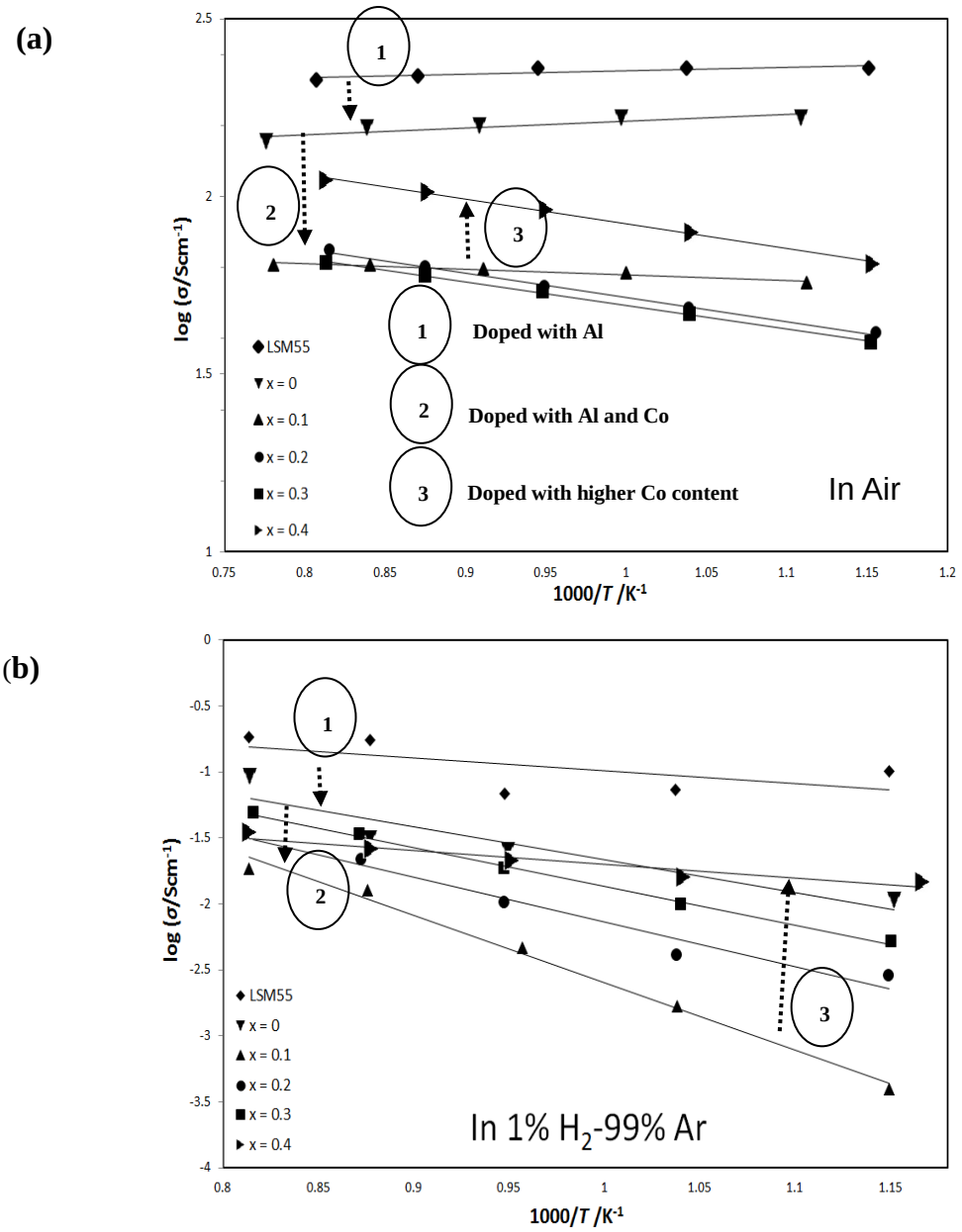

Figure 3.5 Temperature dependence of electrical conductivity of LSM55 and LSMAC in (a) air and (b) 1% H_2/Ar

The fact that LSM55 decomposed under reducing atmosphere greatly affects the electrical conductivity of LSMAC. However, the stability of LSM55 in reducing atmosphere has been demonstrated to increase by doping Al for the Mn site owing to the stability of trivalent Al^{3+}.[9] Yet, incorporation of another transition metal like Co may again alter the phase stability of the oxide. Figure 3.6 shows the XRD pattern of Al and Co-doped LSM55 of LSMAC72 (x = 0.2) after reduction in H_2 at 1273 K. While decomposition to La_2MnO_4 and Sr_2MnO_4 is observed, the main phase of LSMAC72 is still dominantly $LaMnO_3$ perovskite. It should be noted in Fig. 3.5 (b) that while the electrical conductivity of LSM55 is decreased with Co doping, temperature dependence of LSMAC's electrical conductivity is prominently more stable than that of LSM55 during the conductivity measurement which can be assigned to improved phase stability by doping Al.

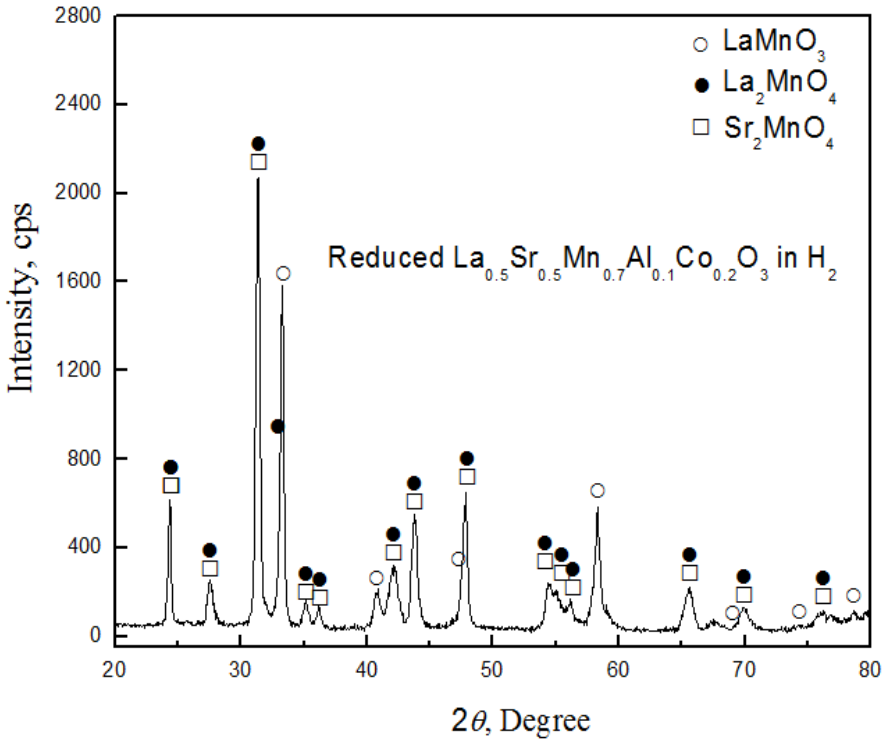

Figure 3.6 XRD pattern of LSMAC72 after reduction treatment in 3%H_2O-H_2 at 1273 K

3.3.2 Effects of Co dopant on anodic performance of LSMA using wet H_2 fuel

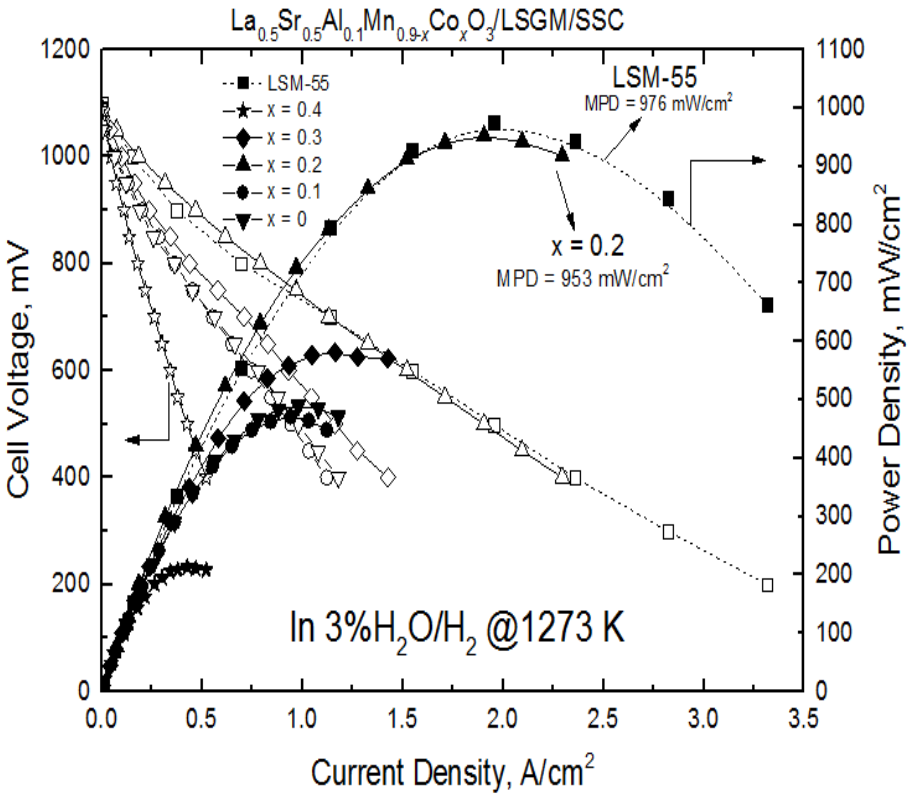

Figure 3.7 I-V/P curve of the $La_{0.5}Sr_{0.5}Mn_{0.9-x}Al_{0.1}Co_xO_3$ (x = 0 to 0.4) compared to LSM55 in H_2 and maximum power density of the cell at 1273 K

Figure 3.7 highlights the power generation curve of the cell using LSMAC oxide anode at 1273 K when 3% H_2O/H_2 was fed for fuel. When LSMA (x = 0) was used, the maximum power density (MPD) was ca. 490 mW/cm^2, which is much smaller than that of the cell using LSM55. This could be explained by the decreased conductivity of LSM55 by doping Al in Mn site. On the other hand, by doping Co, almost theoretical open circuit potential was exhibited and the power density of the cell was much increased and it achieved to ca. 1 W/cm^2 at x = 0.2. Nonetheless, the maximum power density was decreased with increasing Co amount and at x = 0.4, the power density achieved was as small as 200 mW/cm^2 which is 1/5 of the cell using LSM55 for anode. Since it is well-known that Co

oxide is active to fuel oxidation reaction, the initial increased power density with Co doping was assigned to the increased surface activity to electrochemical H_2 oxidation. However, excess amount of Co may deposit on the surface of LSM55 as metallic state resulting in the decreased surface activity to H_2 oxidation. The deposition of Co will be further discussed later. Additionally, since electrical conductivity of LSMAC increases with higher Co content, it is expected that the decreased MPD is mainly related to the decreased phase stability in particular, when excess amount of Co was doped. Hence, the power density was decreased at the excess amount of Co dopant. In any way, the cell using 20 mol% Co doped LSMA (LSMAC72) shows comparable power density to LSM55 when H_2 was used for fuel.

Figure 3.8 shows the comparison of internal resistance of the LSMAC cell as a function of current density. Particularly large IR resistance was observed on LSMA (Fig. 3.8 (a)) but is decreased by doping Co. However, with excess amount of Co, the IR loss is slightly increased again. Consequently, as shown in Fig. 3.5, the electrical conductivity decreased by addition of Co, but the slight increase with increasing Co amount suggests that changes in thermal expansion coefficient may also affect the interface resistance. On the other hand, it is evident that the overpotential dominated the internal resistance and it is much decreased by doping Co at $x = 0.2$ in Fig. 3.8 (b). However, for other compositions, the overpotential hardly changed. Therefore, with the exception of LSMAC72, dependence of power density on Co amount was mainly determined by decreased IR loss. Both IR loss and overpotential reach a minimum at $x = 0.2$ suggesting sufficient surface activity against H_2 oxidation is achieved.

(a)

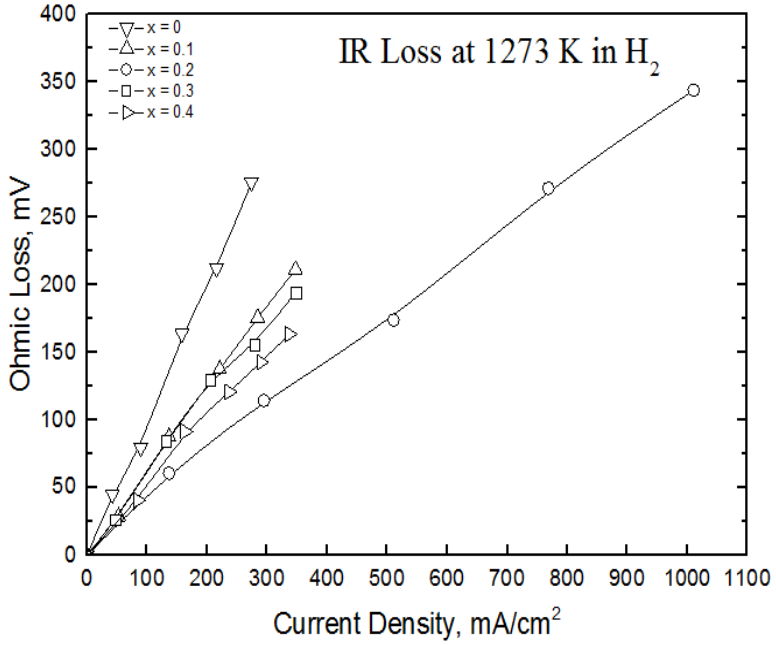

(b)

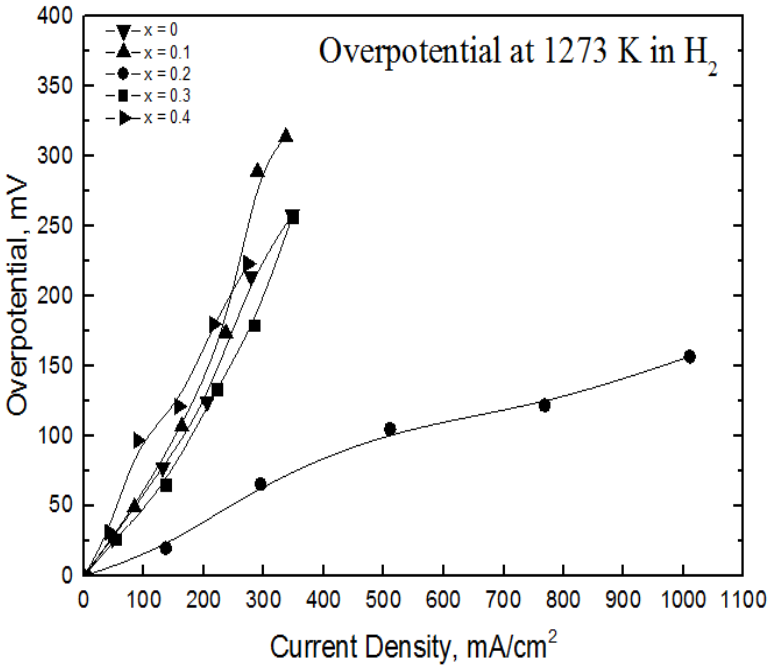

Figure 3.8 Potential drop by (a) IR loss and (b) overpotential of $La_{0.5}Sr_{0.5}Mn_{0.9-x}Al_{0.1}Co_xO_3$ (x = 0.1-0.4) in H_2 at 1273 K

Figure 3.9 shows the comparison of anodic impedance of LSMAC cells when wet H_2 was fed as fuel under open circuit condition. At 10 mol% Co, similar IR loss to non-doped LSMA was observed (0.25 Ω cm^2) and was further shifted to lower value on the real axis intercept at higher frequency with increasing Co doped amount. This observation cannot be assigned to the increased electrical conductivity due to the similar valence state of Mn^{3+}/Mn^{4+} and Co^{3+}/Co^{4+}. In addition, the electrical conductivity of LSMA is actually higher than Co-doped LSMA. Therefore, the decreased IR loss might be explained by the improved contact between anode and the LSGM electrolyte by doping Co. Although IR loss is decreased with further increased in Co amount, the impedance arc was monotonously increased with increasing Co amount suggesting large diffusion overpotential occurred. However, the exception was observed at 20 mol% Co doped, when the cell shows the lowest anodic IR loss and overpotential.

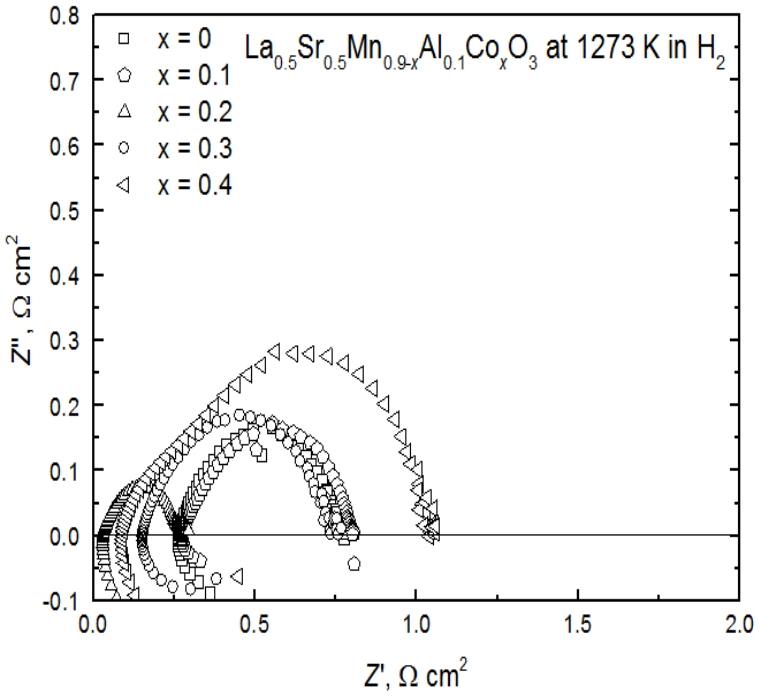

Figure 3.9 Anodic impedance spectra of $La_{0.5}Sr_{0.5}Mn_{0.9-x}Al_{0.1}Co_xO_3$ (x = 0.1-0.4) in H_2 at 1273 K

The internal resistance of the electrode is highly a subject of morphological features of the anode. As can be seen from Fig. 3.10 (a) and (b), particle size of LSMAC72 after preparation was of submicron size yet small particle was sustained after reduction in H_2. Similarly, small particle size as well as higher porosity of LSMAC72 is sustained after the power generation measurement compared to LSMAC63 (Fig. 3.10 (c) and (d)) suggesting aggregation was easily occurred with increasing Co content higher than 20 mol%. The small particle size of LSMAC72 provides larger number of active sites while better porosity improves the gas diffusion and this can be reflected by smaller impedance at low frequency as shown in Fig. 3.9. This suggest the diffusion overpotential of LSMAC72 is mainly assigned to the large gas diffusion and surface adsorption property.

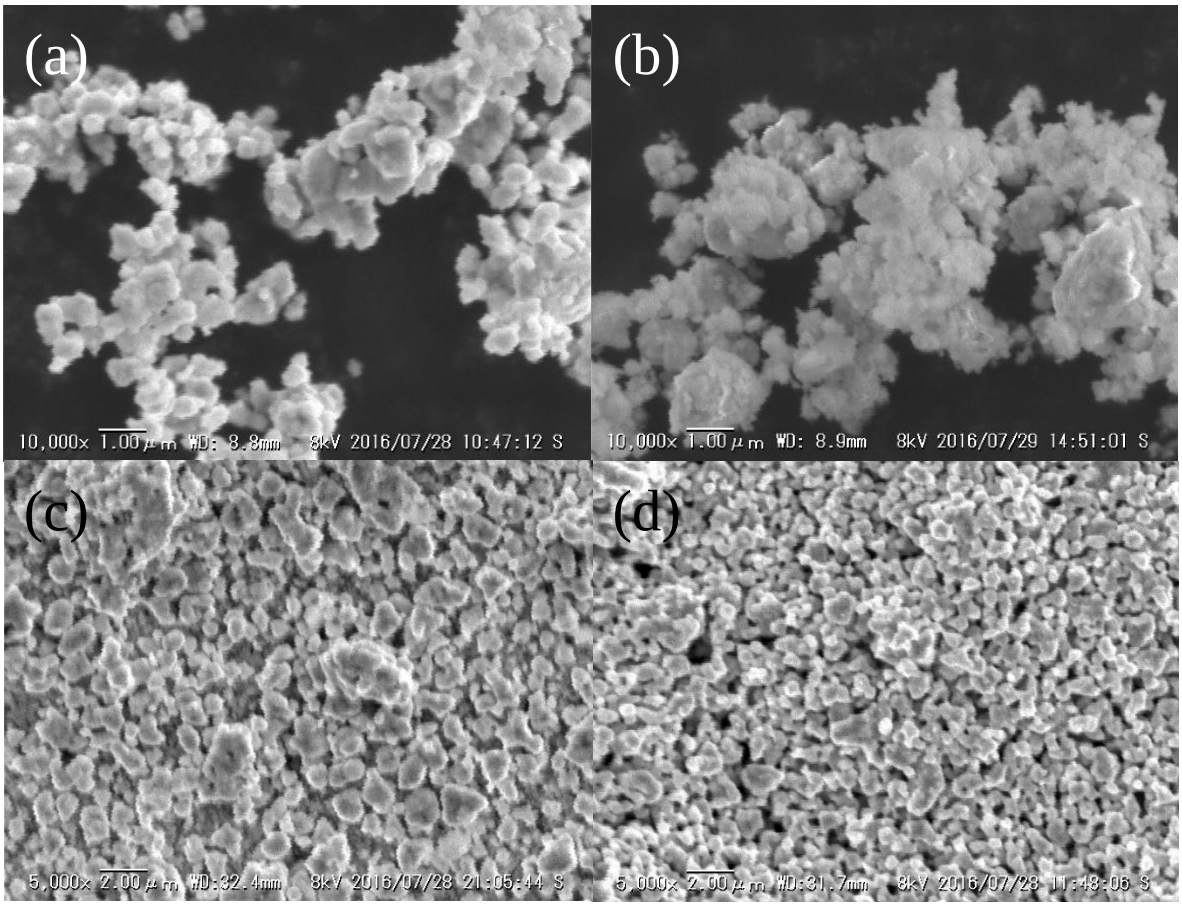

Figure 3.10 SEM images of (a) as-prepared LSMAC72 powder, (b) after H_2 reduction at 1273 K, and the anode surface after the power generation measurement of (c) LSMAC63; (d) LSMAC72

3.3.3. Effects of Co dopant on anodic performance of LSMA using dry C_3H_8 fuel

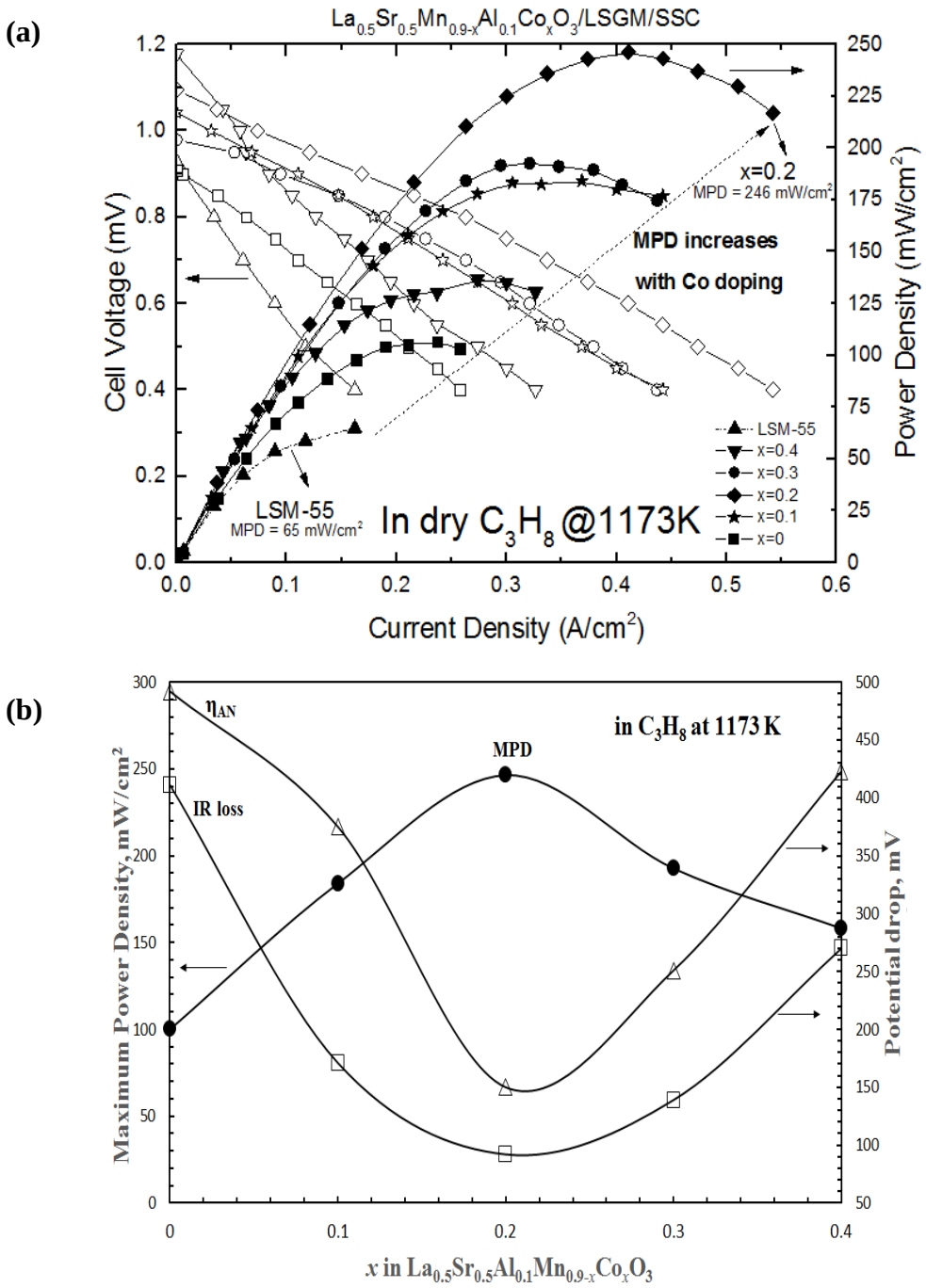

Figure 3.11 (a) I-V/P curve of the $La_{0.5}Sr_{0.5}Mn_{0.9-x}Al_{0.1}Co_xO_3$ (x = 0 to 0.4) compared to LSM55 in dry C_3H_8 and (b) maximum power density of the cell as well as the potential drop by IR and anodic overpotential at 0.3 A/cm^2 in dry C_3H_8 environment as a function of Co amount in $La_{0.5}Sr_{0.5}Mn_{0.9-x}Al_{0.1}Co_x$

Figure 3.11 (a) represents the *I-V*, *I-P* curves of the cell using LSMAC for anode when dry C_3H_8 was fed at 1173 K. Theoretical open circuit voltage (OCV) for direct oxidation of C_3H_8 at 1173 K is 1.12V and LSMAC at x = 0.1, 0.2 and 0.4 show nearly to the theoretical OCV suggesting high activity to C_3H_8 oxidation. However, compared to H_2 oxidation, lower OCV was observed when C_3H_8 is used. Contrary to the performance when using H_2 fuel, MPD is increased with increasing Co dopant and achieved the highest value at x = 0.2 (246 mW/cm^2) which is ca. 2.5 times larger than that of the non-doped LSMA anode. Yet, in a similar manner with H_2 fuel, MPD of the cell decreased when excess amount of Co was doped. Apparently, the decrease in MPD with Co content of x > 0.2 was assigned to the increased overpotential as shown in Fig. 3.11 (b). Therefore, it is considered that the surface activity of LSMA to electrochemical oxidation reaction was decreased at excess amount of Co doped and this is the same dependency with that in the case of H_2.

Figure 3.12 (a) and (b) shows IR loss and overpotential of the cell using LSMAC as a function of current density when C_3H_8 is used for fuel. Dependence of IR loss and overpotential on the amount of Co doped for LSMA is similar with that of the cell using H_2 for fuel (Fig. 3.8). Compared to internal resistance of the cell when using H_2 fuel, large overpotential was observed and the cell at x = 0.2 shows smallest IR loss and overpotential amongst the LSMAC anode examined, a similar dependency to the case of H_2 fuel. Therefore, improved power density at x = 0.2 could be assigned to the decreased anodic overpotential and IR loss. Typically when using hydrocarbon, low IR loss might be assigned to the improved electronic conductivity by carbon deposits.**(10)** However, in this study, filament-like carbon deposition is not observed and so the decreased IR loss by doping Co especially at x = 0.2 is most likely due to increased electrical conductivity. Further discussion on the role of Co species in the enhancement of the cell performance will be presented later.

(a)

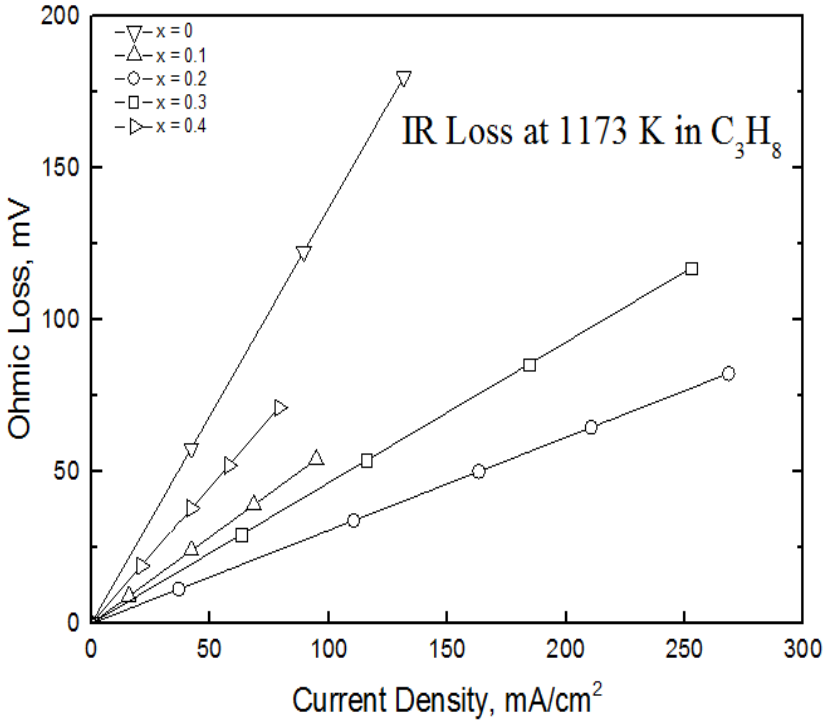

(b)

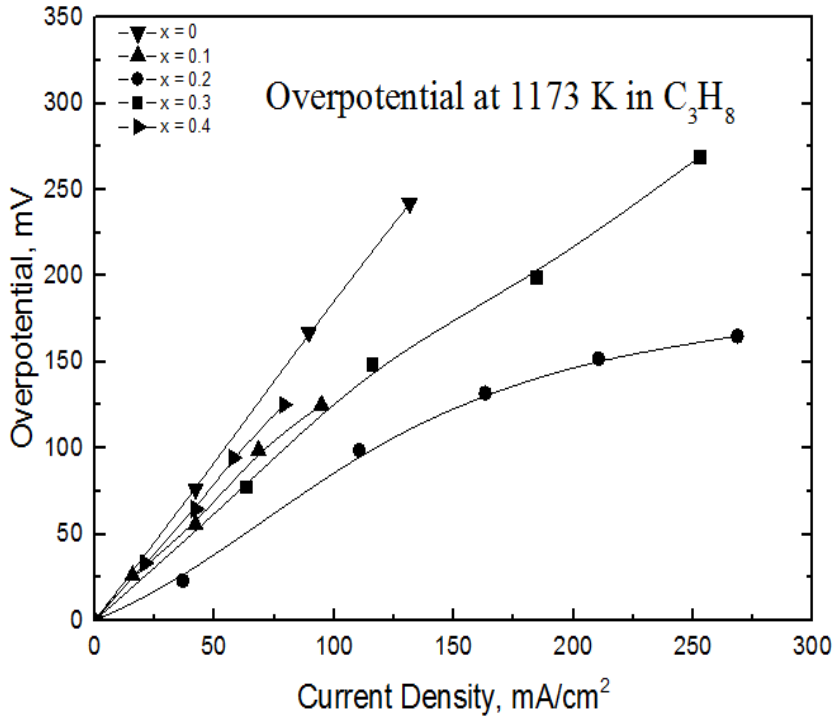

Figure 3.12 Potential drop by (a) IR loss and (b) overpotential of $La_{0.5}Sr_{0.5}Mn_{0.9-x}Al_{0.1}Co_xO_3$ (x = 0.1-0.4) in C_3H_8 at 1173 K

In order to analyze the change in oxidation reaction, a comparison of anodic impedance spectra of Co dopant at x = 0.2 (LSMAC72) when using H_2 and C_3H_8 fuel is shown in Figure 3.13. Slight decrease in IR loss is observed when C_3H_8 is used. However, the anodic impedance arc was clearly larger than that in H_2 fuel. The impedance arc in C_3H_8 consists of at least two arcs and it is seen that impedance arc at lower frequency region (10 Hz) was much larger. This suggests that diffusion polarization is much larger in the case of C_3H_8 compared to H_2. Considering the larger molecular size of C_3H_8, large diffusion resistance is reasonable and this is the main reason for increased anodic overpotential. However, as has been shown previously in Fig. 3.10, the small particle size of LSMAC72 provides larger surface area for gas diffusion resulting in lowest anodic overpotential compared to other LSMAC.

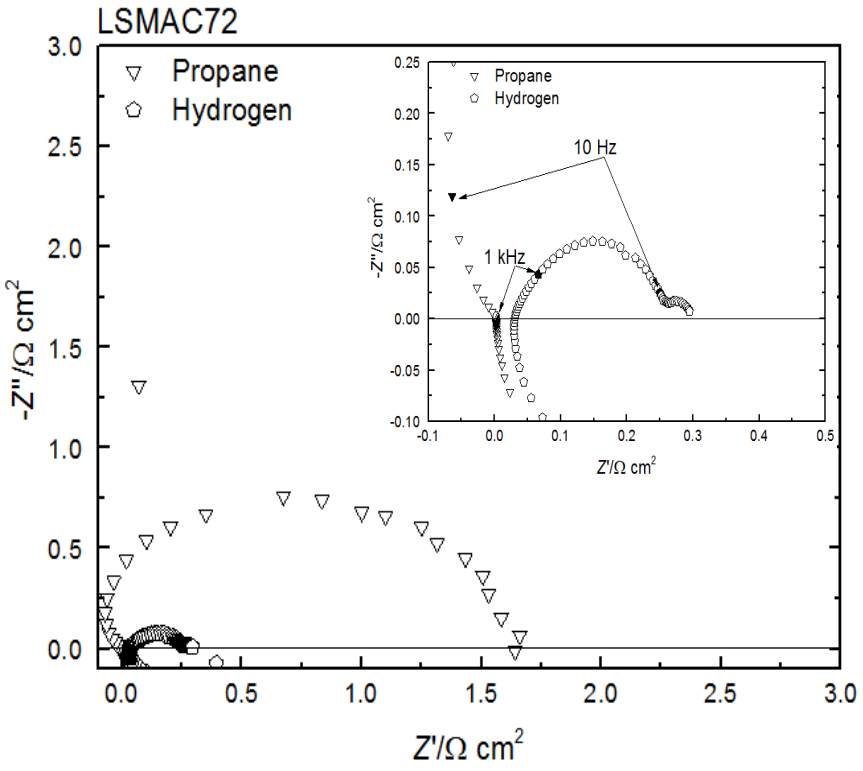

Figure 3.13 Anodic impedance spectra of $La_{0.5}Sr_{0.5}Mn_{0.7}Al_{0.1}Co_{0.2}O_3$ using H_2 and C_3H_8 fuel

3.3.4 Phase stability and coke mitigation of Co-doped LSMA

Al dopant has been demonstrated to improve the phase stability of LSM55 as discussed in detail in Chapter 2. However, unlike Al^{3+}, Co as a transition metal is multivalence, raising fear that the stability of $LaMnO_3$ host can be reduced with further Co doping. To understand the phase decomposition of LSMAC, the XRD pattern for LSMAC anodes after the power generation test in C_3H_8 is shown in Figure 3.14 (a). Similar to LSMA in Chapter 2, XRD peak of $LaMnO_3$ perovskite phase is still strong and the main decomposition phases were determined to be La_2MnO_4 and Sr_2MnO_4. Ishihara et al. reported that the active phase of LSM55 has been assigned to $LaMnO_3$ phase,[(11)] which means the cell performance using LSM55 based anode is strongly associated to the stability of $LaMnO_3$ phase against reduction. While electrical conductivity increased with higher Co content in 1%H_2 atmosphere, phase stability is decreased when Co content is higher than 20 mol%. In other words, there is a strong correlation between electrical conductivity and phase stability in regards to the content of Co dopant. Based on the power generation measurement in both H_2 and C_3H_8, the optimum Co content is found to be around 20 mol%. In order to confirm the deposition of Co, we have previously shown the XRD pattern after reduction in H_2 in Fig. 3.6. From equilibrium, metallic state is the most stable state for Co, and metallic Co may be deposited from lattice position. However, under both condition, similar peaks are observed as shown in Figs. 3.14 (a) and 3.6, in which the main phases were $LaMnO_3$ and $(La, Sr)_2MnO_4$. However, Co metallic peak cannot be detected after treatment in both reducing condition. Therefore, although metallic Co is expected thermodynamically, it is difficult to detect the formation of Co by XRD. This could be assigned to the excessively small Co deposit size. However, under SOFC operating condition, since P_{O2} is not small because of permeated oxygen it is considered that Co may exists at the lattice position in LSMA.

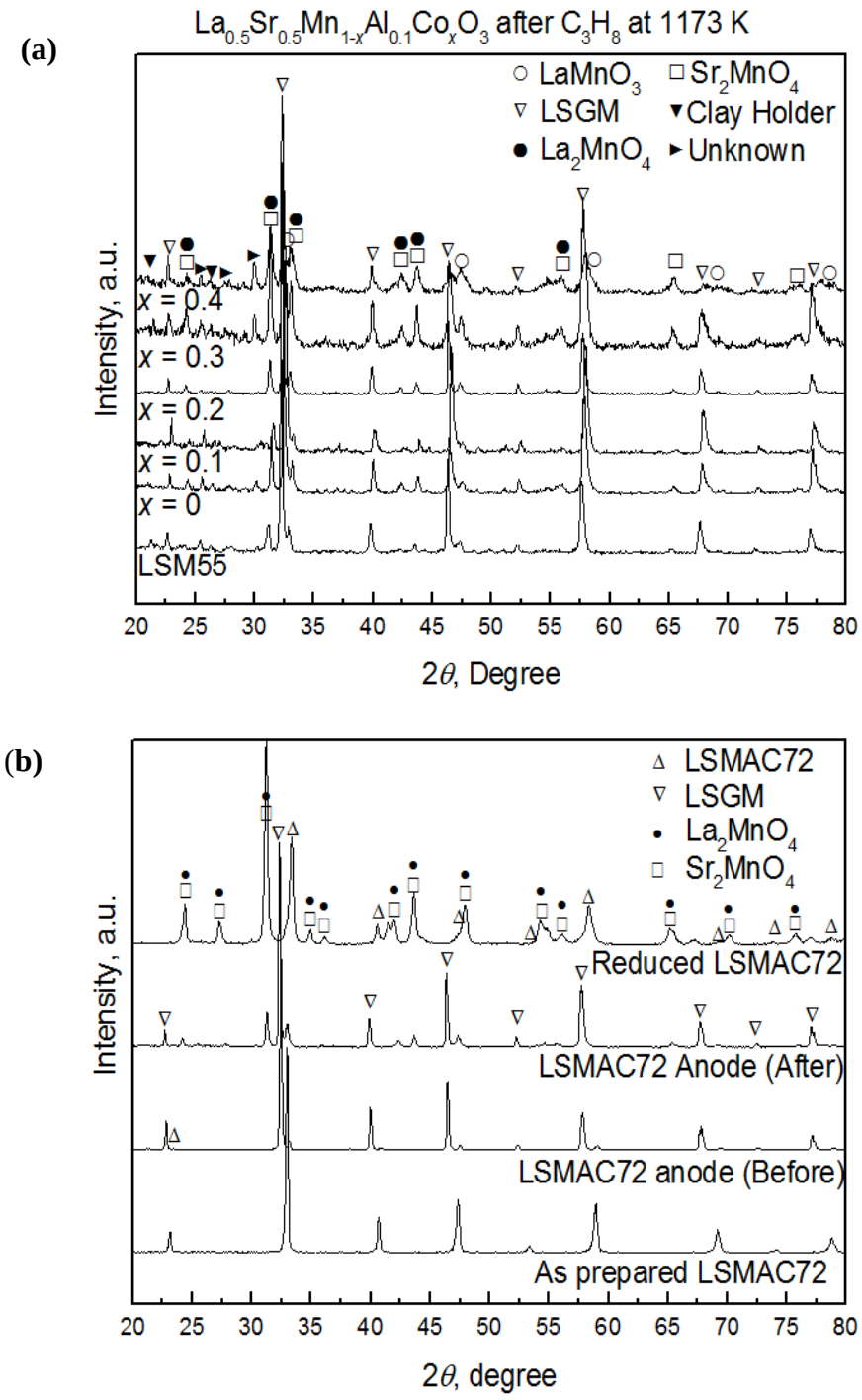

Figure 3.14 XRD patterns after power generation measurement test using C_3H_8 fuel at 1173 K of (a) $La_{0.5}Sr_{0.5}Mn_{0.9-x}Al_{0.1}Co_xO_3$ (b) $La_{0.5}Sr_{0.5}Mn_{0.7}Al_{0.1}Co_{0.2}O_3$ before and after the power generating test

Since LSMAC72 shows high power density compared to other LSMAC anode, a detailed characterization including XRD measurement of LSMAC72 anode before and after power generation measurement at 1173 K in C_3H_8 is shown in Figure 3.14 (b). Additionally, the XRD pattern for as-prepared LSMAC72 and LSMAC72 sample in reducing treatment in dry C_3H_8 at 1173 K for 1 h are also shown in this figure. The diffraction peaks in XRD from LSMAC72 after power generation measurement were related to $LaMnO_3$ perovskite, but strong peaks assigned to La_2MnO_4 were also observed around 33°, suggesting phase separation of $LaMnO_3$ to MnO and La_2MnO_4. It is obvious that the decomposition of LSMAC72 is similar to that of LSM55. However, as shown in Fig. 3.14 (b), doping Al for Mn site is effective for increasing the stability of perovskite phase because the intensity ratio of $LaMnO_3/La_2MnO_4$ main peak was 0.71 which is 2 times larger than that of non-doped LSM55 (peak ratio was 0.36). Therefore, even with doping with Co, it seems that doping Al for Mn site is effective for increasing the stability of perovskite phase against reduction because of stable valence number of Al^{3+}.

Additionally, the long term stability of LSMAC72 anode was conducted at 1173 K. Fig. 3.15 shows terminal potential of the cell using LSMAC72 anode at 0.4A/cm^2 as a function of operating period. Normally, power density was drastically decreased with operation time when metal anode like Ni is used due to coke formation. However, as shown in Fig. 3.15, in the case of LSMAC72 anode, stable terminal potential was sustained over 9 h studied. At the initial period, decrease in power density was observed around 1h, and then the terminal potential became stable around ca. 0.7 V at current density of 0.4 A/cm^2. It can be seen that equilibrium condition was achieved fairly quick within the first hour of C_3H_8 supplied. Although decomposition of LSMAC72 is anticipated, the degradation rate is fairly slow suggesting the $LaMnO_3$ main phase is quite stable. On the other hand, any coke formation on the anode is particularly an important issue when hydrocarbon is used for fuel. The coke formation

will block the active reaction sites, resulting in the deactivation of the anode activity. While tar-like carbon formation is observed as a by-product effluent at 1173 K, filamentous coke formation seems to be prevented on LSMAC72 anode considering the relatively stable voltage output.

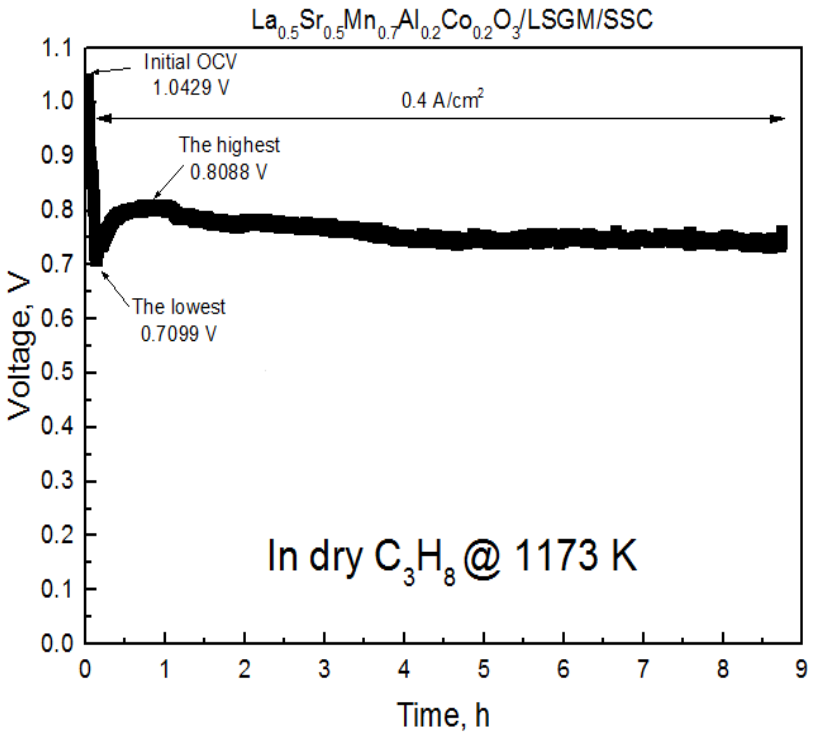

Figure 3.15 Changes in terminal voltage of the cell using $La_{0.5}Sr_{0.5}Mn_{0.7}Al_{0.1}Co_{0.2}O_3$ anode at a current density of 0.4 A/cm^2.

To investigate any existence of coke formation, Raman spectroscopy is used on LSMAC72 anode after the power generation measurement in dry C_3H_8 at 1173 K (Figure 3.16). This technique is an excellent tool to detect the formation of carbon but may also reveals types of ion species present. For instance, the main peak at ca. 700 cm^{-1} for the anode after measurement is related to Mn-O bonding (Mn^{3+}), although the broadening peak at ca. 550 cm^{-1} could be assigned to Mn^{2+} due to its weak asymmetric feature and increased intensity after reduction.[12] Because the main peak at ca. 700 cm^{-1}

became broadened, there is a possibility that it could also be related to Co^{2+} of CoO (675 cm^{-1}) or Co^{3+} as in Co_3O_4 (690 cm^{-1}).[13, 14] Since metal is not Raman active, detection of Co metal is impossible by Raman spectroscopic measurement. While presence of metallic Co is not thoroughly confirmed, the effect of metallic catalysts have been shown to greatly enhanced electrode performance.[15] The fact that LSM55 exhibits respectable performance using H_2 fuel without Co addition confirms that LSM55 itself has somewhat high catalytic activity. However, noticeable enhancement with Co addition is shown when using C_3H_8 fuel as has been discussed earlier. Cho and co-workers have demonstrated that Co alloying with Ni on Ni-$Ce_{0.8}Gd_{0.2}O_{1.9}$ anode enhanced the MPD of the cell when CH_4 is used for fuel.[16] This is most likely due to high activity of Co to direct hydrocarbon oxidation. It was reported that the catalytic activity of Co to oxidation of hydrocarbon fuel is comparable to Ru or Ni under SOFC operational environment.[17] Hu and co-workers have shown that Co^{2+} supported on silica is active for dehydrogenation of C_3H_8 above 823 K and exhibits selectivity for 95% dehydrogenation vs. $C-C$ bond cracking reactions at 923 K.[13] The possible presence of $Co^{2+/3+}$ in LSMAC72 after the reduction hinting at similar catalytic effect in the current study. In addition, incorporation of Co enhances the activity of the triple phase boundary (TPB), resulting in an increased of charge transfer that promptly decreased the polarization resistance.[18] Compared to the resistance when using H_2 fuel, large anodic overpotential is reasonably expected because of complicated oxidation mechanism and more number of electron should be transferred when hydrocarbon fuel is supplied. Clearly, Co dopant achieved sufficient catalytic activity on fuel oxidation and electrical conductivity, in particular, at x = 0.2.

More considerable interest however is for the existence of any peak in the D-band and G-band spectrum in 1200 – 1750 cm^{-1} region of the Raman spectra. G-band is associated to the $C-C$ stretching, common to sp^2-bond formation and usually observed for the peak at 1380 cm^{-1} while D-band features reflect disorder in the structure of the deposited carbon at 1560 cm^{-1}.[19] It is associated

to highly disordered carbonaceous materials which is $C-C$ bonds between aromatic rings with no less than 6 rings. Due to the very weak peak observed around 1380 cm^{-1}, and considering similar peak also observed before measurement, this may not be assigned to the coke formation but likely due to residual carbon in the anode introduced by the incomplete oxidized organic binder. Li and co-workers have also reported that residual carbon cannot be oxidized even after calcination 1673 K for 4 h. [20] Since the intensity of the peak is noticeably low, the slight increase of amorphous carbon after the cell measurement is presumed to be carbonaceous deposit from C_3H_8 pyrolysis and may not be assigned to the coke formation.

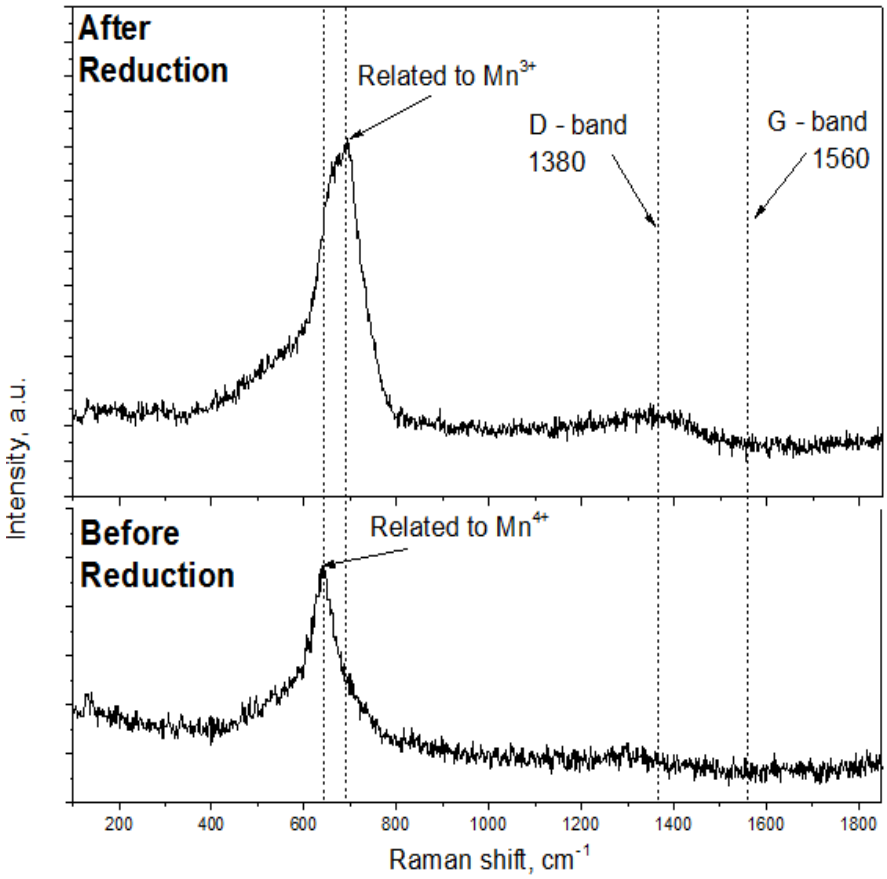

Figure 3.16 Comparison of Raman spectra of $La_{0.5}Sr_{0.5}Mn_{0.7}Al_{0.1}Co_{0.2}O_3$ anode before and after the power generating test using C_3H_8 fuel at 1173 K

However, the detection limit of Raman spectra shows that carbon is barely observed. Hence, X-ray photoelectron spectroscopy (XPS) spectra was acquired to characterize the near-surface carbon element of LSMAC72 anode as shown in Fig. 3.17. A broad and asymmetric feature of C 1s at 282.45 eV is shown with a shoulder at the high energy side of the peak. However, since LSMAC72 is a metal containing oxide, it is widely known that Ar ion beam sputtering on metal containing oxide may inadvertently produce metal carbide. Since the distinct XPS photopeak at 282.45 eV might be a sputtering artefact, it should be ruled out from the sample.[21] Meanwhile, a weak shoulder $C-C$ bonding is observed at 284.55 eV even before the anode is exposed for power generation test. The elucidation for this observation might be an indication of residual carbon from the introduction of organic binder. Additionally, since carbon containing impurities like carbon monoxide are always a part of vacuum ambient they are adsorbed onto the freshly sputtered oxide surfaces inside the XPS specimen chamber.[22]

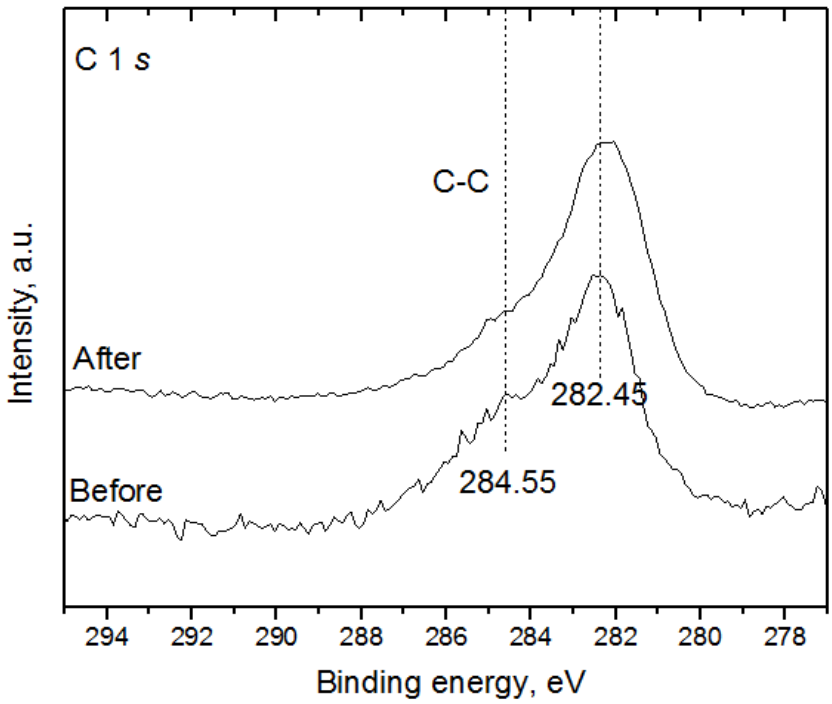

Figure 3.17 XPS spectra for C1s of $La_{0.5}Sr_{0.5}Mn_{0.7}Al_{0.1}Co_{0.2}O_3$ anode before and after the power generating test using C_3H_8 fuel at 1173 K

Upon conclusion of power generation test, both peaks remain fairly unchanged with the exception of slightly weaker $C-C$ peak, suggesting no formation of distinct carbon structure. Evidently, graphite bonding energy which is around 284.8 eV is not clearly observed, in agreement with the result shown by Raman spectra and EDS imaging. Therefore, Co doping on LSMA anode still shows low activity to coke deposition on anode under C_3H_8 feed condition. This suggests that LSMAC anode is promising as the oxide anode for H_2 as well as C_3H_8 fuel.

Furthermore, SEM characterisation was conducted on the surface and the cross sectional area of the cell after power generation measurement (Fig. 3.18). Clearly, there is no visible carbon structure on the anode after operation in C_3H_8, due to the presence of Co dopant in the anode that allows higher stability against carbon formation (Fig. 3.18 (a)).[18] Further analysis on the anode surface by using EDX scanning shows the lack of any distinctive shape confirming no coking has taken place. Similarly, good interphase contact between LSMAC72 anode and LSGM electrolyte particles without anode delamination were observed even after reduction in Fig. 3.18 (b). Certainly, there is no clear formation of carbon structure even at the boundary between anode and electrolyte, a common occurrence for Ni-based anode. It is noteworthy that no coke formation is observed even though normally, higher hydrocarbons like C_3H_8 easily form coke under SOFC power measurement conditions. Considering the high operating temperature in this study, the carbon species deposited is more tar-like rather than filamentous, formed by the unavoidable gas phase kinetic route. [23-25] While carbonaceous thin film may be deposited on the anode surface, it is formed by the free-radical reaction. It is fairly easier to remove by oxidation at lower temperature than graphite, not to mention Co metallic incline to have lower degree of coking compared to Ni.[26] Additionally, from X-ray image in Fig. 3.18, amount of C is not significantly increased after measurement. Therefore, Co doping on LSMA anode still shows low activity to coke deposition on anode under C_3H_8 feed condition due to its high selective catalytic

activity towards dehydrogenation rather than $C-C$ scission. This suggests that LSMAC anode is promising as the oxide anode for H_2 as well as C_3H_8 fuel.

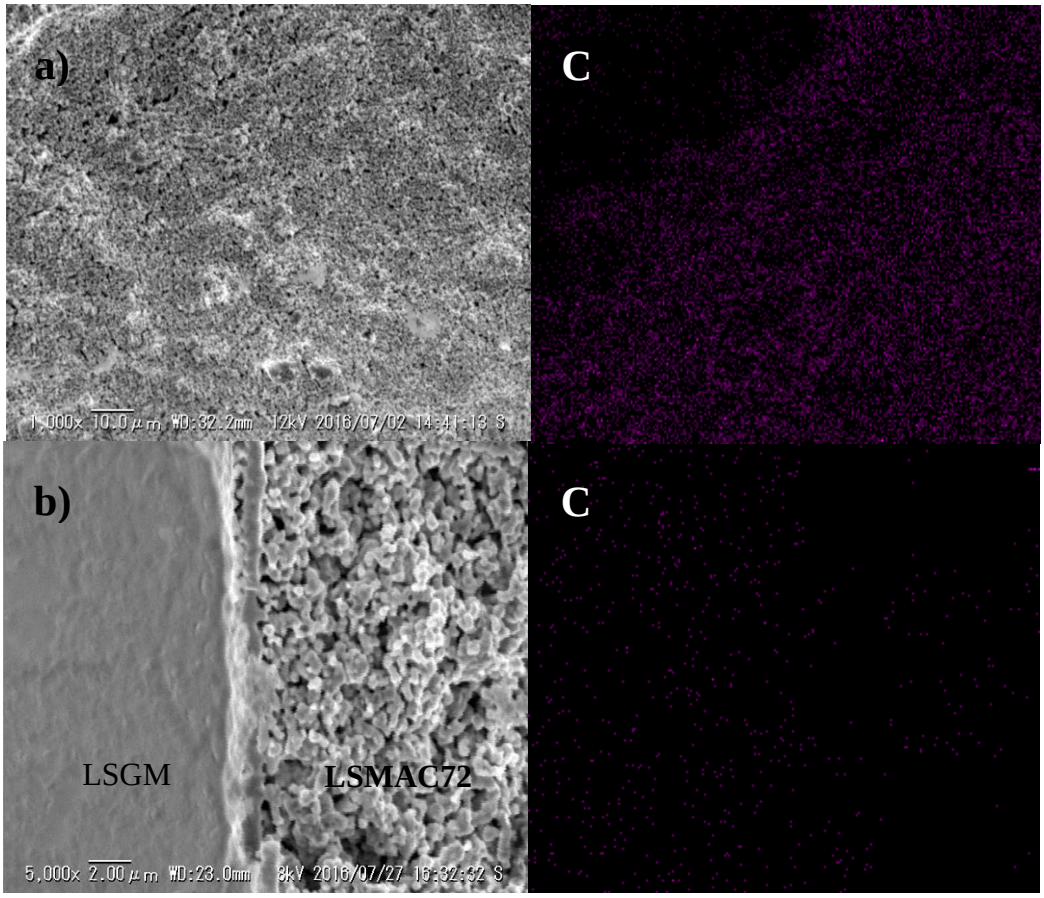

Figure 3.18 SEM image and EDS scan of $La_{0.5}Sr_{0.5}Mn_{0.7}Al_{0.1}Co_{0.2}O_3$ anode after the power generating test using C_3H_8 fuel at 1173 K on (a) surface (b) cross section

3.4 Conclusion

$La_{0.5}Sr_{0.5}MnO_3$ perovskite oxide doped with Co and Al was studied as oxide anode for direct hydrocarbon type SOFC. Although reasonable power density like 1 W/cm^2 and open circuit potential (1.1 V) at 1273 K was exhibited when H_2 was used as fuel, the power density as well as open circuit potential was significantly decreased when dry C_3H_8 was used for fuel in the case of LSM55. This decrease in power generation performance was assigned to decomposition of $LaMnO_3$ perovskite phase and low activity of La_2MnO_4 for C_3H_8 oxidation. It was found that stability of $LaMnO_3$ perovskite phase was increased by partial substitution of Mn with Al. However, the power density of the cell using LSMA anode is still insufficient when C_3H_8 is used for fuel. In this study, it was found that Co substitution in the Mn site is effective for increasing the power density of the cell, particularly for C_3H_8 fuel. At 20% Co doped (LSMAC72), similar electrochemical activity to LSM55 is achieved in H_2 (0.95 W/cm^2) while the largest MPD among all doped LSM55 studied is demonstrated when using C_3H_8 (0.25 W/cm^2) despite the use of thick LSGM electrolyte of 0.285 mm. The electrical conductivity of LSMAC72 is lower than that of LSM55 itself, however reduced IR loss is achieved during power generation in C_3H_8 possibly due to reduced interface resistance and better phase stability towards reduction. Consequently, the incorporation of Co may increase the catalytic activity of LSMA resulting in the increased performance in direct C_3H_8 oxidation. While decomposition of crystal phase is still occurred, Al doping suppressed the phase separation and hence this study reveals that LSMAC72 as a possible new anode material in direct C_3H_8 oxidation.

Reference

(1) K.C. Stein, J.J. Feenan, G.P. Thomson, J.F. Shultz, L.J.E. Hofer, R.B. Anderson, J. Air Pollution Control Assoc. **10**(4), 275 (1960).

(2) Q. -H. Wu, M. Liu, W. Jaegermann, Mater. Letters, **59**, 1980 (2005).

(3) Y R. D. Shannon, Acta Crystallogr., **A32**, 751 (1976).

(4) N. Kallel, N. Ihzaz, S. Kallel, A. Hagaza, M. Oumezzine, J. Magn. Magn. Mater., **321**, 2285 (2009).

(5) M. Hazzez, N. Ihzaz, M. Boudard, M. Oumezzine, Physica B, **487**, 78 (2016).

(6) J. Maček, B. Novosel, M. Marinsek, J. European Ceramic Soc. **27**, 48 (2007).

(7) Q. X. Fu, F. Tietz, P. Lersch, D. Stover, Solid State Ionics, **177**(11-12), 1059 (2006).

(8) Q. X. Fu, F. Tietz, D. Stover, Solid State Ionics, **177**, 1819 (2006).

(9) A. M. Kamarul Bahrain, S. Ida, T. Ishihara, J. Solid State Electrochemistry, (2016) doi:10.1007/s10008-016-3356-7.

(10) H. He, J. M. Vohs, R. J. Gorte, J. Power Sources, **144**(1), 135 (2005).

(11) T. Ishihara, S. Fukui, M. Enoki, & H. Matsumoto, J. Electrochem. Soc., **153**(11), A2085 (2006).

(12) N. Mironava-Ulmane, A. Kuzmin, M. Grube, J. Alloys Compd., **480**, 97 (2009).

(13) B. Hu, A.B. Getsoian, N.M. Schweitzer, U. Dass, H. Kim, J. Niklas, O. Poluektov, L. A. Curtiss, P. C. Stair, J.T. Miller, A. S. Hock, J. Catal., **322**, 24 (2015).

(14) C. -W. Tang, C. -B. Wang, S. -H. Chien, Thermochemica Acta, **473**, 68 (2008).

(15) G. Kim, S. Lee, J. Y. Shin, G. Corre, J. T. S. Irvine, J. M. Vohs, R. J. Gorte, Electrochem. Solid-State Lett., **12**(3), B48 (2009).

(16) C. Cho, B. Choi, K. Lee, J. Alloys Compd., **541**, 433 (2012).

(17) D. B. Ingram, S. Lunic, J. Electrochem. Soc., **156**, B1456 (2009).

(18) A. Fuerte, R. Valenzuela, M. Escudero, L. Daza, J. Power Sources, **196**(9), 4324 (2011).

(19) K. S. Blinn, H. Abernathy, X. Li, M. Liu, L. A. Bottomley, M. Liu, Energy Environ. Sci., **5**(7), 7913 (2012).

(20) C. Li, Y. Shi, N. Cai, J. Power Sources, **225**, 1 (2013).

(21) A. Jaramillo, L.D. Spurlock, V. Young, A. Brajter-Toth, Analyst, **124**, 1215 (1999).

(22) Rajesh Kumar Tiwari, (2002) Dissertation for the degree of Doctor of Philosophy in Chemistry. Faculty of the Virginia Polytechnic Institute and State University, p.111,Available:https://theses.lib.vt.edu/theses/available/etd-08052002-102300/unrestricted/03rktiwari.pdf [2016, July 15].

(23) C. Y. Sheng, A.M. Dean, J. Phys. Chem. A, **108**, 3772 (2004).

(24) G. K. Gupta, A. M. Dean, K. Ahn, R. J. Gorte, J. Power Sources, **158**, 497 (2011).

(25) B. Descamps, G. L. Vignoles, O. Féron, J. Lavenac, F. Langlais, J. Phys. IV France, **11**, Pr3-101, (2001).

(26) S. -I. Lee, J. M. Vohs, R. J. Gorte, J. Electrochem. Soc., **151**(9), A1319 (2004).

Chapter 4

Composite Oxide Consisting of $La_{0.5}Sr_{0.5}Mn_{0.7}Al_{0.1}Co_{0.2}O_3$ for Increasing Anodic Activity

4.1 Introduction

In Chapter 3, we have verified that doping Al and Co to the Mn site of LSM55 is effective for increasing the phase stability and anodic electrochemical activity particularly when dry C_3H_8 was used for fuel. In particular, co-doping 20 mol% Co and 10 mol% Al to the Mn site of LSM55 (LSMAC72) shows comparable cell performance (0.95 W/cm^2 in H_2) to LSM55 in case of H_2 fuel while superior power density when utilizing C_3H_8 fuel is achieved up to ca. 4 times 0.25 W/cm^2. The fact that coking is mitigated when using LSMAC oxides is an accomplishment of the novel oxide anode, but when compared to the reported power density of the reported oxide anodes for direct hydrocarbon SOFC,[1-4] the anodic activity is still insufficient partly due to low electrical conductivity (large IR loss) and most likely because of partial decomposition of perovskite structure is still occurred. Consequently, mixing with oxide which is conductive and tolerant in reducing atmosphere was studied in this chapter for enhancing power density of direct C3H8 fuel SOFC.[4, 5]

As mentioned in Chapter 1, composite material is an alternative option when obtaining good electronic conductivity and catalytic activity in a single anode which can not achieved simultaneously. The current state-of-the-art Ni-YSZ anode itself is a cermet, a composite of 8%YSZ ceramic oxide and Ni metal. Barnett and co-workers have investigated the use of composite SOFC anodes with various levels of gadolinium doped ceria (GDC). The results provide additional evidence on the stability of ceria-based anodes operating under hydrocarbon fuel like methane, ethane, propane, octane, and butane.[6, 7] They reported a combination of Ru-CeO_2 catalyst layer with a conventional Ni-YSZ anode, allowing internal reforming of iso-octane without coking and yields stable power densities of 0.3 - 0.6 W/cm^2 for operating temperatures in the range of 943 K – 1043 K. Barnett and co-workers conclude that while the catalytic activity of CeO_2 by itself is insufficient for hydrocarbon reforming,

doped CeO_2 is a MIEC and its tolerance to anode degradation along with modest catalytic activity makes it an attractive candidate for inclusion in composite anodes.[8]

Likewise, a composite anode of infiltrated GDC and host Nb-doped $SrTiO_3$ (STN) exhibited an extremely low polarization resistance of 116 $m\Omega cm^2$ at 1123 K under symmetrical cell condition when H_2 is used for fuel.[9 - 11] Although $Sr_{0.94}Ti_{0.9}Nb_{0.1}O_3$ (STN) exhibited the high electrical conductivity properties, electrocatalytic activity towards fuel oxidation is not high. The charge compensation by Sr deficient in STN changes the main charge carrier by formation of Ti^{3+}, and resulting in Ti-enriched secondary phase in Sr-deficient materials. GDC was thus considered to be highly active to catalytic oxidation. On the other hand, in order to achieve high electronic conductivity, Shin et al.[12] employed a composite perovskite consisting of $La_{0.6}Sr_{0.4}Fe_{0.9}Mn_{0.1}O_3$ (LSFM) and $Ce_{0.6}Mn_{0.3}Fe_{0.1}O_2$ (CMF) as the anode and was measured against hydrogen and various hydrocarbon fuels such as methane, ethane, propane and butane. High anodic activity was achieved and MPD around 1 W/cm^2 was exhibited at 1073 K when C_3H_8 is used. The authors assigned the high performance to the reduced IR loss and anodic overpotential, which may contributed by the n-type conductivity of CMF. The terminal potential is also stable for more than 50 h under C3H8 fuel. Another significant results are no coke formation observed even though heavy hydrocarbon like C_3H_8 or C_4H_{10} directly is used for fuel.

The current study aims to further increase in anodic property of LSMAC by mixing several oxide for composite. Since LSMAC72 shows the best cell performance in both H_2 and C_3H_8, it is chosen as the matrix while the filler constituent is made up of either GDC, LSFM, LSGM, CMF or STN. The composite of LSMAC72 + oxide anode is anticipated to perform better than single LSMAC anode in C_3H_8 fuel.

4.2. Experimental

4.2.1. Synthesis and characterization of oxide anodes

Similar sol-gel combustion method as in Chapter 3 was employed for the preparation of $La_{0.5}Sr_{0.5}Mn_{0.7}Al_{0.1}Co_{0.2}O_3$ perovskite oxide (LSMAC72). The starting materials for LSMAC72 were $La(NO_3)_3.6H_2O$ (99.9% Wako Pure Chemical Co. Ltd., Japan), $SrNO_3$ (98% Chameleon Reagent, Japan), $Mn(NO_3)_2.6H_2O$ (99.9% Wako Pure Chemical Co. Ltd., Japan), $Al(NO_3)_3.9H_2O$ (98% Wako Pure Chemical Co. Ltd., Japan) and $Co(NO_3)_2.6H_2O$ (98% Wako Pure Chemical Co. Ltd., Japan). The metal nitrates were allowed to mix and dissolve in deionized water by continuous stirring on a magnetic hotplate. Once the citric acid, $C_6H_8O_7.H_2O$ (99.5% Wako Pure Chemical Co. Ltd., Japan) is added, the temperature of the solution was increased to 423 K until the solution turned to viscous gel and then heated to allow self-combustion of the gel which instantly yield ashes precursor. To remove any nitrate residues, the ash is subjected to heat treatment at 673 K before finally calcined at 1523 K.

The preparation of $Ce_{0.8}Gd_{0.2}O_2$ (GDC) and $Sr_{0.94}Ti_{0.9}Nb_{0.1}O_3$ (STN) used the conventional solid-state reaction method. For GDC, powders of CeO_2 (99.9% Rare Metal Co. Ltd., Japan) and Gd_2O_3 (99.9% Kishida Chemical Co., Japan) were ground in a mortar before pre-calcination at 1273 K for 6 h. After the heat treatment, the oxide was then ground again and pelletized prior to sintering at 1773 K for 6 h in air. The obtained pellet is pulverized before ball-milled at 200 rpm for 30 min. Similarly for the synthesis of STN, $SrCO_3$ (99.9% Rare Metal Co. Ltd., Japan), TiO_2 (99.9% Rare Metal Co. Ltd., Japan) and Nb_2O_5 (99.9% Kishida Chemical Co., Japan) were mixed and sintered at 1373 K for 2 h in 7%H_2-N_2.

Both $Ce_{0.6}Mn_{0.3}Fe_{0.1}O_2$ (CMF) and $La_{0.6}Sr_{0.4}Fe_{0.9}Mn_{0.1}O_3$ (LSFM) were also prepared via solid-state route of $Ce(NO_3)_2.6H_2O$ (98% Kishida Chemical Co., Japan), $La(CH_3COO)_3.1.5H_2O$ (90% Kishida Chemical Co., Japan), $SrNO_3$ (98% Chameleon Reagent, Japan), $Mn(NO_3)_2.6H_2O$ (99.9% Wako Pure Chemical Co. Ltd., Japan), $Mn(CH_3COO)_2.4H_2O$ (99% Kishida Chemical Co., Japan) and $Fe(NO_3)_3.9H_2O$ (99.9% Wako Pure Chemical Industries Ltd., Japan). The respective raw materials were dissolved in deionized water under continuous stirring on a magnetic hot plate and the solution was completely evaporated. The precursor was then treated to pre-calcination at 673 K for 2 h. The resultant oxide was then ground using mortar before sintered at 1473 K for 6 h. The composite oxide of LSMAC72 and the respective oxide anodes was prepared by mixing at the weight ratio of 90 wt% LSMAC72: 10 wt% oxide anode. An appropriate amount of ethyl cellulose is used as a binder and the composite is turned into paste by adding isobutyrate as the solvent. The composite mixture was then homogenized by using a conditioner mixer (Thinky AR-100).

The $La_{0.9}Sr_{0.1}Ga_{0.8}Mg_{0.2}O_3$ (LSGM) electrolyte and $Sr_{0.5}Sm_{0.5}CoO_3$ (SSC) cathode were prepared by solid-state reaction method. For the preparation of LSGM, commercial oxides of La_2O_3 (99.9% Kishida Chemical Co., Japan), Ga_2O_3 (99.9% Mitsubishi Materials Corporation, Japan), MgO (99.9% Wako Pure Chemical Co. Ltd., Japan), and $SrCO_3$ (99.9% Kishida Chemical Co., Japan) were mixed in alumina mortar before pre-calcination at 1273 K for 6 h. After palletization, it was sintered at 1773 K for 6 h. $Sr_{0.5}Sm_{0.5}CoO_3$ was synthesized by continuous heating and stirring of $Sr(CH_3COO)_2.0.5H_2O$ (99% Wako Pure Chemical Co. Ltd., Japan), Sm_2O_3 (99.9% Nacalai Tesque Inc., Japan) and $Co(NO_3)_2.6H_2O$ (98% Wako Pure Chemical Co. Ltd., Japan) dissolved in deionized water until evaporated. Pre-calcination takes place at 673 K, before the powder was fired at 1273 K in air. Commercial X-ray diffractometer, XRD (Rigaku, RINT2500) is used for phase determination of all obtained powder oxides.

4.2.2 Fabrication of single cell and anodic performance measurement technique

The electrolyte-supported single cell using LSGM (ca. 0.3 mm thickness) was prepared by screen printing method in similar manner to previous chapters. The composite LSMAC72 + oxide anode and SSC cathode paste was painted on each side of LSGM disc with a diameter of 5 mm. Platinum mesh (5×5 mm) was lightly pressed on top of the anode as current collector. Reference electrode is prepared using the commercial Pt paste (Tanaka TR7902) that is set close to cathode with a platinum lead wire connected to the Pt reference electrode. The cell was then baked at 1373 K for 1 h. Conventional four-probe method is used to measure the power generating property of the cell. In the meantime, to reduce the degree of phase decomposition from H_2 reduction, the fuel setup in the current study is changed by only supplying dry C_3H_8 rather than firstly supplying H_2 followed by C_3H_8 fuel. The flow rate of the supplied gas was maintained at 100 mL/min. To measure the terminal voltage, constant dc current was supplied by using galvanostat (Hokuto Denko HA-151A) and displayed by digital multimeter (Advantest, type R 6451A). Estimation of the internal resistance was conducted using current interruption method with dc current pulse generated by current pulse generator (Nikko Keisoku, NCPG 10-1). Digital memory recorder (Hioki 8835) was used to record the potential response. The impedance measurement was conducted using the impedance/gain-phase analyzer (Solartron type 1255B, Solartron) with the electrochemical interface (Solartron type 1287, Solartron).

Phase stability of the cell after the power generation test was conducted by XRD (Rigaku, RINT2500) immediately after the measurement was finished. Analysis of carbon deposition on the anode material after the cell test was conducted by using scanning electron microscope (SEM) (VE-7800, Keyence Co.) with Energy Dispersive Spectrometry (EDS) instrument (EDAX Co., Ltd.) for elemental analysis as well as by Raman spectroscopy (Horiba HR800).

4.3. Results and Discussion

4.3.1 Anodic performance of LSMAC72 composite oxides

LSMAC72 composites were prepared with various oxide anodes, denoted as LSMAC72+STN, LSMAC72+CMF, LSMAC72+LSFM, LSMAC72+LSGM and LSMAC72+GDC respectively at weight ratio 90 wt% LSMAC72; 10 wt% oxide anode. 10 wt% oxide anode is fixed as the minimal content to gauge the effect of additives to the cell performance. Dry C_3H_8 is supplied as the fuel and the power generation measurement of the cell is measured from 1173 K to 973 K. Figure 4.1 (a) shows the power generation curves of LSMAC72 and the composites at 1173 K using direct dry C_3H_8 fuel. By directly feeding C_3H_8 without prior reduction in H_2, the cell performance of LSMAC72 doubled to ca. 530 mW/cm^2 from ca. 250 mW/cm^2 likely due to lower degree of phase decomposition. Notably, all composites especially LSMAC72+STN, LSMAC72+GDC and LSMAC72+CMF show hugely improved anodic activity than LSMAC72 with MPD of ca. 830, 729 and 800 mW/cm^2 respectively. The highest MPD is shown by composite LSMAC72 with STN > CMF > GDC > LSFM > LSGM > LSMAC72. While current limiting effect is observed at high current density for almost all composites, they are not as profound as the LSMAC72 anode itself, suggesting reduced diffusion overpotential by oxide anodes addition despite at relatively small content.

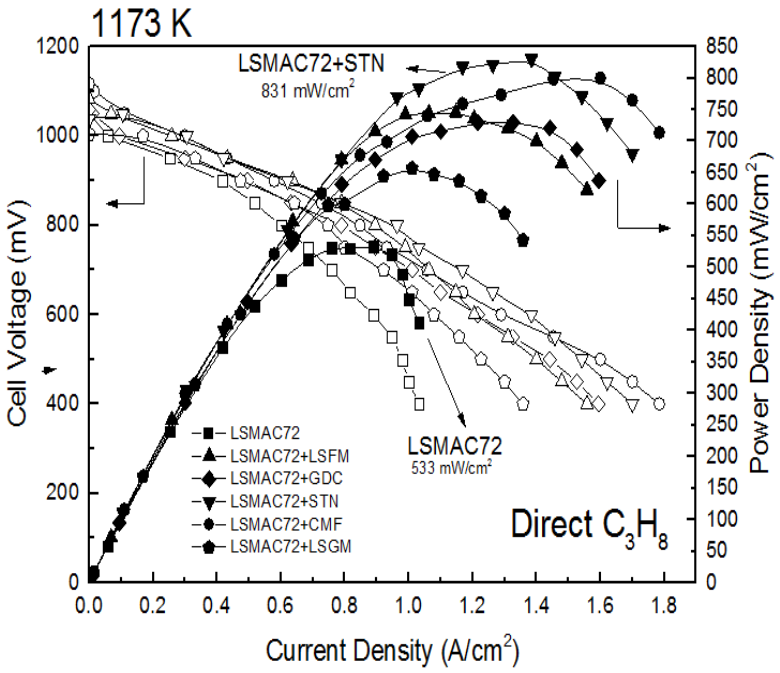

(a)

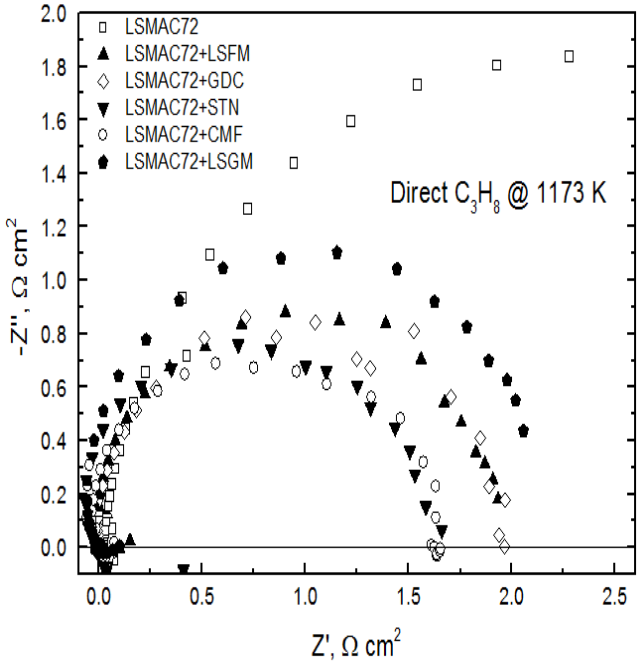

(b)

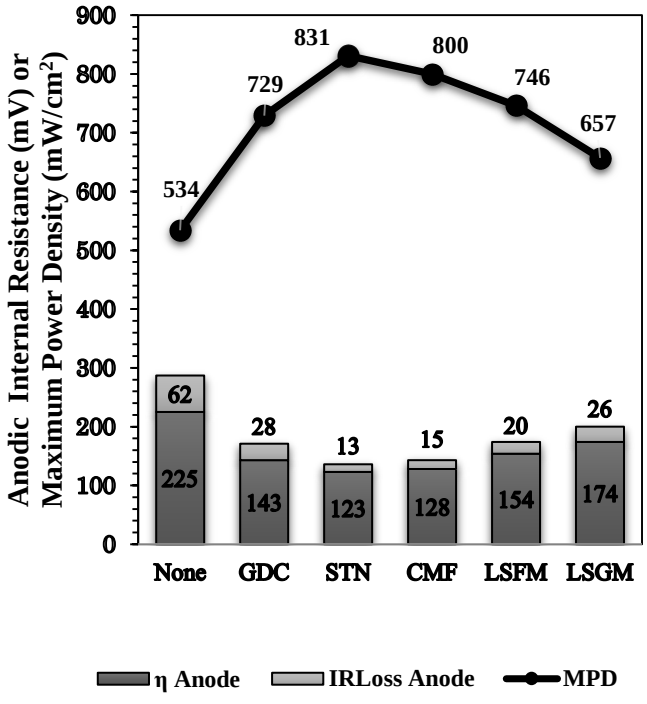

(c)

Figure 4.1 (a) I-V/P curve of the cell using composite $La_{0.5}Sr_{0.5}Mn_{0.7}Al_{0.1}Co_{0.2}O_3$ + oxide anodes operating with direct C_3H_8 fuel at 1173 K; (b) Anodic Nyquist impedance spectra and (c) Anodic internal resistance of the composite at current density of 0.3 A/cm^2

Based on the Nyquist anodic impedance spectra (Fig 4.1 (b)), all composite LSMAC72 show low and closely similar anodic ohmic losses but varies greatly in terms of the overpotential. It is evident that anodic overpotential is the dominant potential loss as shown with the large impedance arc at low frequency. This is expected due to multiple competing reactions associated with hydrocarbon gas oxidation. Interestingly, addition of oxide anode slightly reduces the ohmic loss but the effect is more apparent with reduced anodic overpotential as demonstrated by all composites compared to LSMAC72 anode. Particularly, both composite LSMAC72+CMF and LSMAC72+STN show the lowest anodic overpotential at ca. 1.63 Ωcm^2. To clarify the losses from anodic contribution, the internal loss is estimated by using current interruption method at current density of 0.3 A/cm^2 as shown in Fig. 4.1 (c). LSMAC72 shows the largest anodic ohmic loss and overpotential. By adding 10 wt% oxide anode, both ohmic and overpotential reduced especially for composite loaded with STN or CMF. Improved performance for the LSMAC72+CMF might be attributed to catalytic activity of CeO_2 towards hydrocarbon fuel, facilitating water gas phase reaction as well as allowing faster kinetic for C_3H_8 oxidation mechanism hence lower anodic overpotential. Meanwhile, enhanced MPD for composite LSMAC72+STN and the low ohmic loss can be ascribed to the high electrical conductivity of STN. $Sr_{0.94}Ti_{0.9}Nb_{0.1}O_3$ is reported to have electrical conductivity of ca. 127 S/cm at 1273 K at P_{o2} = -20.5 atm which is more than sufficient for anode.[9] This result visibly shows mixing effect of oxide anode in reducing the electrode resistance of LSMAC72 when using direct C_3H_8 fuel.

Surprisingly at 1073 K, instead of composite anode LSMAC72+STN or CMF, LSMAC72+GDC shows the highest MPD at 464 mW/cm^2 (Table 4.1). LSMAC72 anode again shows the lowest cell performance in comparison to the composites. The main cell resistance of the anodes still derived from the overpotential loss and corresponds to the MPD result, the lowest anodic overpotential is shown by composite LSMAC72 with GDC. As expected, LSMAC72 shows the largest

anodic overpotential possibly due to microstructural changes from phase decomposition. However at 973 K, all composite anodes show negligible cell performance (MPD < 30 mW/cm^2). Both LSMAC72+GDC and LSMAC72+LSGM only top the MPD at ca. 28 mW/cm^2. The anodic overpotential still represents the major loss for all anodes.

Table 4.1 OCV and MPD of LSMAC72 + 10wt% oxide anodes in direct C_3H_8 at 1173 – 973 K

Operating Temperature (K)	**LSMAC72+10wt% Oxide Anode** **Oxide**	**OCV**	**MPD**	**Anodic internal resistance (mV)**	
		(mV)	**(mW/cm^2)**	**η_{An}**	**IR_{An}**
1173	**None**	1050.00	533.00	225	62
	STN	1038.04	831.00	123	13
	CMF	1116.75	800.25	128	15
	LSFM	1081.66	745.00	154	20
	GDC	1058.15	729.00	143	28
	LSGM	1014.20	657.00	174	26
1073	**None**	1028.65	121.58	341	74
	STN	1134.56	348.95	279	28
	CMF	1100.87	331.84	262	31
	LSFM	1090.42	240.00	240	34
	GDC	1130.04	464.21	199	35
	LSGM	1140.37	372.89	253	39
973	**None**	1003.77	5.91	476	82
	STN	1228.83	21.08	315	39
	CMF	1213.76	20.84	321	44
	LSFM	1131.66	16.87	336	42
	GDC	1173.37	27.95	278	47
	LSGM	1245.84	27.50	311	44

Fuel: Dry C_3H_8 **Cathode**: SSC **Electrolyte**: LSGM Potential drop at 0.3A/cm^2

Fig. 4.2 represents the *ex-situ* SEM micrographs of the composites surface after power generation measurement at 973 K. Since LSMAC72+STN shows the largest MPD at 1173 K while LSMAC72+GDC shows averagely high MPD at all temperature measured, emphasis was given on their microstructure before the measurement as well (Fig. 4.2 a) & b)). The particle size for LSMAC72+GDC of ca. 1 – 2 µm is seems to be preserved after the reduction in Fig. 4.2 c), an obvious benefit of composite mixing. Good percolation and interconnection is shown after reduction while at the same time porosity of the anode seems to be sustained, allowing better gas diffusion. Hence, it can be confirmed that lower overpotential observed by LSMAC72-GDC is due to preserved porosity while consequently catalytic oxidation of C_3H_8 is enhanced through the addition of GDC. Meanwhile, combination of large particle size from STN (3 - 4 µm) and smaller particles from LSMAC72 is shown for LSMAC72+STN in Fig. 4.2 (b). However, the surface micromorphological of the composite in Fig. 4.2 d) shows the large STN particles diminished after the reduction in C_3H_8 suggesting poor chemical stability. While the porosity seems visible, it is likely the microstructural changes contributes to the large overpotential observed especially at 973 K. Likewise, other composites show similar microstructural features like LSMAC72+STN after the power generation measurement as shown in Fig. 4.2 f) – h).

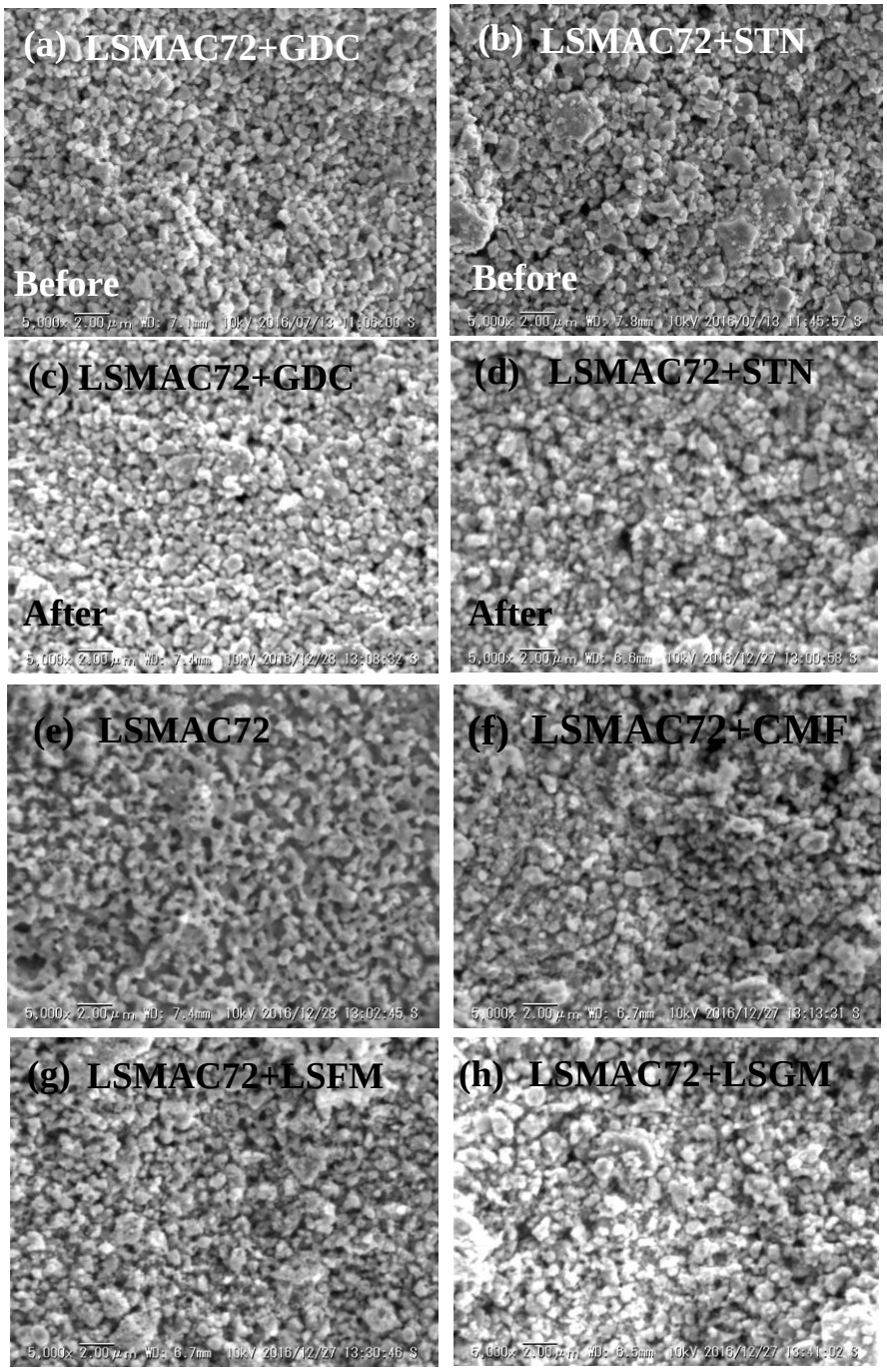

Figure 4.2 SEM images for anode surface before power generation measurement in C_3H_8 at 973 K for composite a) LSMAC72 + GDC; b) LSMAC72 + STN and after c) LSMAC72 + GDC; d) LSMAC72 + STN; e) LSMAC72; f) LSMAC72 + CMF; g) LSMAC72 + LSFM and h) LSMAC72 + LSGM

Fig. 4.3 shows the carbon elemental distribution map on the surface of the composite after power generation measurement in C_3H_8 at 973 K. Amongst all composites, only LSMAC72+GDC shows uniformly distributed carbon mapping with no distinctive structure shape suggesting the carbon detected might be deposits from gas-phase reaction rather than graphitic or filamentous based. This is anticipated since GDC increases the catalytic activity of hydrocarbon oxidation. Besides, the presence of GDC has been proven to be effective in mitigating carbon formation when using hydrocarbon fuel.[13] However, LSMAC72, composite LSMAC72+ CMF, LSMAC72+STN and LSMAC72+LSFM particularly exhibit carbon concentration on the surface. Considering that STN and LSFM does not have any catalytic activity towards hydrocarbon oxidation and serves to increase the anode electrical conductivity, the carbon agglomeration is expected. In fact, the carbon deposits with LSFM addition seems higher than LSMAC72 itself (Fig. 4.3 a)). This result again confirms the feasibility of LSMAC72 as a carbon tolerant anode as well as proven the GDC assistance in mitigating carbon formation in direct hydrocarbon SOFC.

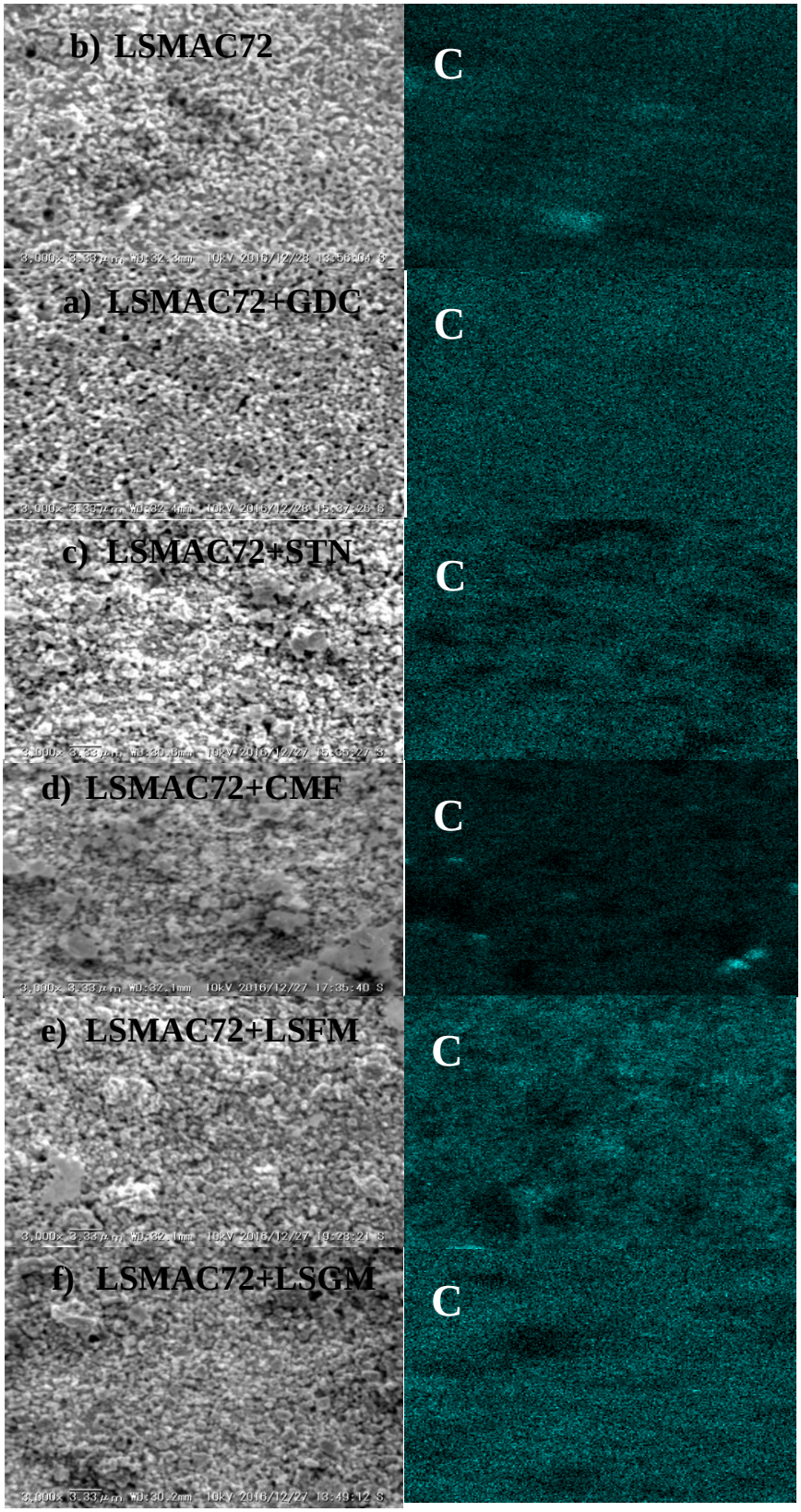

Figure 4.3 Surface SEM images and EDS scan for carbon element after power generation measurement in C_3H_8 at 973 K for a) LSMAC72; b) with GDC; c) with STN; d) with CMF; e) with LSFM and f) with LSGM

Since the error of EDS analysis in detecting low atomic weight element like C is relatively large and the results are usually quasi-quantitative, Raman spectroscopy has been conducted on the surface of LSMAC72 anode after the power generating measurement in dry C_3H_8 at 973 K (Figure 4.4). It is notable that Raman spectrum for LSMAC72+GDC corresponds to the EDS result where D-band and G-band spectrum in 1200 – 1750 cm^{-1} region barely exists. However, graphitic formation is detected for LSMAC72+CMF and LSMAC72+STN but more prominently observed for LSMAC72+LSFM due to the existence of both D- and G-band.

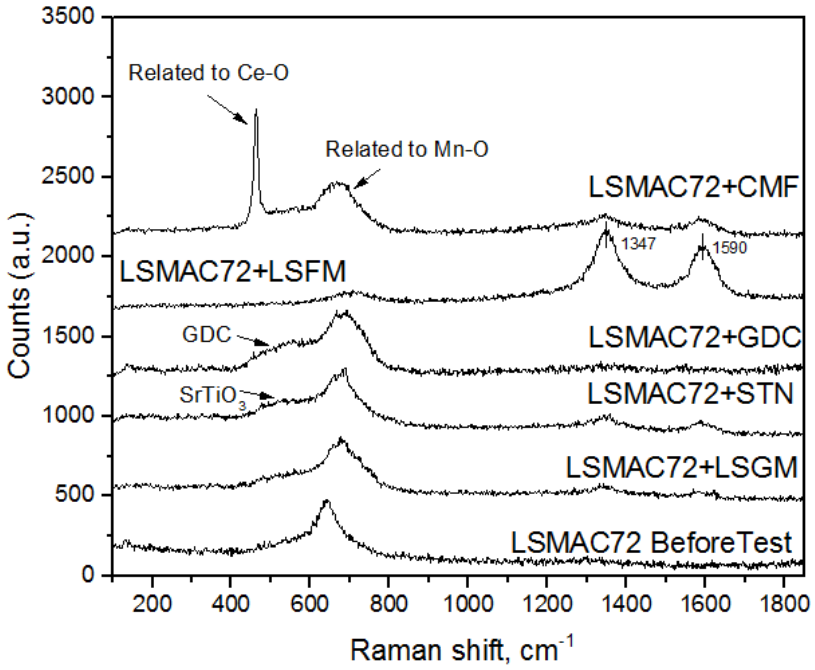

Figure 4.4 Raman spectra of composite LSMAC72 anodes after the power generating measurement using C_3H_8 fuel at 973 K

Fig. 4.5 shows the XRD pattern of all composites measured *ex-situ* after power generation test in C_3H_8 at 973 K. Weak $LaMnO_3$ perovskite peaks still observed for all composites but similar to single anode LSMAC72, peaks assigned to La_2MnO_4 were also observed around 32°. For LSMAC72+GDC, additionally, cubic CeO_2 phase is partly decomposed to Ce_2O_3 due to severe

reduction of cerium from Ce^{4+} to Ce^{3+} as

$$O_O^x \leftrightarrow \frac{1}{2}O_{2(g)} + V_O^{\cdot\cdot} + 2e' \quad (4\text{-}1)$$

$$Ce^{4+}(CeO_2) + e^{"} \leftrightarrow Ce^{3+}(Ce_2O_3) \quad (4\text{-}2)$$

The decomposition is consistent with the result shown by Kim and co-workers[13], suggesting the P_{O2} when C_3H_8 is supplied is lower than -25 atm.[12] However, similar to CMF, the reduction of CeO_2 assists the oxidation of hydrocarbon fuel for GDC. While there is no detailed study conducted on the phase stability of CMF under reducing environment, the phase stability of GDC has been shown to be stable under 1173 K up to P_{O2} < -24 atm.[13] In fact, the phase stability of GDC20 was reported to increase with lower temperature. On the other hand, the phase stability for all composites are quite similar and not severely degraded in terms of the presence of $(La, Sr)_2MnO_4$ phases. This is expected due to lower operating temperature than previous setup which starts at 1273 K compared to 1173 K in the current study. Additionally, by not initially reducing the anode under H_2 fuel which is a strong reducing agent, the LSMAC72 perovskite retains higher degree of phase stability. Hydrocarbons are known to act as a buffer to prevent changes in P_{O2} and the buffering effect increases with higher hydrocarbon.[14] Therefore, it is logical that while dry C_3H_8 itself is a reducing agent, the P_{O2} is held at favorable pressure, consequently improved the phase stability. However, the exception is for LSMAC72+LSFM that shows severely decomposed phase compared to other composites.

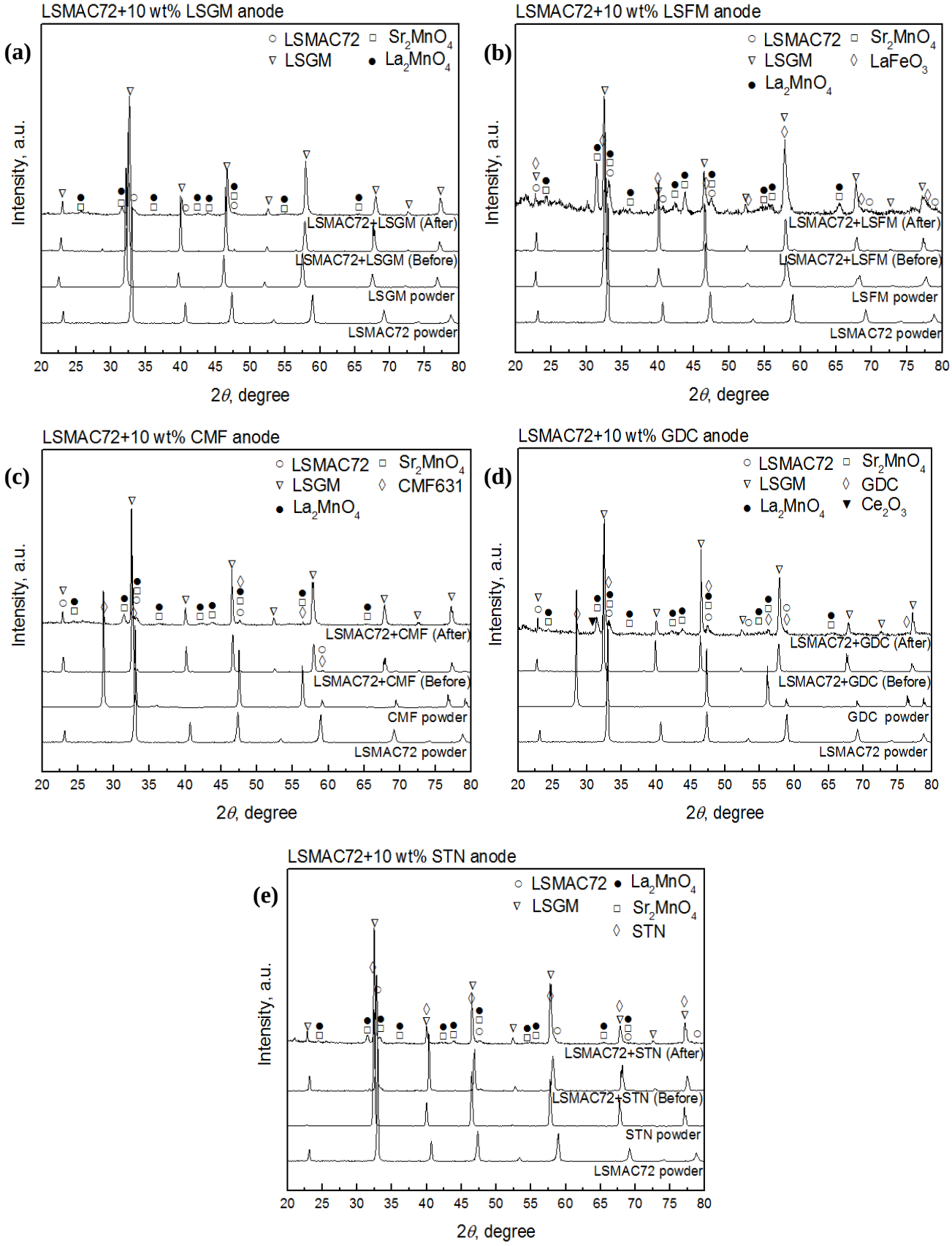

Figure 4.5 XRD pattern after reduction in C_3H_8 at 973 K for all LSMAC72 composite anodes

4.3.2 Anodic performance of LSMAC72+*x* wt% GDC composite oxides using direct dry C_3H_8 fuel

Based on the result of composite LSMAC72 anodes in section 4.3.1, while LSMAC72+STN shows the highest MPD at 1173 K, its performance rapidly dropped at lower temperature. Conversely, LSMAC72+GDC shows fairly high and stable performance at lower temperatures measured. Hence, further works was carried out to investigate the effect of GDC content to the cell performance of LSMAC72+GDC at 0 – 40 wt% as a function of temperature of 1173 K – 973 K. Fig. 4.6 (a) highlights the *IV-IP* for composite LSMAC72+GDC under direct C_3H_8 operation at 1173 K, prepared by hand mixing at GDC content from 0 - 40 wt%. At 1173 K, LSMAC72+20 wt% GDC shows the highest MPD at 827 mW/cm^2 which apparently exhibits similar performance to LSMAC72+10 wt% STN at 831 mW/cm^2.

The result exhibits a clear trend with the highest performance is shown at **20 wt% GDC > 10 wt% > 30 wt% > 40 wt% > 0 wt%**. Analyzing the corresponding anodic impedance spectra in Fig. 4.6 (b) clearly shows the effect of GDC addition. The anodic ohmic losses are fairly small but as expected the anodic overpotential are dominant at all GDC content. Notably, adding GDC decreases the anodic overpotential especially at 10 wt% GDC but gradually increases with higher GDC content. At 30 and 40 wt% GDC, it seems that additional semicircle appears at lower frequency but is not fully visible and did not make a second intercept with the real axis in the frequency range measured. The result seems to suggest that at higher GDC content, the limitation of mass transport is higher likely to limited gas diffusion. This is likely related to the microstructure of the anode and will be discussed later.

(a)

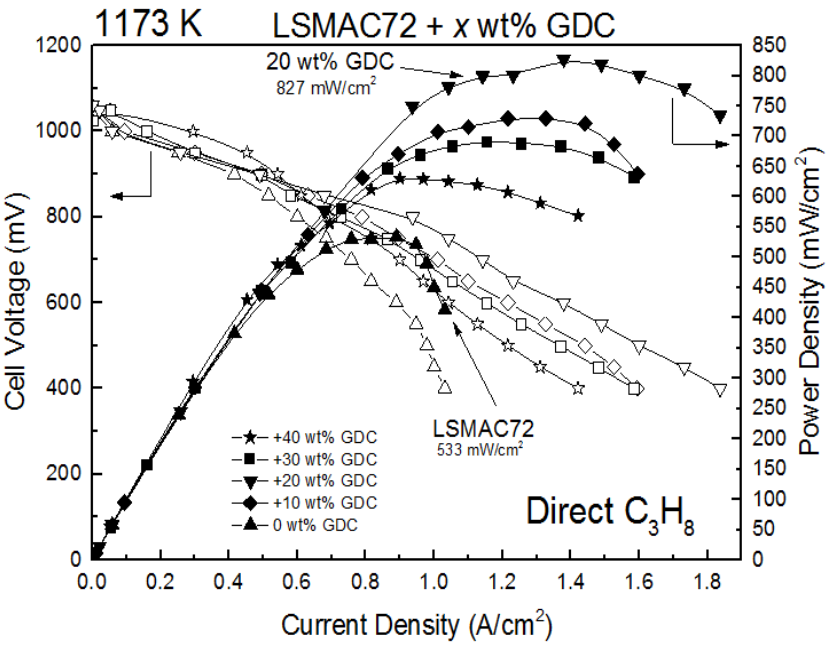

(b)

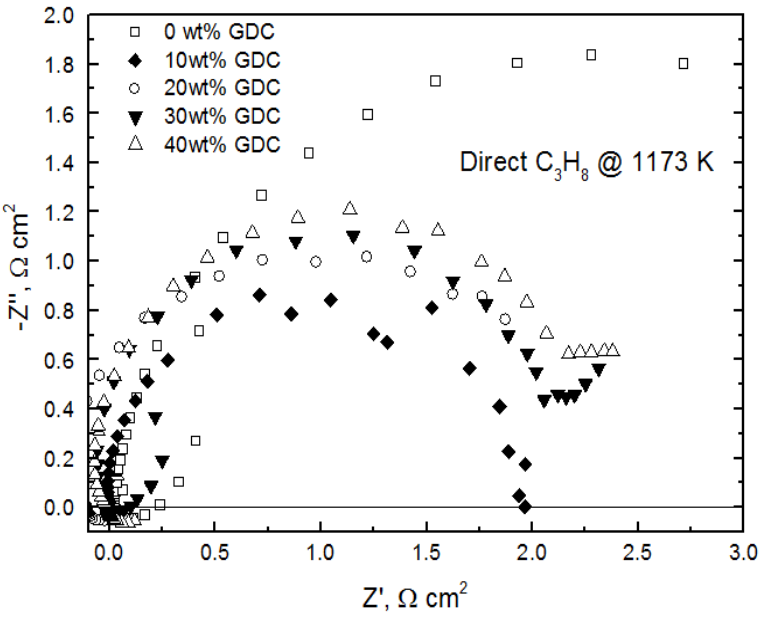

Fig. 4.6 (a) I-V/P curve of composite LSMAC72+GDC at different GDC content and (b) the corresponding Nyquist impedance spectra at 1173 K

The relationship between the MPD and anodic internal resistance is shown in Fig. 4.7 (a). Even though anodic overpotential is dominant at all GDC content, both anodic overpotential and ohmic loss are significantly reduced with the addition of GDC. While GDC has low electrical conductivity,

the fact that it is an MIEC might slightly help reduces the ohmic loss. In addition, it is probable that the interphase between the electrode and LSGM electrolyte is enhanced leading to plateaued ohmic loss with increasing GDC content. In Fig. 4.7 (b), the MPD trend is replicated at 1073 K, with LSMAC72 + 20 wt% GDC shows the highest MPD recorded thus far at 1073 K in this study at 515 mW/cm^2. Similarly, the anodic internal resistance is reduced by adding GDC but the anodic overpotential steadily increases and even higher at 30 and 40 wt%.

However, at 973 K, very poor performance at all GDC content is observed suggesting phase degradation of LSMAC72 under long operational condition as well as insufficient catalytic activity affecting the overall cell performance (Fig. 4.7 (c)). In addition, low conductivity of both LSMAC72 and GDC at lower temperature also didn't help improving the cell performance. Nevertheless, since the OCV shows incremental value with lower temperature up to 1.2 V at 973 K, no gas leakage can be confirmed. This result however confirms the effect of GDC addition at low GDC content in improving the anodic performance of LSMAC72 under direct C_3H_8 operation especially at 1173 and 1073 K.

Fig. 4.8 represents the surface SEM images for pristine composite LSMAC72+GDC at 0 - 40 wt% GDC content. Noticeably, the morphology of LSMAC72 changes by adding GDC as shown in Fig. 4.8 (b) – (e). The GDC particle is not clearly visible at 10 wt% but more obvious at higher GDC content particularly at 40 wt% (Fig. 4.8 (e)) which is more greyish and larger than LSMAC72. The SEM images reveals that the larger GDC particles in quasi-cuboid shape while the smaller LSMAC72 particles shape is mostly irregular. It is difficult to ascertain from the SEM images but it seems that while both particles connected the porosity might be reduced due to larger GDC particles as can be seen in Fig. 4.8 (e). This affects the mass transport and diffusion of reactant species, which explains the larger anodic overpotential with higher GDC content shown in Fig. 4.7.

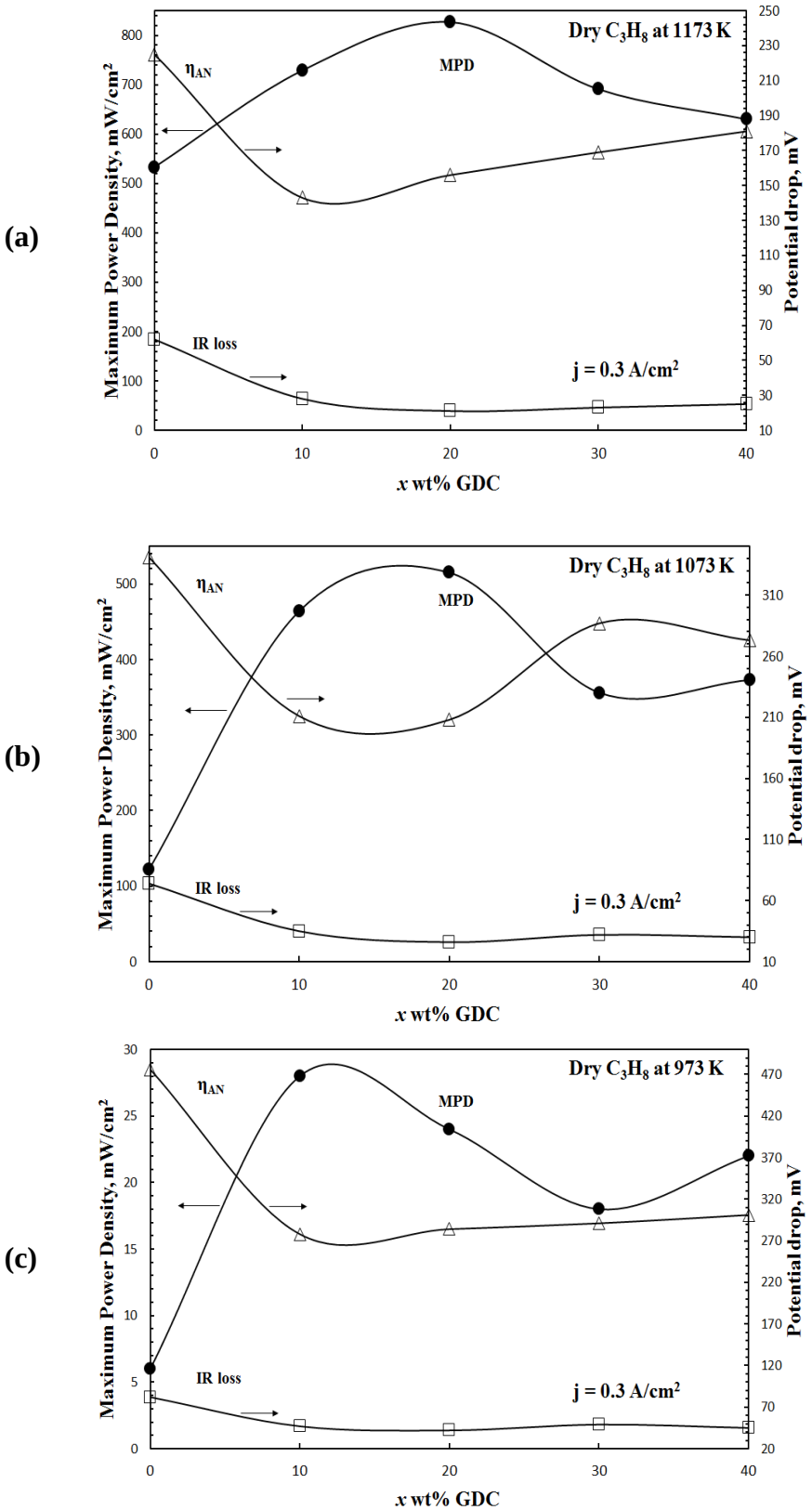

Fig. 4.7 Maximum power density of the cell as well as the potential drop by IR and anodic overpotential at 0.3 A/cm^2 in dry C_3H_8 environment as a function of GDC content in composite LSMAC72+GDC at (a) 1173 K; (b) 1073 K; (c) 973 K

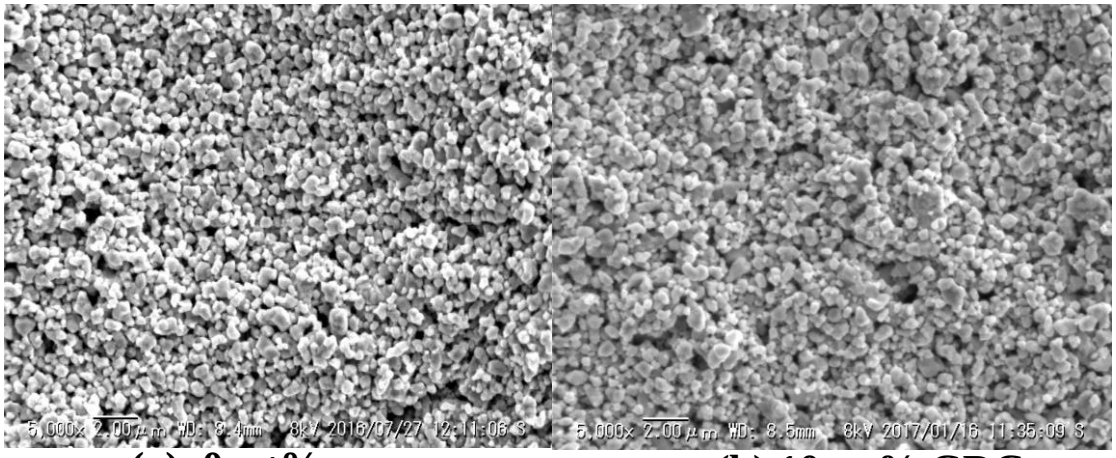

(a) 0 wt% (b) 10 wt% GDC

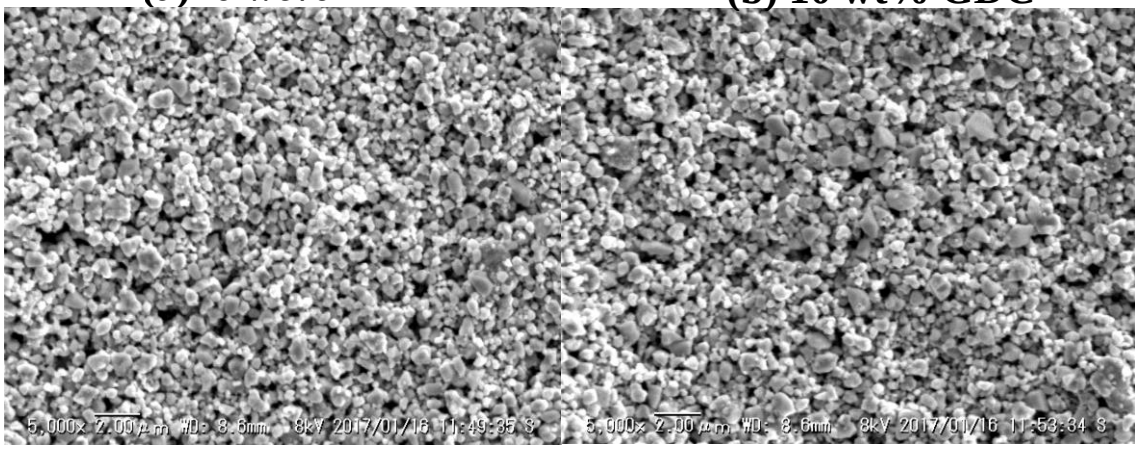

(c) 20 wt% GDC (d) 30 wt% GDC

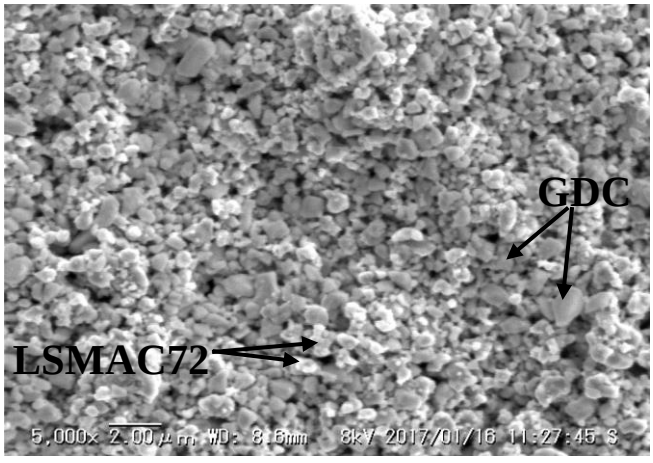

(e) 40 wt% GDC

Figure 4.8 Surface SEM images before power generation measurement for LSMAC72 + GDC at a) 0 wt%; b) 10 wt%; c) 20 wt%; d) 30 wt% and e) 40 wt%

In contrast, Fig. 4.9 represents the surface SEM images for composite LSMAC72+GDC at 0 - 40 wt% GDC content after the power generation measurement at 973 K. The morphological structure without GDC (Fig. 4.9 (a)) shows extreme microstructural changes under prolonged operation in dry C_3H_8 which explains its low performance. However, by adding GDC especially at 10 – 20 wt% the microstructure seems fairly preserved which is essential for gas diffusion as the porosity is retained. Conversely, the microstructure of the composite at 30 and 40 wt% seems to be sintered, reducing the crucial porosity which corresponds to their higher anodic overpotential. In addition, unexpectedly carbon filament seems to appear with higher GDC content at 40 wt%.

The corresponding carbon elemental distribution map for LSMAC72 + 40 wt% GDC proves inconclusive whether the filament structure belongs to carbon deposit. Hence, further Raman characterization is performed on the surface of the composite anodes and shown in Fig. 4.10. It is recognisable that Raman spectrum for LSMAC72+GDC at 30 wt% and 40 wt% GDC shows sharp peaks corresponds to carbon structure of D- and G-band spectrum confirming the presence of carbon deposit. No obvious peak is observed at 10 wt% GDC but weaker peaks is displayed by composite with 20 wt% GDC. Li and co-workers reported that carbon beads were formed on Ni-GDC anode when using CH_4 fuel even at 40 wt% GDC content.[15] While Ni is known to be the main catalyst for carbon formation compared to LSMAC72 which is fairly a coke resistant oxide anode, it is noteworthy to know that their work used humidified CH_4 fuel which is less favourable condition for carbon formation compared to the fuel condition in the current study. The distinct reason for severe carbon formation with higher GDC content is unclear however it is known that carbon formation also depends on the shape and structure of the catalyst and mixing GDC at higher content may ease the carbon formation.

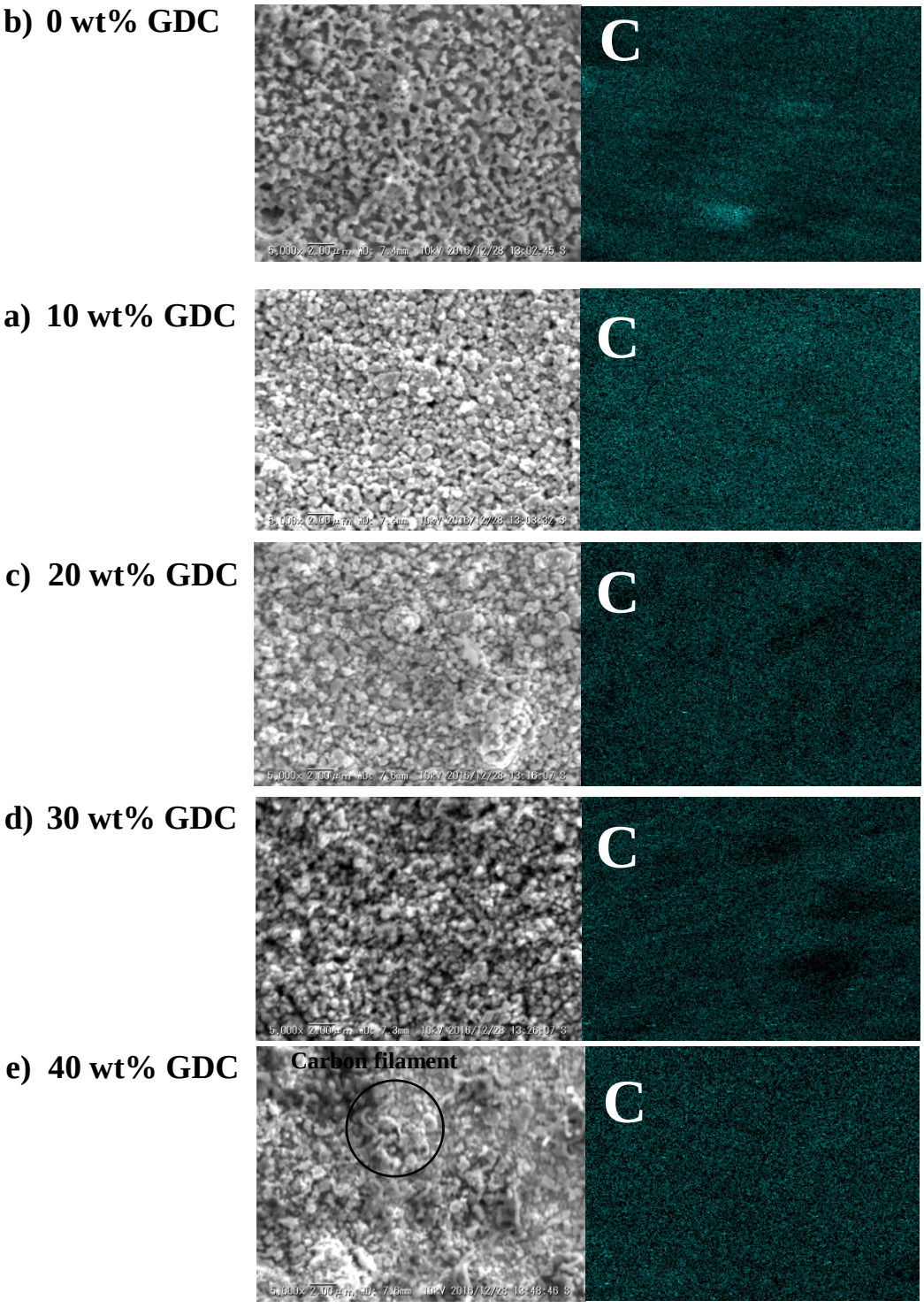

Figure 4.9 Surface SEM images and the corresponding EDS scanning for carbon element after power generation measurement in C_3H_8 at 973 K for LSMAC72 + GDC at a) 0 wt%; b) 10 wt%; c) 20 wt%; d) 30 wt% and e) 40 wt%

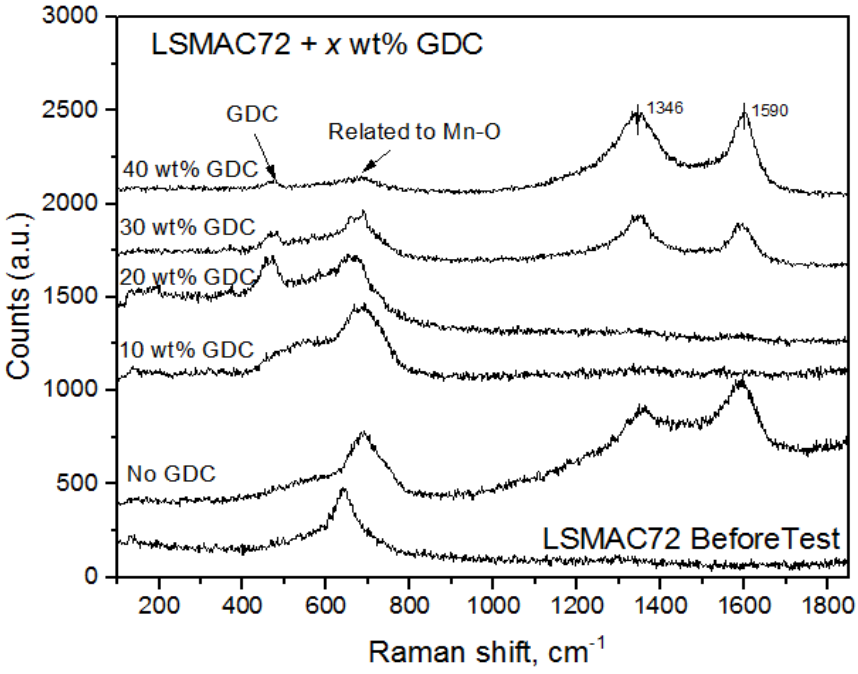

Figure 4.10 Raman spectra of composite LSMAC72+GDC anodes at 0-40 wt% GDC after the power generating measurement using C_3H_8 fuel at 973 K

Finally, Fig. 4.11 shows the phase stability of the composite anode LSMAC72 with GDC from 0 – 40 wt% GDC after the power generation measurement. The XRD result suggests that the stability of the LSMAC72+GDC is fairly similar with other composite LSMAC72 anodes where the $(La,Sr)_2MnO_4$ peaks are clearly visible and changes in the intensity of GDC peaks are as expected increasing with GDC content. More importantly, the phase stability has been quantitatively calculated by the peak intensity ratio of $LaMnO_3/(La,Sr)_2MnO_4$ determined from the highest $LaMnO_3$ peak at 33°. At 0 wt% GDC, the intensity ratio was calculated to be 0.85 and increasing with higher GDC content at 0.89 for 10 wt%, 1.12 for 20 wt%, 1.06 for 30 wt% and the highest at 1.39 for 40 wt%. Clearly, while the morphology of composite LSMAC72 with higher GDC content heavily changed, the phase stability improves greatly. This result confirms that GDC is fairly stable under the current operational condition and a viable way to improve the phase stability and the cell performance at least up to 20 wt%.

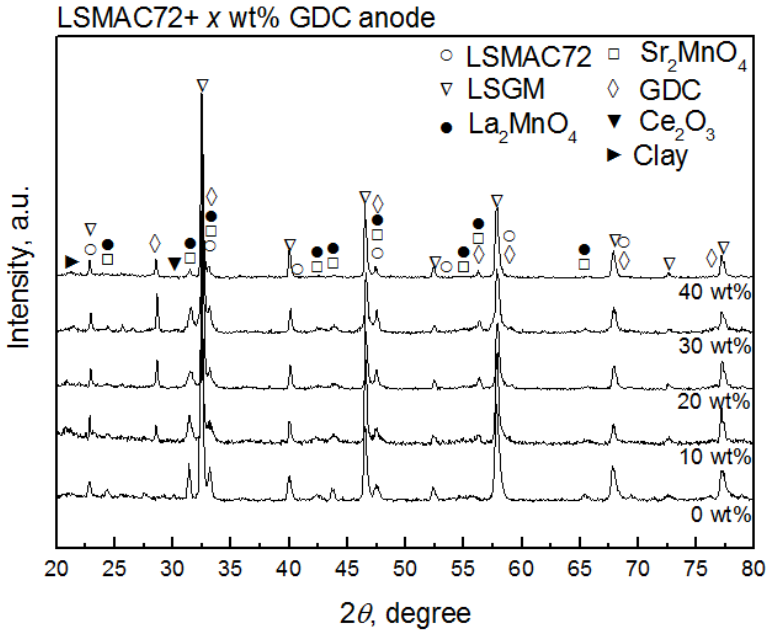

Fig. 4.11 Comparison of XRD pattern for composite LSMAC72+ *x* wt% GDC anode after power generation measurement at 973 K

4.4 Conclusion

Mixing LSMAC72 with various oxides at 10 wt% for anodic performance was studied and it was found that adding oxide anode shows positive effects for all composites when using direct C_3H_8 fuel. Particularly, it can be established that STN or GDC shows the most positive effects especially at 1173 K. However, the MPD rapidly dropped for LSMAC72+STN but LSMAC72+GDC shows fairly stable cell performance from 1173 K to 973 K. Impedance arc and internal resistance analysis suggests that anodic overpotential is especially decreased when adding oxide anodes. SEM micrograph reveals that there is barely any obvious change to the anode surface of LSMAC72+GDC and LSMAC72+LSGM but other composites particularly LSMAC72+LSFM shows microstructural changes after the power generation measurement in C_3H_8 at 973 K. Particularly, numerous porosity and interconnect of the particles are visible, allowing for better gas diffusion which leads to lower

overpotential for LSMAC72+GDC. In addition, GDC enhanced the catalytic oxidation of C_3H_8, facilitating the kinetic of the fuel oxidation. Increasing GDC content shows positive effect to the MPD up to 20 wt% GDC. However, unexpectedly carbon formation is easier to deposit with GDC content higher than 30 wt% due to microstructural changes associated with higher GDC content. Nevertheless, this study has confirmed that enhanced power density can be achieved when LSMAC72 is mixed as a composite with GDC.

Reference

(1) S. Tao, J.T. Irvine, Nat. Mater. **2**(5), 320 (2003).

(2) R. Gorte, H. Kim, J. Vohs, J. Power Sources **106**(1-2), 10 (2002).

(3) T. Kim, G. Liu, M. Boaro, S. Lee, J. Vohs, R. Gorte, O.H. Al-Madhi, B. Dabbousi, J. Power Sources **155**(2), 231 (2006).

(4) R. Gorte, J. Catal. **216**(1-2), 477 (2003).

(5) H. He, J.M. Vohs, R.J. Gorte, J. Power Sources **144**, 135 (2005).

(6) Z.L. Zhan, S.A. Barnett, Science, **308**(5723), 844 **(**2005).

(7) B.D. Madsen, S.A. Barnett, Solid State Ionics, **176**(35-36), 2545 (2005).

(8) A. Atkinson, S. Barnett, R.J. Gorte, J.T.S. Irvine, A.J. McEvoy, M. Mogensen, S. Singhal, J. Vohs, Nat. Mater., **3**, 17 (2004).

(9) P. Blennow, A. Hagen, K.K. Hansen, L.R. Wallenberg, M. Mogensen, Solid State Ion. **179**, 2047 (2008).

(10) P. Blennow, K. K. Hansen, L.R. Wallenberg, M. Mogensen, ECS Trans. **13**(26), 181 (2008).

(11) P. Blennow, K. K. Hansen, L.R. Wallenberg, M. Mogensen, Solid State Ion. **180**, 63 (2009).

(12) T.H. Shin, S. Ida, T. Ishihara, J. Am. Chem. Soc. **133**(48), 19399 (2011).

(13) K.J. Kim, G.M. Choi, J. Electroceram. **35**, 68 (2015)

(14) S. Mcintosh, R.J. Gorte, Chem. Rev. **104**, 4845 (2004).

(15) M. Li, B. Hua, J. Luo, S.P. Jiang, J. Pu, B. Chi, L. Jian, J. Mater. Chem. A. **3**, 21609 (2015).

CHAPTER 5

Conclusion

5.1 Summary

The discovery of current state-of-the-art Ni/YSZ cermet anodes has passed its centennial anniversary years ago. Yet, while its catalytic and electrical conductivity is unrivalled when in use with the synergistic effect of YSZ electrolyte, its use in current-day SOFC stacks poses a great challenge whenever hydrocarbon or carbonaceous fuels are to be used. The promise of hydrogen economy is still not completely fulfilled and while the potential of clean and renewable energy from a multitude of energy sources is proven to be unreliable owing to power fluctuation. Likely, the most viable route for the near future is better efficiency of energy conservation especially in the energy conversion. In this regard, the current study has, from the beginning looks to find an alternative material that may substitute Ni in terms of fuel flexibility while concurrently displaying a significant cell performance. This property coupled with high energy conversion efficiency makes it an attractive option for many stationary and distributed power applications.

The groundwork and motivation of this study has been clearly laid out in Chapter 1. In order to develop a novel anode material that is inert to carbon formation, the principle theory of SOFC and basics of carbon formation mechanism has been discussed in great length. Additionally, it has been made crystal clear that majority of studies focus on novel materials with uncharted properties and characteristics, presenting a difficult transition for near future commercialization. Hence, a lower-risk and an established substantial know-how route is by improving the current and widely studied material to be used as anode. With that in mind, 50 mol% Sr-doped $LaMnO_3$ (LSM55) was picked as the host anode to be used with hydrocarbon fuel, an oxide anode that has been long studied and used as a cathode material.

The key to utilize LSM55 as an anode is improvement to the phase stability under reducing environment. In Chapter 2, the effect of various dopants onto Mn site of LSM55 to its phase stability is investigated. Reasonable high activity of LSM55 towards H_2 oxidation was observed and the power density of up to 1 W/cm^2 at 1273 K can be achieved when using a cell with LSGM electrolyte that utilizes H_2 fuel. However, the power density using LSM55 significantly decreased when C_3H_8 is used for fuel and this could be explained by the low stability of LSM in reducing atmosphere that produces low catalytic activity phases like La_2MnO_4 and Sr_2MnO_4. It was demonstrated that the cell using doped Al greatly improved the phase stability of LSM55 under reducing environment owing to stable Al^{3+} state. In particular, $La_{0.6}Sr_{0.4}Mn_{0.6}Al_{0.4}O_3$ shows high activity to electrochemical oxidation of C_3H_8 resulting in the increased power density of 200 mW/cm^2 which is almost 3 times of non-doped LSM anode. In spite of low activity of Al^{3+} to oxidation, this could be assigned to the increased stability of LSM in dry C_3H_8. This may suggests that the perovskite phase of $LaMnO_3$ is higher catalytic activity to C_3H_8 oxidation than that of La_2MnO_4 and also of higher electrical conductivity. Small particle size of LSM55 was also sustained by doping with Al and so doping Al for Mn site of $La_{0.5}Sr_{0.5}MnO_3$ is positively worked for decreasing the anodic overpotential. Therefore, $La_{0.5}Sr_{0.5}Mn_{0.6}Al_{0.4}O_3$ is promising as oxide anode for direct hydrocarbon type SOFC.

In Chapter 3, further improvement to the Al-doped LSM55 was investigated. Among the various dopant, Co as a catalyst is used to enhance the surface activity of the material. Nonetheless, the power density of LSMA64 is found to be insufficient in C_3H_8 and even negligible when using H_2 fuel. Co substitution in the Mn site proves to be effective for increasing the power density of LSMA especially in C_3H_8 environment. At 20% Co dopant (LSMAC72), similar electrochemical activity to LSM55 is achieved in H_2 (0.95 W/cm^2) while the largest MPD amongst all doped LSM is demonstrated when using C_3H_8 (0.25 W/cm^2) despite the use of thick LSGM electrolyte of 0.285 mm. The electrical

conductivity of LSMAC72 is admittedly lower than LSM itself, however reduced IR loss is achieved during power generation in C_3H_8 due to possibly reduced interface resistance and better phase stability towards reduction. In addition, it was confirmed that no coke deposition is observed by using three different method, SEM-EDS, Raman spectroscopy and XPS. Consequently, the incorporation of Co as a catalyst further yielding increased performance in direct C_3H_8 oxidation. While decomposition still occurs, Al doping suppressed the phase separation and hence this study reveals the potential of LSMAC72 as an alternative anode material for direct C_3H_8 oxidation.

In Chapter 4, insufficient MPD for LSMAC requires another approach to increase its anodic activity. Mixing LSMAC72 with various oxides for anodic performance was studied and it was found that positive effects were observed for C_3H_8 fuel. In case of oxides mixed with LSMAC72, it was found that STN or GDC shows the most positive effects for C_3H_8 fuel. The increased MPD was shown by composite LSMAC72 with STN and GDC. Impedance arc and internal resistance analysis suggests that anodic overpotential is decreased when using STN or GDC. SEM micrograph reveals that there is barely any obvious change to the anode surface of LSMAC72+GDC and LSMAC72+STN after the power generation measurement in C_3H_8 at 1173 K. Particularly, numerous porosity and interconnect of the particles are visible, allowing for better gas diffusion which leads to lower overpotential. In addition, GDC enhanced the catalytic oxidation of C_3H_8, facilitating the kinetic of the fuel oxidation. The exact nature for the improvement for LSMAC72+STN requires further study to understand since reaction kinetic and surface morphology has larger influence to the overall cell performance when using hydrocarbon fuel. Nevertheless, this study has confirmed that enhanced power density can be achieved when LSMAC72 is mixed as a composite with selected oxide anodes. In addition, high electrical conductivity of an oxide anode does not guarantee improved performance as electrocatalytic activity and microstructure also play important role as has been described in the previous section. It is

expected that further increase in STN or GDC component is effective for increasing in power density in particular for C_3H_8 fuel.

5.2 Future Prospect

This study therefore, represents a valuable contribution to the scientific world of SOFC on the feasibility of using $LaMnO_3$ based compound (LSM55) as an anode for direct hydrocarbon SOFC. The phase stability of $LaMnO_3$ can be increased by doping selected element and especially improved when Al is used as dopant. While power density is lower than LSM55 in H_2, double doping with Co and Al on the Mn site (LSMAC) improves its ionic conductivity and charge transfer, effectively increases the MPD of LSMAC when using hydrocarbon fuel. Notably, $La_{0.5}Sr_{0.5}Mn_{0.7}Al_{0.1}Co_{0.2}O_3$ or LSMAC72 exhibits similar cell performance in H_2 to LSM55 while superior performance up to 4 times higher in C_3H_8 was recorded. This enhancement comes with better phase stability in reducing environment, which LSM55 greatly suffers. More importantly, LSMAC72 shows coking tolerant towards hydrocarbon fuel, confirmed by SEM-EDS, XPS and Raman spectroscopy. This characteristic alone is a huge advantage compared to Ni-based anode, which this study is intended to replace. Essentially, further improvement is still required to realize this novel anode as direct hydrocarbon SOFC anode especially towards electrical conductivity and enhanced phase stability. Regardless, it is expected that with continuous work on LSMAC72 whether by further investigation in dopants or by mixing with other more stable and highly conductive oxide component, the oxide anode may be able to be used as replacement for the conventional anode being used today for hydrocarbon SOFC in the future.

ACKNOWLEDGEMENT

Alhamdulillah, my utmost and millions gratitude to Allah, I humbly ask for your forgiveness and all praises for the glory of our Creator the Most Gracious, Most Compassionate. For without Your blessings, I won't be able to sail through this enormous challenge by myself all these years.

I am highly indebted and grateful to Prof. Tatsumi Ishihara for his utmost understanding, his patience and his compassion in nurturing me, guiding and counselling me, even when things doesn't work smoothly the way it should. I am deeply grateful for your guidance and encouragement to pursue and spend every bit of my breath to complete this dissertation within the period given. Your extensive knowledge and vast know-how, not to mention your amazing dedication and unrivalled work-rate has been and always be my source of inspiration that I will try my level best to emulate. I am also honored to have Prof. Keiji Tanaka from Department of Materials Physics and Chemistry and Prof. Katsuro Hayashi from Department Chemistry and Biochemistry on the dissertation committee. Their diverse expertise and perspectives have greatly enriched my educational and research experience.

I also wish to express my gratitude to all members and staff of Ishihara Laboratory, especially Assoc. Prof. Shintaro Ida for his invaluable advices and help. Similarly, big thank you to my mentors and friends who have been there to help me out, Dr. Inoishi, Dr. Hosoi, Dr. Hyodo, Dr. Hong and especially Dr. Ju and Kusoda, who assisted me in developing my understanding on the SOFC subject and Murakami for the immediate help with the XPS measurement.. Special thanks to Prof. Nipaka and Prof. Tang for your tremendous help and everlasting friendship. I reserved my thanks as well to my partner in crime, Dr. Wang who literally lifted me up when I have just arrived, Dr. Jang and Kim, the ever knowledgeable and dependable friends, Tan, Dr. Fan, Dr. Ting, Zhang and Lin for all the memories and laughter that we have shared together.

Last but never the least, I dedicated this achievement to my parents and family, to my late father, Kamarul Bahrain, a dedicated and strong-willed person that even in your final days your words still rang to my ears to keep going, to do whatever it takes to pursue the highest echelon in academics. To my beloved mother, Aishah the venerable yet strong old lady that gave her blessing, knowing we'll be far apart for years but your love, your prayers and your blessings keep showering us throughout our life here. And plenty of love to my wife, Nor Diana the ever supportive and understanding wife and wonderful daughters Raissya Kaleyla and Rihanna Keysha, thank you for simply just being with me here, your presence itself bring colors to my life, your love encourages and motivates me through all the thick and thin. And finally to my parents-in-law and my siblings, heartfelt love and huge thanks for the support, prayers and motivation.

I wish to acknowledge the opportunity and full financial support by MEXT through the prestigious 2013 Monbukagakusho scholarship.